catalysts

MDPI

Review

From CO_2 to Value-Added Products: A Review about Carbon-Based Materials for Electro-Chemical CO_2 Conversion

Lilian D. Ramírez-Valencia, Esther Bailón-García *, Francisco Carrasco-Marín and Agustín F. Pérez-Cadenas

Carbon Materials Research Group, Department of Inorganic Chemistry, Faculty of Sciences, Campus Fuentenueva s/n, University of Granada, 18071 Granada, Spain; liliandr@correo.ugr.es (L.D.R.-V.); fmarin@ugr.es (F.C.-M.); afperez@ugr.es (A.F.P.-C.)

* Correspondence: estherbg@ugr.es; Tel.: +34-958-243-235; Fax: +34-958-248-526

Abstract: The global warming and the dangerous climate change arising from the massive emission of CO_2 from the burning of fossil fuels have motivated the search for alternative clean and sustainable energy sources. However, the industrial development and population necessities make the decoupling of economic growth from fossil fuels unimaginable and, consequently, the capture and conversion of CO_2 to fuels seems to be, nowadays, one of the most promising and attractive solutions in a world with high energy demand. In this respect, the electrochemical CO_2 conversion using renewable electricity provides a promising solution. However, faradaic efficiency of common electro-catalysts is low, and therefore, the design of highly selective, energy-efficient, and cost-effective electrocatalysts is critical. Carbon-based materials present some advantages such as relatively low cost and renewability, excellent electrical conductivity, and tunable textural and chemical surface, which show them as competitive materials for the electro-reduction of CO_2. In this review, an overview of the recent progress of carbon-based electro-catalysts in the conversion of CO_2 to valuable products is presented, focusing on the role of the different carbon properties, which provides a useful understanding for the materials design progress in this field. Development opportunities and challenges in the field are also summarized.

Keywords: carbon dioxide; electro-reduction; carbon-based materials; value-added products

Citation: Ramírez-Valencia, L.D.; Bailón-García, E.; Carrasco-Marín, F.; Pérez-Cadenas, A.F. From CO_2 to Value-Added Products: A Review about Carbon-Based Materials for Electro-Chemical CO_2 Conversion. *Catalysts* **2021**, *11*, 351. https://doi.org/10.3390/catal11030351

Academic Editors: Ki Tae Park, Chang-Tang Chang and Wonhee Lee

Received: 11 February 2021
Accepted: 4 March 2021
Published: 9 March 2021

1. Introduction

The energy supply currently depends mostly on fossil fuels, causing a continuous accumulation and, therefore, an excess of CO_2 in the atmosphere, bringing negative effects on the environment. The population and live standards growth make not imaginable the decoupling of energy supply from fossil fuels. Faced with this situation, different alternatives have been proposed to mitigate the environmental impact and dependence on non-renewable energy sources. The conversion of CO_2 into value-added products by chemical reactions seems to be the most promising and attractive solution since, together with the reduction of the atmospheric CO_2 levels, CO_2 is efficiently recycled stablishing an ideal zero-emission carbon balance. CO_2 can be converted to added-value products by photochemical [1–4], thermochemical [5–8], radiochemical [9,10], biochemical [11–14], and electrochemical [15–18] strategies. However, the most interesting alternative is the capture and use of CO_2 as raw material to produce various products (Table 1) through its electrochemical reduction since this is a flexible and controllable process with mild and safe operating conditions and low equipment cost, which also allows coupling environmentally friendly non-fossil energy from renewable sources. Taking into account these advantages, many efforts have been made worldwide in the development and improvement of the technology available for CO_2 electro-conversion.

However, despite the fact that electro-reduction of CO_2 (CO_2RR) is thermodynamically viable, its transformation presents very slow reaction kinetics and usually requires significant energy expenditure [19] due to the high stability and inertness of the CO_2

molecule [20]. Therefore, an extensive research has been developed by the overall scientific community focused on the electrocatalyst design, since the efficiency and selectivity of the reduction reaction is strongly dependent on the electrode nature, properties, and configuration [21]. An ideal catalyst for CO_2 electroreduction requires: (i) Being able to mediate the transfer of electrons coupled to protons, (ii) having a low over potential for the activation of the CO_2 molecule, (iii) exhibiting a selectivity preferably towards a target product, and (iv) preserving structural integrity during prolonged operation.

Table 1. Equilibrium potential and Gibbs free energy for CO_2 reduction reactions.

Reduction Reactions	Gibbs Free Energy ΔG° (Kj mol$-^1$)	Standard Potential E° (Volts vs. NHE)
$2CO_{2(g)} + 2H^+ + 2e^- \rightarrow H_2C_2O_4$	+91.8	−0.475
$CO_{2(g)} + 2H^+ + 2e^- \rightarrow HCOOH_{(aq)}$	+38.4	−0.199
$CO_{2(g)} + 2H^+ + 2e^- \rightarrow CO_{(g)} + H_2O$	+19.9	−0.103
$CO_{2(g)} + 4H^+ + 4e^- \rightarrow HCHO_{(aq)} + H_2O$	+27.5	−0.071
$CO_{2(g)} + 6H^+ + 6e^- \rightarrow CH_3OH_{(aq)} + H_2O$	−17.3	+0.030
$CO_{2(g)} + 8H^+ + 8e^- \rightarrow CH_{4(g)} + 2H_2O$	−130.8	+0.169

Lately, carbon-based catalysts have attracted much attention due to their relatively low cost and renewability, good chemical stability, excellent electrical conductivity, tunable textural and chemical surface, and large surface area, containing micropores, mesopores, and macropores that favor adsorption, access, and diffusion of molecules to the internal active sites of the material [22]. Due to these particular characteristics, carbon-based materials have been extensively used as electrocatalysts for CO_2 reduction either as supports to disperse different metallic particles with several sizes (single-atoms, dual-atoms, nanoparticles) or as direct catalyst by functionalization with heteroatoms to prepare economical and sustainable metal-free electro-catalysts [23]. The purpose of this article is to provide an overview of the recent advances in the design of carbon-based materials for the CO_2 electroreduction, including metal-free and metal-based carbon materials, putting emphasis on the relationship between catalysts properties and the target add-value product.

2. Metal-Free Carbon Materials as Catalyst

Metal-free carbon-based catalysts emerge as an alternative to overcome the difficulties that arise when using metals as catalysts, such as their limited availability and poor durability that prevent their application on large scales. However, the activity of carbon materials itself is poor, so heteroatoms (N, B, S, P, F) are introduced into the carbon structure to promote electrocatalytic activity and selectivity [24]. Carbon doping with foreign heteroatoms affects the electronic structure of carbon materials since the different size and electronegativity of such foreign atoms compared to carbon atoms lead to a charge redistribution and, consequently, modify their electrochemical catalytic properties [25]. Additionally, the covalent chemical bonds between the carbon and the doped atoms avoid segregation problems occurring in metal-based catalysts leading to better operational stability [25]. Different heteroatoms have been used to dope carbon obtaining materials with good electrochemical performance in the CO_2 reduction, and among them, N and B have been the most studied.

2.1. N-Doped Carbon-Based Materials

The N atom has a similar size to the C atom but higher electronegativity [26], therefore the defects caused by nitrogen doping can break the electroneutrality of C atoms in the hexagonal carbon structure [27] leading to an enhanced electronic/ionic conductivity without distortion in the local geometry that influences the electrocatalytic activity [28]. N-doped carbons have shown to be promising candidates as catalysts for the electro-reduction of CO_2 due to the low over-potentials obtained, the high activity, stability, and selectivity towards certain products ascribed to this surface properties modification. The nitrogen

species are located in several places within the carbon skeleton, which results in different active sites. The electrocatalytic behavior of the N-doped carbons towards CO_2RR is deeply dependent on the type of nitrogenated surface group and its content [26].

2.1.1. N-Doping Methodology and N-Doped Catalyst Active Sites

Different carbon and nitrogen precursors have been used for the synthesis of N-doped carbon electrocatalysts (Table 2). Two main doping strategies have been developed: In situ and post-doping treatments. The first consists of simultaneously perform both the synthesis and doping of carbon-based materials at the same time; while in the second, the carbon material is first synthesized and then doped in a subsequent process [22,25]. After doping, four types of nitrogen species can be identified in the carbon skeleton by XPS: Pyridinic (398.5 eV), pyrrolic/pyridonic (399.9 eV), quaternary or graphitic N (401.0 eV), and oxidized pyridinic species (403.4 eV) [29,30]. The total amount of nitrogen fixed on the carbon structure and the nature of N functionalities clearly depends on the N precursor source, doping methodology, and carbon material.

Table 2. Carbon and nitrogen precursors to construction of electrocatalysts and active sites.

Sample	Main Product	Carbon Precursor	N Precursor	Type [a]	Synthesis Method	Nitrogen Species (% atomic) XPS					Active site	Ref
						N [b]	Pyri [c]	Pyrr [d]	G [e]	O [f]		
NR/CS-900	CO	CS (porous carbon nanosheets)	Polymerized Aniline with Ammonium Persistence to Polyaniline (Solid)	Post	Activation ($ZnCl_2$) and pyrolysis	5.30	1.45	1.05	2	0.8	Pyridinic	[31]
NCNTs	CO	CNTs	Acetonitrile-dicyandiamide	In situ	Liquid vapor deposition (CVD)	5.0	1.5	1.1	2.4	n.d.	Pyridinic	[32]
WNCNs-1000	CO	Coal, NaCl template method C-700	NH_3	Post	Pyrolysis	4.3	2.61	1.45	0.16	0.08	Pyridinic	[33]
NCNTs-ACN-850	CO	CNTs (Acetonitrile)	Dicyandiamide	In situ	Liquid chemical vapor deposition	4.9	1	0.5	3.4	n.d.	Pyridinic	[21]
CN/MWCNT	CO	MWCNT	NaN_3 reacts with $C_3N_2Cl_3$ to form g-C_3N_4	Post	Pyrolysis	0.12	n.d.	n.d.	n.d.	n.d.	n.d.	[34]
NCNT-3-700	CO	CNTs	Poly(diallyldimethy lammonium chloride) (PDDA)	Post	Pyrolysis	1.75	0.5	0.625	0.5	0.125	Graphitic	[35]
CNPC-1100	CO	Coal	NH_3	Post	Ammonia etching/pyrolysis	4	1	1	1.5	0.5	n.d.	[36]
NG-800	CO	GF (Graphene foam) Ni-foam vapor deposition	gC_3N_4 (Solid)	Post	Pyrolysis	6.6	4.5	1.5	0.6	n.d.	Pyridinic	[37]
MNC-D	CO	ZIF-8	Dimethyformamide DMF	Post	Heat-treated	16.97	8	5	4	n.d.	Pyridinic	[38]
NPC-900	CO	Coal arantracite	Dicyandiamide (DICY)	In situ	Activation (KOH)/Pyrolysis	1.92	0.60	0.50	0.83	n.d.	n.d.	[27]
N-CWM	CO	Natural wood	Urea	Post	Pyrolysis	4.07	0.54	2.90	0.55	0.09	Pyridinic	[39]
N-graphene	Formate	Graphene oxide	Melamine (Solid)	In situ	Pyrolysis	5.5	3	0.9	1.6	n.d.	Pyridinic	[40]

Table 2. *Cont.*

Sample	Main Product	Carbon Precursor	N Precursor	Type [a]	Synthesis Method	Nitrogen Species (% atomic) XPS					Active site	Ref
						N [b]	Pyri [c]	Pyrr [d]	G [e]	O [f]		
PEI-NCNT/GC	Formate	Multiwalled CNT	Ammonia plasma/co-catalyst (PEI)	Post	Ammonia plasma enhanced chemical vapor deposition (PECVD)	11.3	n.d.	n.d.	n.d.	n.d.	n.d.	[41]
HNCM/CNT	Formate	CNT	Dimethyformamide DMF	In situ	Pyrolysis	8.26	3.5	n.d.	4.8	n.d.	Pyridinic	[42]
N-C61-800	Formate	Fullerene PC61BM	Urea	In situ	Pyrolysis	2.57	0.39	0.54	1.64	n.d	Graphitic	[43]
CF-120	Syngas	CF (carbon foam)PU	NH_3	Post	Ammonia etching/pyrolysis	5.5	2.5	1.8	0.6	0.6	Pyridinic/ Pyrrolic	[44]
3D N-CNTs/SS-750	Syngas	Melamine	Melamine	In situ	Pyrolysis	6.8	3.90	0.50	2.50	n.d.	n.d.	[45]
c-NC	Ethanol	Resol	Dicyandiamide	In situ	Pyrolysis/Template method-mesoporous materials	7	2.6	2.8	1.6	n.d.	Pyridinic/ Pyrrolic	[46]
MNCs-5	Ethanol	Resol	Dicyandiamide	In situ	Pyrolysis/triblock-copolymer-templating method.	~6.2	2.1	2.8	1.3	n.d.	Pyridinic/ Pyrrolic	[47]
GO-VB6-4	Ethanol-Acetone	Graphene oxide	B6 Vitamin	Post	heat treatment	2.3	2.3	n.d.	n.d.	n.d.	Pyridinic	[48]
NGM-1/CP	CH_4	Graphene	3-Pyridinecarbonitrile	In situ	Pyrolysis	6.52	1.45	3.35	1.72	n.d.	Pyridinic/ Pyrrolic	[49]

[a] N-doping type, [b] N total, [c] Pyridinic, [d] Pyrrolic, [e] Graphitic, [f] Oxide.

These N species can act as active sites for the electrochemical reduction of CO_2. N-containing groups have a Lewis base character allowing them to easily interact with the acidic CO_2 molecules favoring its adsorption and reaction on the catalyst surface [42,50]. The catalytic activity for CO_2RR has been reported to be dependent on the type of the N-containing groups [37,38,51]. Most authors agree that pyridine N species are the most active sites for CO_2 electroreduction because this functionality has lone pairs of electrons, which makes it capable of binding CO_2 [21]. Some authors [46,47,49,52], although to a lesser extent, have also reported that N-pyrrolic species can be active sites for the CO_2 electroreduction whereas others identify N-pyrrolic as main active sites for hydrogen evolution reaction (HER) [24,39]. The role of graphitic/quaternary N species is even more controversial. Some authors [31,46,47,53] concluded that graphitic N does not play a wide role in the CO_2 reduction since graphitic N electrons are located in the π^* antibonding orbital being less available for CO_2 binding [21,53], whereas other authors such as Xu and co-authors [35] or Chen and co-authors [43] showed that N-graphitic can also be an active site for electrochemical reactions. These controversial results in terms of active sites can be attributed to the different morphologies and structures of the carbon materials that can expose more or less different functionalities of nitrogen, as well as affecting its location within the structure [28,38,54,55].

In view of the above, recently, Tuci and coauthors [16] studied a series of N-pyridinic heterocycles because, as mentioned above, the pyridinic N nuclei are the most active sites. N-pyridine heterocycles are dangling groups covalently attached to the surface of multi-walled carbon nanotubes (Figure 1). These were used as metal-free electrocatalysts using an exohedral functionalization strategy, which contributed to clarify the role of the content of nitrogen groups in the activation of CO_2 and its electrochemical conversion. The evidence allows to infer that both the basic character of each heterocycle (Pyridinic-N basicity > Pyrrolic-N basicity) and the contribution of electronic charge density distribution play an important role on the electrocatalytic performance in metal-free systems. The first aspect promotes the interaction between CO_2 and dangling groups allowing (i) the generation of local CO_2 concentration gradients near the active sites of the catalyst and (ii) to reduce the energy barriers of the first electron transfer. The second aspect allows stabilizing the CO_2^{*-} intermediate before continuing its reduction.

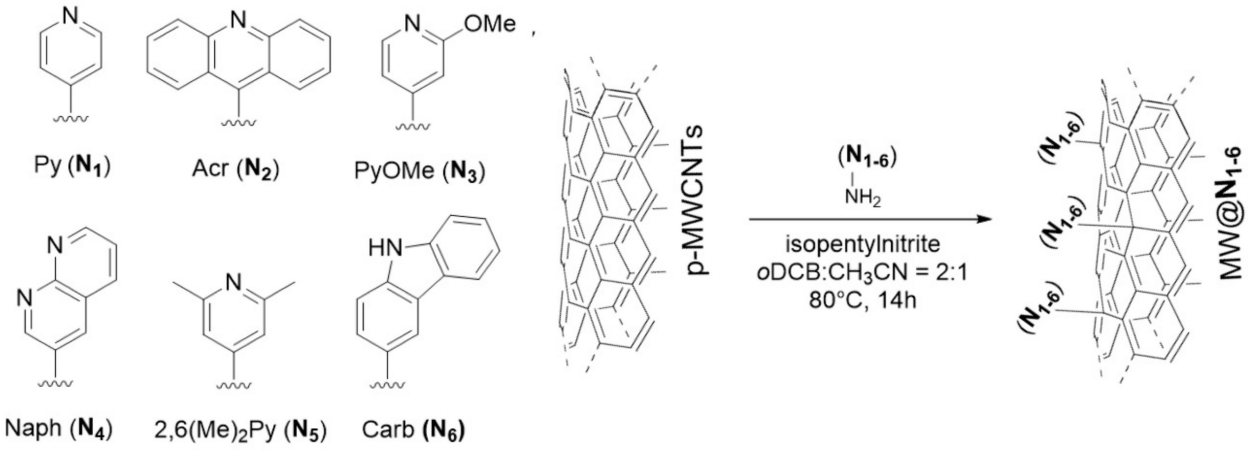

Figure 1. Exohedrally N-decorated MWCNTs (MW@N1–6) as metal free-catalysts for the CO_2 reduction reaction. Adapted from ref [16].

In general, a nitrogen functionality can be an active site if it is capable of facilitating a first electron transfer activating the CO_2 molecule to form $CO_2^{\bullet-}$, which then is transformed to key intermediary products such as COOH* and CO*. It is generally suggested that the rate limiting step for CO_2RR is this first electron transfer onto the CO_2 molecule to form $CO_2^{\bullet-}$ [22]. The selectivity and the reaction steps depend on the intermediate

stabilization at the active sites (Figure 2); essentially, for the production of CO or HCOOH, a strong CO_2 adsorption energy is required to stabilize the intermediate COOH*, but also a weak adsorption of these products is necessary to avoid further reduction or catalyst poisoning [52,56]. In the case of obtaining high selectivity towards multi-carbon products, it is due to the stabilization of the initial C1-type intermediates such as CO or HCOOH, which need to be strongly adsorbed to continue reducing them, taking advantage of the high electron densities of the medium [57].

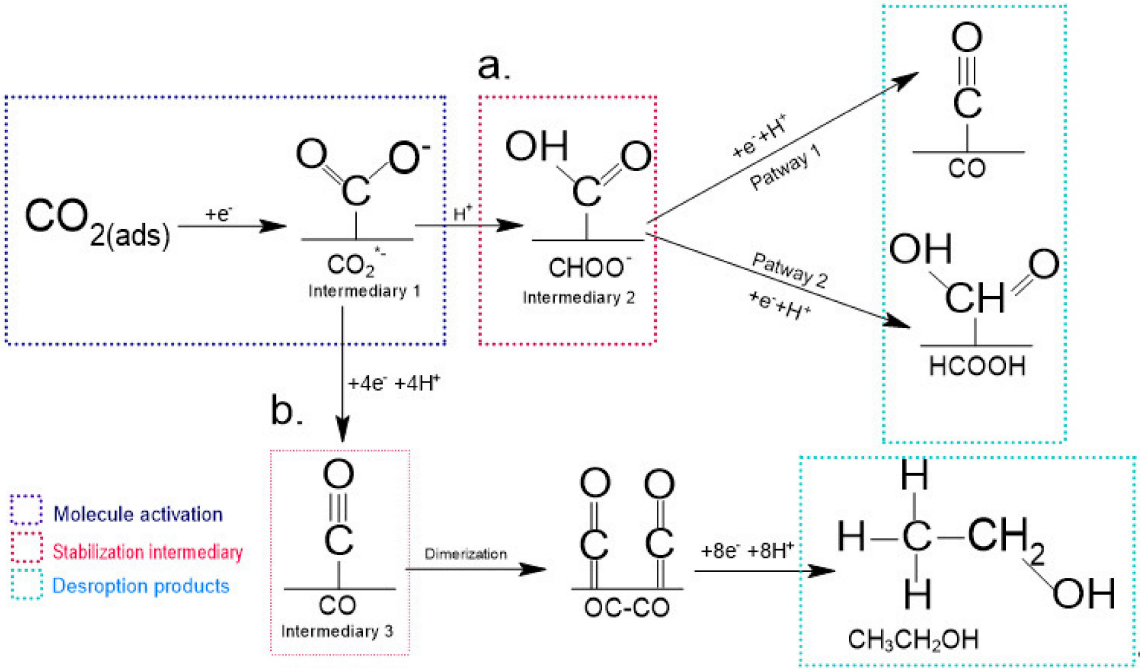

Figure 2. Selectivity and the reaction steps on N-doped metal-free catalysts (**a**) C1 type products, (**b**) C2 type products.

The N content and type can affect the adsorption and activation of CO_2 molecules as well as the bond strength between the intermediates or adsorbed products with N-functionalities, affecting the selectivity of the process. Consequently, several products such as CO, syngas, formate or formic acid, alcohols, and hydrocarbons can be obtained depending on the chemical and textural properties of N-doped carbon catalysts.

2.1.2. CO as Main Product

Among all the products in which the CO_2 molecule can be reduced, the most thermodynamically favorable product is CO since it requires only two electrons and protons for activation [58,59]. Several authors [31,33,39,60] have pointed out that N-pyridinic species are the most efficient active sites for the CO_2 electroreduction to CO. Zhang and co-authors [39] have clearly pointed out the beneficial effect of N-doping in the enhancement of the electrocatalytic activity of carbon materials. They used natural wood as carbon source to prepare a N-doped carbon membrane (Figure 3a). The wood went through a carbonization process and was subsequently doped with nitrogen using urea obtaining self-supported electro-catalyst with a hierarchical porous structure (micro-meso-macropores), high surface area, structural integrity, and abundant N-pyridinic species within the carbon framework avoiding the use of any binder that could cover the active sites. The authors confirm the remarkably effect of N-doping on the electrocatalytic kinetics of the CO_2RR; the Tafel slope was 144 mV dec^{-1} for the N-doped carbon membrane with regard to that of 195 mV dec^{-1} of the non-doped carbon membrane, indicating that the rate of CO_2 electroreduction is improved by N-doping. However, rather than the N amount, the nature of the N functionalities is crucial to enhance the activity and selectivity for the CO_2RR to CO. Liu and co-workers [60] studied this fact by tuning the nitrogen-dopant configuration

and concentration in N-doped graphene nanoribbon networks aiming to identify the active sites in the CO_2RR. The content of N-pyridinic was tuned by both in situ and post-synthesis treatments via modification of the N source concentration in the synthesis or via a post hydrogen treatment, respectively. Hydrogen post-treatment is a good strategy to tune the composition and concentration of different N species. At low temperatures, hydrogen first react with oxidized N on the surface of carbon whereas the increase of temperature enhances the reduction power of hydrogen, favoring the reduction of graphic N followed by pyridinic and pyrrolic N. They found that the CO_2RR activity is closely related to the content of N-pyridinic groups, whereas no trend was obtained for N-pyrrolic, N-quaternary, and oxidized pyridinic N functionalities. The same observation was obtained by Zhu and co-workers [31]. These authors synthesized 1D/2D nitrogen-doped carbon nanorod arrays/ultrathin carbon nanosheets catalyst by in situ polymerization of polyaniline on carbon nanosheets previously synthesized by the thermal expansion of calcium gluconate. Finally, the sample was submitted to an activation/carbonization process with $ZnCl_2$ at different temperatures (800, 900, or 1000 °C). The best electrocatalytic behavior was obtained for the catalyst treated at 900 °C. This sample presents a mesoporous structure, with the largest surface area (859.97 m^2 g^{-1}) and the highest content of N-pyridinic functionalities. Therefore, the authors also concluded that the faradaic efficiency for CO formation increased by increasing the content of N-pyridinic functionalities, a trend that was not observed for other N-functionalities. The importance of N-pyridinic functionalities was also pointed out by Li and co-workers [33]. These authors prepared wrinkled N-doped carbon nanosheets by thermal treatment of carbon nanosheets with NH_3 concluding that a good balance between the specific surface area and the pyridinic-N content is the key to obtain better catalytic performance for the electroreduction of CO_2 to CO. Consequently, Li and co-workers, in agreement with other authors, also indicate that N-pyridinic seems to be responsible for the CO_2 electroreduction to CO.

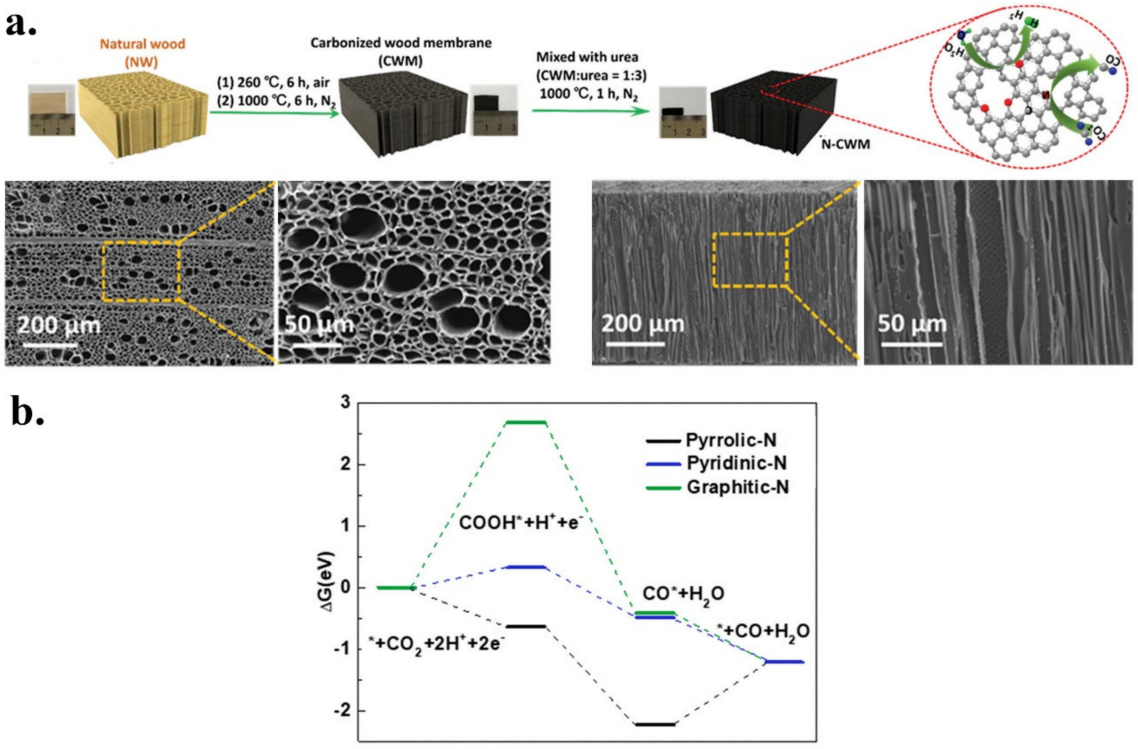

Figure 3. (**a**) Scheme of the synthesis of N-doped carbon membrane from natural wood and top-view and side-view SEM images. (**b**) Calculated Gibb free energy for CO_2 electroreduction to CO on different Nitrogen surface groups of N-doped carbon membrane. Adapted from [39].

These experimental results were corroborated by density functional theory (DFT) calculations [61]. The CO_2RR to CO on N-doped carbon materials occurs via two coupled proton–electron transfer steps forming the adsorbed intermediates COOH* and CO*, respectively. Basically, moderate bond strength between the intermediates (*COOH, *CO) and N functionalities and a weak CO adsorption is required for a high catalytic activity and reaction rate for the production of CO by electroreduction of CO_2 [31]. DFT calculations (Figure 3b) indicate a strong interaction between the intermediate *COOH and N-pyrrolic and oxidized N functionalities joined to a strongly bounded *CO resulting in low catalytic activity [31]. However, the interactions between the N-pyridinic site and intermediates (COOH* and CO*) present an adequately strong bond and an easy desorption of the CO product, which is beneficial for the conversion of CO_2 to CO [39]. Thus, the N-pyridinic effectively decrease the energy barriers for the formation of *COOH and *CO intermediates, accelerate *CO desorption, and improve the reaction kinetics toward the CO_2RR to CO.

Therefore, the increase of the pyridinic-N content in nitrogen-doped carbon materials is an interesting strategy to design high-performance catalysts for the CO_2RR to CO. Several strategies have been developed to enhance the selective pyridinic N doping both by introduction of N-containing precursors during the carbon material synthesis or by post-synthesis functionalization. Kuang and co-workers [38] observed that a post-doping etching treatment with dimethylformamide (DMF) favors the preferential formation of pyridinic N, which enhance the activation and adsorption of CO_2 and consequently, the activity, and selectivity for the CO_2RR to CO. The type of nitrogen functionalities can also be controlled by both the nature of N-containing precursors and the temperature of the carbonization/activation treatment [21,62]. Sharma and co-workers [21] control the nitrogen-bonding configuration and content in carbon nanotubes by using three different N-containing carbon precursors: Acetonitrile (ACN), dimethlyformamide (DMF), and triethylamine (TEA), and several growth temperatures: 750, 850, and 950 °C. The highest content of N was obtained using ACN as precursor and 850 °C as treatment temperature (4.9 at %). The nitrogen content decreases at higher temperatures (3.9 at %) due to the N_2 formation and release. Similar total content of N-functional groups was obtained using DMF (2.8 at %) and TEA (2.4 at %) treated at 850 °C, however the fixed nitrogen moieties are quite different and, consequently, different electrocatalytic performance was obtained. By using DMF as a precursor, relatively higher pyridinic (0.9 at %) and graphitic (1.1 at %) N and lower pyrrolic N (0.8 at %) contents were obtained compared to those obtained using TEA (0.3, 0.8, and 1.3, respectively). Consequently, the use of DMF as precursor regarding TEA results in less cathodic onset potential (−0.78 V for DMF and −1.05 V for TEA) accompanied by an increase in the FE to CO from 25 to 40%, which is attributed to the relatively higher pyridinic N content fixed using DMF. Yasuda and co-workers [63] modulate between pyridinic N and quaternary N by using pyridine or julolidine, respectively during the thermal surface polymerization of nitrogen-containing aromatic precursor molecules to fabricate nitrogen-doped graphene. Xu and co-coworkers [35] analyzed the effect of calcination temperature of poly(diallyldimethylammonium) chloride-oxidized MWCNTs composites on the quantity and nature of N functional groups. They observed that the overall nitrogen content decreases from 2.3 to 1.8 and 0.7% when the calcination temperature increases from 500 to 700 and 900 °C, respectively. The nature of the N-containing groups is also deeply affected by this temperature increase. The pyrrolic N fraction decreases and the quaternary N fraction increases markedly whereas the pyridinic fraction is almost constant by the increase of temperature. The best catalytic performance in the CO_2 electroreduction to CO was obtained for the sample calcined at 700 °C obtaining a maximum FE of 90% for CO production with a stability of over 60 h despite that the N content is not the highest one, which again demonstrates the important role that the type of nitrogen groups plays in the CO_2RR.

However, thermal treatments of carbon nanomaterials (like CNTs or graphene) at high temperatures and the introduction of N into the graphitic layer inevitably led to defects generation such as Stone-Wales or point defects due to the N removal during heating. These

defects can also act as active sites for electrochemical reactions [64] and, therefore, the role of the defects' density on the selectivity and activity for CO_2RR must be properly elucidated in order to design catalysts with the desired catalytic performance. Defects can be created by the removal of heteroatoms from graphitic layers by thermal treatment [65]. Daiyan and co-workers [65] prepared defective N-doped mesoporous carbon materials by the progressive removal of nitrogen moieties by subjecting it to an annealing thermal treatment at several temperatures (800, 900, and 1000 °C). The total content of N decreases and the I_D/I_G ratio increases by increasing the annealing temperature suggesting the generation of defects by removal of N species from the carbon lattice. These vacant sites generated by the N removal produce a rearrangement of the graphitic structure to minimize energy, forming rings of several size such as pentagons, heptagons, and octagons, which lead to the formation of structural defects. The FE to CO increases and the FE to H_2 decreases by increasing the annealing temperature revealing that defects are acting as new active sites for the electrocatalytic conversion of CO_2 to CO and therefore, defects, rather than the previously fixed N species, play a crucial role. DFT calculations indicates that N-doping would decrease the energy barriers for the CO_2 electroreduction to CO (<0.71 eV). However, N-doped sites present very negative values of the free-energy barrier for the formation of intermediate H* (<−0.53 eV) resulting in a passivation of N active sites by strongly bonded H*, which hinder the CO_2 electroreduction. Conversely, edge defect atomic sites exhibit low barriers for the CO_2 electroreduction to CO (<0.68 eV) and not very strong H* binding energy (<0.45 eV). Therefore, defects sites generated by N removal are superior active sites for the CO_2RR to CO being not passivated by strongly bounded H*.

Despite the fact that nitrogen content and nature of N groups are important factors conditioning the catalytic performance of N-doped carbon materials for the CO_2RR, it does not mean that the greater are, the better catalytic performed will be obtained. The porous structures and morphology of carbon materials are also key to enhance the CO_2RR [38]. Porous structure and catalyst morphology play an important role in the CO_2RR affecting the catalytic activity and product distribution due to effects on: (i) diffusion of solvated CO_2, (ii) residence time of products and intermediates in the pores, (iii) different mass transfers requirements for the hydrogen evolution and CO_2 electroreduction reactions, (iv) accessibility to active sites and (v) size and morphology-dependent surface coordination effects [66]. Therefore, the control and design of the textural properties and morphology of carbon materials could be an interesting strategy to control the catalytic performance and selectivity of N-doped carbon materials. Li and co-workers [36] employed coal as carbon precursor, which was etched with NH_3 in a post-doping process to simultaneously introduce nitrogen-containing defects while forming hierarchical porous structures in the carbon material. Consequently, a catalyst with a high exposure of active sites and a great ease of mass transfer was obtained and thus led to an improvement in FE for CO (92% at −0.6 V vs. RHE) with a stability of 8 h and a Tafel slope of approximately 163 mV dec^{-1}. A similar selectivity towards CO (92%) was reported by Kuang and co-authors [38] at a lower potential (−0.58 vs. RHE) and a greater stability of 16 h. These results are mainly due to the clear mesoporous structure obtained for the catalysts, which favors the generation of N-pyridinic species since their energy in the border sites is much lower compared to the internal sites of carbon-based structure [54]. The catalyst was synthesized by means of the endotemplating method that enable a control in the porosity of the carbon structure [67], and the template used was ZIF-8. Subsequently, a post-doping was carried out by means of an etching with dimethylformamide (DMF) that favors the preferential formation of N-pyridine defects. The TPD study confirmed that post-doping treatment with DMF can improve the binding strength of CO_2, which is a prerequisite for the future reduction process of this molecule. According to these results, the high specific surface area and large average pore size seems to facilitate the mass transfer of CO_2, the high N content ensures the high electrocatalysis activity, and the proper ratio of various N functionalities depresses the competing HER [36]. In addition to the surface area improvement, the tailoring of the pore size is also crucial for the

improvement of the electrochemical performance. Hursán and co-workers [66] synthesized N-doped carbons with an interconnected, uniform, and size-controlled porous structure by a sacrificial support method, starting from poly(o-phenylenediamine)polymers and using silica nanoparticles with different diameters as templates (Figure 4). At this way, after carbonization and HF etching to remove silica template, three N-doped carbons with an interconnected 3-dimensional meso or macroporous structure were obtained having pores with 13, 27, and 90 nm nominal diameters. They found that the activity for CO_2RR, the selectivity, and the stability of N–doped carbon materials are highly dependent on their porosity. The presence of mesopores is beneficial in achieving high CO selectivity and current density, with an optimal pore size around 27 nm, which was explained based on CO_2 adsorption in the different pore size, different residence time, catalyst wettability, and geometric effects.

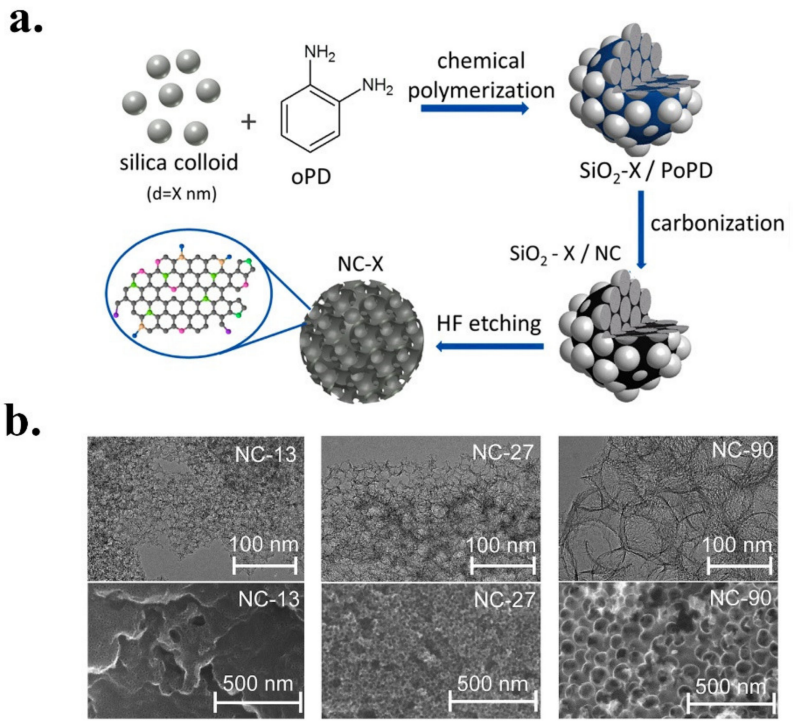

Figure 4. (**a**) Scheme of the synthesis of N-doped carbons (NC) by a sacrificial support method. (**b**) TEM and SEM images of NC with different pore sizes (13–90 nm). Adapted from [66].

Nevertheless, the microporous structure can also be effectively used for the enhancement of the CO_2 electrocatalytic conversion to CO by utilizing spatial confinement of N atoms in micropores. Following this strategy, Liu and co-authors [27] obtained a metal-free nitrogen-doped electrocatalyst with a FE towards CO of 95% and a stability of 10 h at −0.65V vs. RHE. Catalytic materials were synthesized by means of the self-assembly method induced by evaporation of a solvent using coal as carbon source, KOH as activator, and dicyandiamide (DICY) as nitrogen resource. They observed a pore contraction induced by high temperatures (900 °C), which encapsulates N atoms in the microporous structure of the material and at this way, an efficient production of CO is obtained due to the spatial confinement effect. Conversely, at 800 °C, N atoms are localized in large pores providing poor activity due to the lack of the confined space effect. Therefore, pursuing high surface areas and high amounts of nitrogen-doped in the materials will not necessarily lead to a good electro-catalytic performance, and the objective is the coordination between the structures of pores and N atoms to optimize electrochemical performance.

Although it is true that the amount and type of nitrogen species have an influence on the improvement of the electrocatalytic activity, it is the properties of the carbonaceous material such as its developed porosity that allows the improvement of the faradic efficiency

towards CO (Table 3). Therefore, for these cases, selectivity is not so related to the presence of a certain functional group, but rather depends on the structure of the carbonaceous material used, in which the micro-meso and macro pores play an important role to efficiently convert CO_2 to CO. The micropores provide abundant active sites, stabilizing the nitrogen species [27,36] while the meso and macro pores allow the contact and easy transport of the reactants and products [38,66].

Table 3. Comparison between pore structure, quantity, and distribution of N species.

Sample	Catalysts Material	Pore Structure	FE(co) %	Jco [mA/cm^2]	Nitrogen Species (% atomic) XPS					Ref.
					N Total	Pyridinic	Pyrrolic	Graphitic	Oxide	
CNPC-1100	Carbon Coal	Microporous-Mesoporous-Macro porous	92 at −0.6 V vs. RHE	0.3 at −0.6 V vs. RHE	3.90	0.95	1.13	1.27	0.55	[36]
MNC-D	ZIF-8	Mesoporous	92 at −0.58 V vs. RHE	−6.8 at −0.58 V vs. RHE	16.97	8.00	5.00	4.00	n.d.	[38]
NC-27	oPD (o-phenylenediamine)	Mesoporous-Macro pores	75 at −0.71 V vs. RHE	−1.53 at 0.71 V vs. RHE	8.43	2.25	n.d.	n.d.	n.d.	[66]
NPC-900	Carbon Coal	Microporous	95 at −0.67 V vs. RHE	−2.3 at −0.67 V vs. RHE	1.92	0.60	0.50	0.83	n.d.	[27]

2.1.3. Syngas Production

Despite the effort made to selectively obtain CO, the electrochemical reduction of CO_2 is usually accompanied by the production of hydrogen thorough the hydrogen evolution reaction (HER), which is the competitive reaction of CO_2RR. Therefore, much research has been focused on obtaining catalysts that suppress the HER to obtain selectively CO with high activity. However, the complete suppression of the HER reaction is difficult, thus, the CO produced by electroconversion of CO_2 is usually accompanied by H_2. Taking this into account, and considering that both products are the component of the synthesis gas (syngas), many efforts have been made to design catalysts that allow the formation of synthesis gas with a controllable and specific H_2/CO ratio required for the production of value-added chemical by post-thermochemical processes such as the short-chain thermochemical synthesis (H_2/CO molar ratio of 0.5), methanol or Fisher–Tropsch (H_2/CO molar ratio of 2), and hydroformylation (H_2/CO molar ratio of 1) syntheses [45].

However, the obtaining of a high activity for the CO_2RR maintaining a desirable H_2/CO molar ratio (between 0.5–2) for a hybrid electrocatalysis/thermocatalysis approach is not trivial. A CO_2 deficient environment near the catalytically active sites occurs as the CO_2 supply rate usually does not reach the consumption rate due to diffusion limitations resulting in insufficient *COOH intermediates, which leads to a dominant hydrogen evolution reaction (HER). Therefore, the rates of CO_2RR and HER reactions must be adjusted and balanced for the efficient production of syngas with tunable H_2/CO ratio [68]. Consequently, an exhaustive design of the catalyst and experimental conditions is required to try to achieve this goal.

As commented in the previous section, the activity toward CO_2RR and HER can be modified by controlling the amount and type of N functionalities and defects [44,65]. One of the main advantages of using nitrogen-doped carbonaceous materials is that the content and type of nitrogen on the catalyst surface can be adjusted by means of the tuning of synthesis parameters (temperature, N-precursor, exposure time, carbonization temperature) and consequently, controllable H_2/CO molar ratio can be obtained by the proper design of the catalyst. Liu and co-authors [45] synthesized an integrated 3D electrode by the direct grown of N-doped carbon nanotubes on a stainless-steel mesh using melamine as both nitrogen and carbon sources (Figure 5a). The stainless-steel mesh acts as grown support

and current collector. The control of the H_2/CO molar ratio was given by tuning the synthesis conditions (pyrolysis temperature) or the CO_2RR applied voltage. The total N content and N type are affected by the pyrolysis temperature. At temperatures below 750 °C, the total and pyridinic N content gradually increased with increasing temperature resulting in a decrease in the H_2/CO ratio; for example, at −1.0 V vs. Ag/AgCl, the H_2/CO ratio decreases from 2 to 1 by increasing the pyrolysis temperature from 650 to 700 °C (Figure 5b). This H_2/CO_2 ratio increases at a pyrolysis temperature of 800 °C (H_2/CO ratio of 3) due to the decrease of total N and pyridinic N groups, which act as the active centers for CO_2 reduction. Moreover, for all pyrolysis temperatures, the FE to CO increases as the potential increases to −1.1 V vs. Ag/AgCl (Figure 5b), and gradually decreases at higher potentials. Consequently, the H_2/CO can be also fitted to the required one for the desired industrial application by only changing the applied potential.

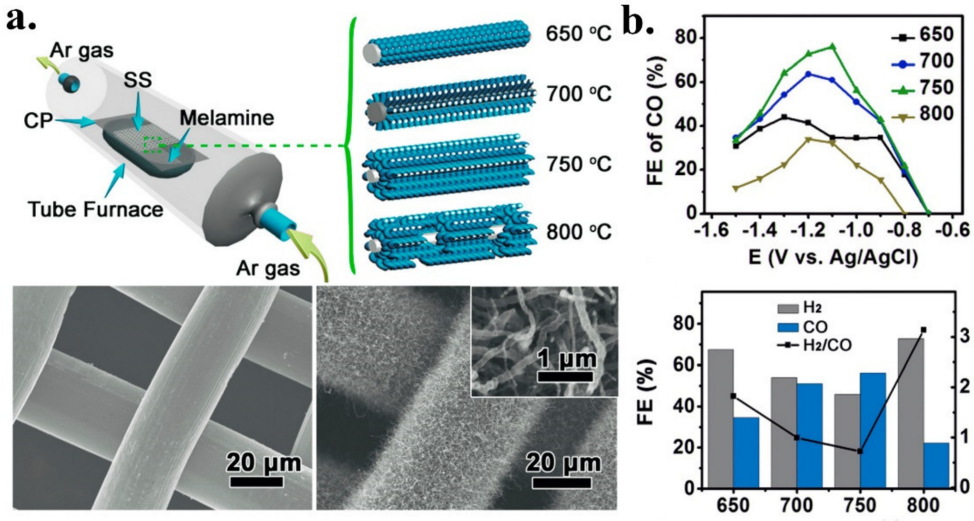

Figure 5. (**a**) Scheme of the synthesis of integrated 3D electrodes by the direct grown of N-doped carbon nanotubes on a stainless-steel mesh and SEM images. (**b**) Faradaic efficiencies for CO at various applied potentials (up) and Faradaic efficiency and molar ratio of H_2/CO of different samples at −1.0 V vs. Ag/AgCl (down). Adapted from [45].

Nonetheless, the instability of H_2/CO ratio with the applied potential is not desired when green electricity generated from renewable energy is used as energy supply for the electroreduction. The renewable energy suffers from unstable voltage output and, if the electrocatalytic performance of catalyst is voltage-sensitive, a dramatic change in the syngas composition occurs by a slight fluctuation of the energy source voltage [44]. In this sense, Li and coworkers [44] developed electrodes with tunable and potential-independent H_2/CO ratio. These electrodes consist of nitrogen-doped tubular carbon foams with a robust structure, highly open pores, and well-accessible active sites (Figure 6a) since any type of binder polymer is used that could cover the active sites. This electrode configuration enables a sufficient supply of CO_2 and breaks mass transfer limitations, that joined to the defects and nitrogen species created by the N-doping with NH_3, enables the production of tunable syngas via CO_2RR. Therefore, these electrodes act as both gas diffusers and self-supported electrocatalysts. A stable FE of CO (Figure 6b), and consequently, stable H_2/CO ratio, in a relatively wide potential window (−0.5 V to −1.3 V vs. RHE) was obtained resulting from the facile mass transport of CO_2 inside the monolithic tubular electrode. Moreover, the H_2/CO ratio can be controlled from 0.5 to 2 by controlling the NH_3 treatment time and consequently, the amount and type of N functional groups (Figure 6b). The total amount of N and pyridinic N progressively increases by increasing the NH_3 doping treatment time from 30 to 60, 90, and 120 min (samples C30, C60, C90, and C120, respectively) and consequently, the H_2/CO ratio decreases with the increase of the treatment time. In this way, after 60 min of N-doping treatment, a H_2/CO ratio

of 2 is obtained optimal for methanol and Fisher–Tropsch syntheses and this ratio can be modulated to 1 or 0.5, optimal for hydroformylation or short-chain thermochemical synthesis, respectively, by increasing the doping time to 90 min or 120 min.

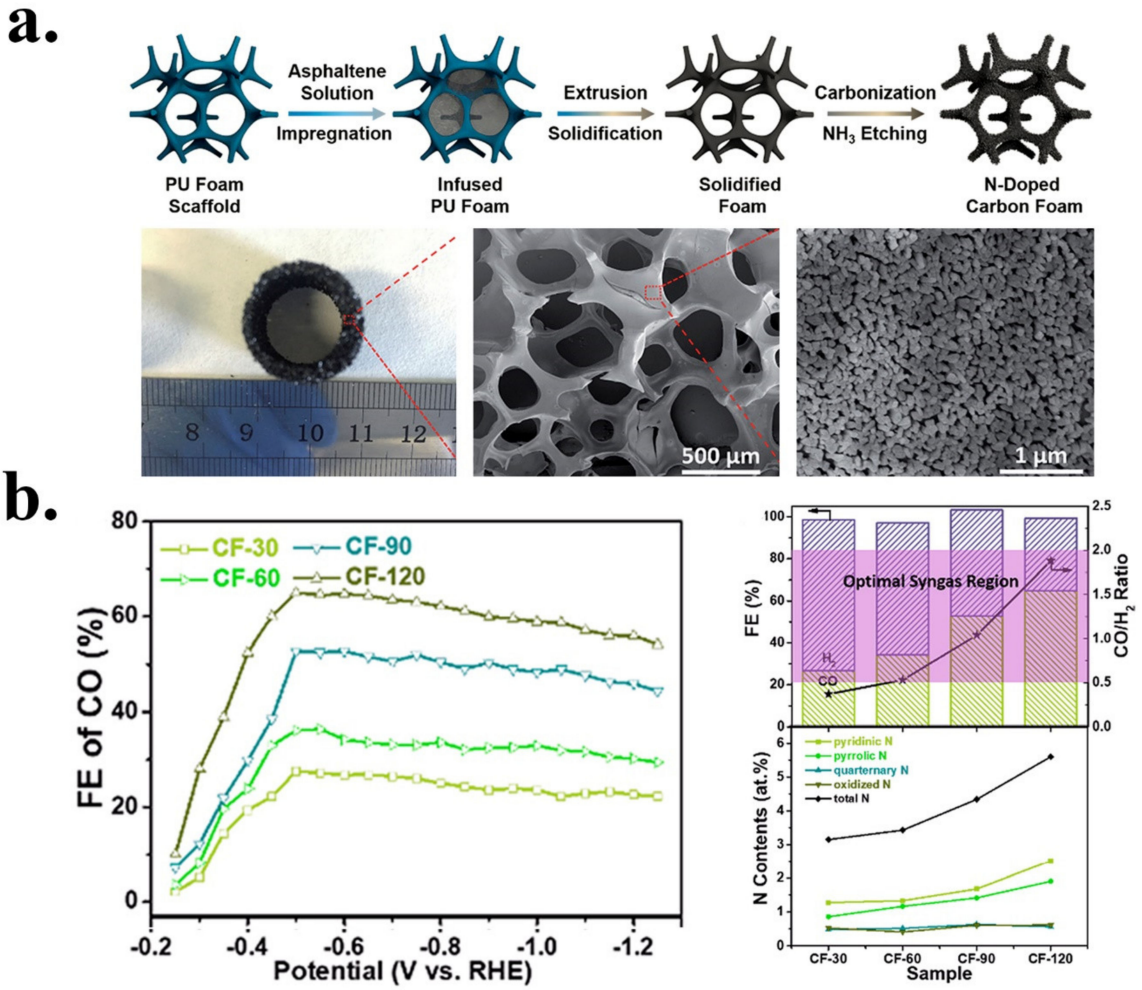

Figure 6. (**a**) Scheme of the synthesis, digital photograph, and SEM images of N-doped carbon foam (after 120 min of NH_3 etching). (**b**) Faradaic efficiencies for CO at different applied potentials (left) and Faradaic efficiencies and the corresponding proportions of syngas at −0.6 V vs. RHE as a function of N content (right). Adapted from [44].

Recently, the use of a plasma treatment has been reported as another efficient strategy for the modification of the surface of the nitrogen-doped catalyst aiming to an efficient control of the CO/H_2 ratio [24]. Ji and co-authors [24] developed N-doped nanotube arrays that were subjected to a Ar-plasma treatment during different treatment times (5, 10, 15, 25, and 40 min) to modify the surface chemistry of the N-doped carbon catalyst. They observed that both N content and the nature of the N functionalities can be adjusted by controlling the plasma treatment time. The total N remains constant at plasma treatment times lower than 10 min while for longer times the total N begin to decrease in proportion to the treatment time. The type of N species also is affected by the plasma treatment time; the percentage of pyrrolic N decreases progressively at times lower than 10 min and then drastically increases, while the percentage of pyridinic N follows the opposite trend. In this way, the H_2/CO ratio increases progressively from 1.1 to 3.03 by increasing the plasma treatment time to 10 min, and then drastically decreases to 0.55 increasing the treatment time to 40 min. According to these results, the authors speculate that the N-pyridinic species facilitate the formation of CO while the N-pyrrolic species are favorable for HER, and thus, controlling the quantity of both active sites by the plasma treatment, the H_2/CO

ratio can be regulated. It has been distinguished that the catalyst treated with Ar-plasma for 10 min obtained a high FE for CO of 75% at −0.82 V vs. RHE with a stability for more than 10 h. According to the authors, the main advantage of treating N-doped electrocatalysts with plasma is that this process is carried out at room temperature and no chemical residues are produced, so it could be an efficient and practical way to tune the syngas composition.

2.1.4. Formate and Formic Acid as Main Products

One of the first synthesized metal-free catalysts that were selective towards formate or formic acid was reported by Zhang and co-authors [41]. They prepared N-doped carbon nanotubes (CNTs) by means of a treatment with ammonia plasma at different exposure times (0, 10, 15, 20, 40, and 60 min) to control the level of doping on the catalyst surface. O-doped carbon nanotubes were also prepared in a similar way but using oxygen plasma. Pristine CNTs and O-doped CNT gave H_2 as main product (>90%) with a small amount of CO (<1%) whereas a maximum faradaic efficiency of 59% to formate was obtained for N-doped CNTs, which clearly manifests that N-doping plays a crucial role in CO_2 reduction to formate. The N content progressively increases by increasing the ammonia plasma exposure time, leveling off after 40 min of exposure. The Faradaic efficiency to formate increases by increasing the content of N up to 7.6% (20 min of exposure time) but further improvement was not obtained by increasing the N content (at higher exposures times). The addition of a co-catalyst such as polyethylamine (PEI) on the N-doped nanotubes enhances both the EF and current density for formate production obtaining an EF of 85% and a more positive starting overpotential. This improvement was explained based on the role of the PEI layer: (i) PEI overlayer may stabilize $CO_2^{\bullet}$ by a H-bond interaction, and (ii) PEI is known for its CO_2 adsorption capacity, therefore, the PEI layer can concentrate CO_2 on the catalyst surface, increasing its local effective concentration [69]. It is worth highlighting that in this study, they found that this co-catalyst was not efficient if the material was not doped with nitrogen. Later, Wang and co-authors [40] reported a formate-selective electrocatalyst (73%) using only metal-free nitrogen-doped graphene without any extra co-catalyst. For the synthesis of this catalyst, graphene oxide and melamine were used as carbon and nitrogen precursors, respectively, which were subjected to high pyrolysis temperatures. According to the XPS characterization, it was found that the samples had a high percentage of N-pyridine species (3.0 at %) followed by graphitic (1.6 at %) and pyrrolic N (0.9 at %). According to the authors, pyridinic N were responsible for the performance of the electro-catalyst, since having this type of nitrogen species the adjacent carbon atoms could be substantially positively charged in their oxidized form and generate suitable sites for the reduction reaction [70], then a good balance between the FE and the applied overpotential was obtained.

Another formate-selective catalyst with a higher EF (81%) was developed by Hong Wang and co-authors [42]. They synthesized N-doped carbon membrane (HNCM) and N-doped nanoporous-carbon/carbon-nanotube composite membrane (HNCM/CNT) that work as both CO_2RR catalyst and binder-free gas diffusers, improving contact and charge transport between the electro-catalyst, the aqueous electrolyte, and the gaseous reagent CO_2. Despite that the total N content in both alone and composite membranes is similar (8.5 ± 0.2 at %), the distribution of N species is quite different. N graphitic species (84.9%) abound in HNCM membrane whereas pyridinic and graphitic species are in abundance (41.8% and 58.2%, respectively) in HNCM/CNT composite membrane. This higher pyridinic N content in HNCM/CNT is attributed to the surface templating of the condensation reactions in conjunction with coupled edge termination of graphitic layers by pyridinic units. Therefore, the incorporation of CNT favors the selective formation of pyridinic N species, presumably through topology and electronic interactions. This different distribution of N species clearly affects the activity and selectivity of membranes. HNCM/CNT exhibits a more positive overpotential and a larger current density than HNCM. The main product obtained using both membranes is formate, however the FE to formate increases when CNTs are introduced; FE to formate were 81% and 41% for HNCM/CNT and HNCM, respectively.

This different FE suggest that the N species distribution is very important to control the selectivity, so that the increase of the amount of pyridinic N improves the CO_2RR activity and selectivity to formate formation in aqueous solution.

Recently, a highly selective electrocatalyst for the CO_2RR to formate (92%) based on N-doped fullerene derivative material (C61) was developed by Chen and co-authors [43]. This electrocatalyst was synthesized by pyrolysis of pristine PC61BM ([6,6]-phenyl-C61-butyric acid methyl ester) and urea (Figure 7a) at different temperatures (500–1000 °C). The authors observed that the relative percentage of the different types of N-species greatly depend on the pyrolysis temperature. At low pyrolysis temperatures (500 and 600 °C), pyrrolic N species are the majority species (around 48%), but this percentage decreases as the temperature increased, completely disappearing at 1000 °C, being converted into pyridinic N (70%) and graphitic N (30%). In turn, the fraction of N-graphitic species increases by increasing the temperature up to 800 °C and then decreases whereas N-pyridinic is almost constant up to 800 °C and then increases. The total current density is not significantly affected by the pyrolysis temperature, however the FE to formate is clearly affected by the temperature and, as a consequence, by the different species distribution (Figure 7b). The maximum formate FE vs. pyrolysis temperature follows a similar trend than the graphitic N content, whereas no such trend is obtained for pyridinic N and pyrrolic N. That could indicate that graphitic N-species are the most active sites for formate formation, although the contribution to electro-catalytic performance of pyridinic and pyrrolic N-defects cannot be ruled out.

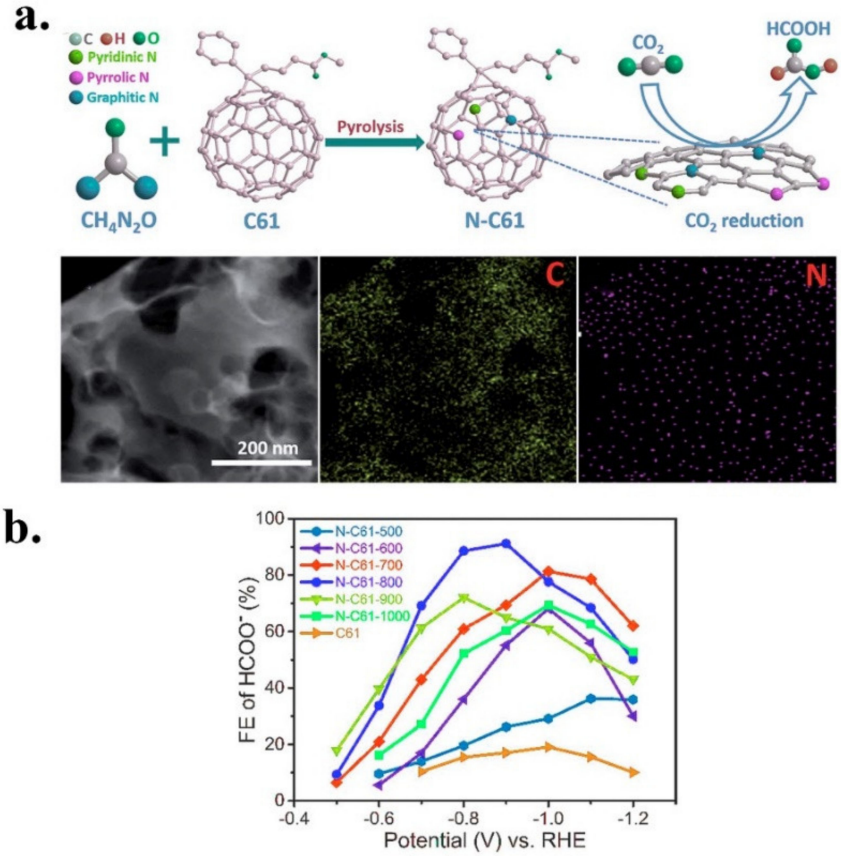

Figure 7. (**a**) Scheme of the synthesis of N-doped C61, SEM images and EDX mapping. (**b**) Variation of the maximum formate FE with the potential for the different samples. Adapted from [43].

Lui and co-authors [52] carried out a computational study of the reduction of CO_2 to HCOOH on nitrogen-doped graphene catalysts. These theoretical computational studies conducted by DFT revealed that N doping can modify the electronic properties of graphene, resulting in a low energy barrier for the formation of the intermediate COOH, in addition

to the strong adsorption energy of this intermediate and the weak adsorption energy of CO or HCOOH allowing a high selectivity of the products. Within the nitrogen configurations in graphene, computational studies showed that N-pyrrolic (PyrroN3) has a better catalytic performance due to its low over-potential of 0.24 V, exclusively leading to HCOOH as the main product.

2.1.5. Multi-Carbon Products

As commented, to obtain catalysts able to obtain multi-carbon products by CO_2RR in a multiple-step electron transfer pathway, a stabilization and strong adsorption of the initial C1-type intermediates (CO or HCOOH) is required to continue reducing them [56] and the catalyst must be capable of accepting a multi-electronic transfer from 4 to 12 electrons [71,72]. However, N-doped carbons usually cannot stabilize those C1-type intermediates to their further coupling to generate multi-carbon products [46]. Consequently, CO and COOH have been the main products obtained when using N-doping carbon materials. Therefore, to date, reports on developing efficient N-doped carbon materials for CO_2RR to multi-carbon products are extremely scarce. Despite this, some investigations dealing mainly on the development of N-doped carbon nanostructures for the CO_2RR to ethanol or acetone can be found.

Liquid multi-carbons products (ethanol and acetone) were selectively obtained by Yuan and co-authors [48] using functionalized graphene oxide (GO) as electrocatalysts. GO was functionalized with vitamin B6 (VB6) as a nitrogen resource due to its low cost and its high content of hydroxyl groups, which serve as a bridge to bond with the carboxyl groups of GO facilitating nitrogen doping. In order to draw a comparison, GO was also functionalized with other pyridine derivatives: Hydroxypyridine (X-1), 4-aminopyridine (X-2), 8-hydroxyquinoline (X-3), and 5-amino-1,10-phenanthroline (X-4). All pyridine derivatives were successfully grafted on the GO sheets surface. The authors demonstrate that the electrocatalytic performance of the functionalized GO in the CO_2RR is closely associated with the content of modified pyridinic N and the special structure of grafted pyridine derivative. GO-VB6 present the highest FE to the formation of ethanol and acetone (45.3 at %, –0.40 V vs. RHE). Despite GO-X-1, GO-X-2, and GO-X-4 having similar pyridinic N % (2.764%, 2.540%, and 2.426%) than GO-VB6 (2.314%), they show lower total FEs (17.9%, 16.4%, and 3.1 at %−0.40 V vs. RHE, respectively). This different electrocatalytic behavior indicates that the structure of grafted pyridine derivatives plays a crucial role. VB6 molecule contains strong electron donating groups, such as -OH and -CH_3, which could increase the electronegativity of the pyridinic N and, consequently, favor the CO_2 adsorption or reaction. X-1 and X-2 also have one strong electron-donating group (-OH or -NH_2), however these are converted into -COO^- or -$CONH^-$ during the functionalization process. In the case of X-3 and X-4, these pyridine derivatives have an extra benzene ring that linked to the pyridinic N, which have ability to disperse the electrons producing a further attenuation of the electronegativity of pyridinic N and thus weakening the ability of CO_2 adsorption and reduction.

Song and co-authors [46] developed N-doped carbons with cylindrical channel configuration (Figure 8a) that are able to completely suppress the CO_2RR to CO and, thus, being highly selective to ethanol with FEs ranging between 73 and 77% at the potentials from −0.40 to −0.56 V. This catalyst consists on an ordered mesoporous N-doped carbon (c-NC) with an interconnected network of cylindrical mesopores synthesized by soft-template method using resol as carbon resource, F127 as soft-template, and dicyandiamide as nitrogen resource [73]. The superior electrocatalytic activity of the N-doped mesoporous carbon for the CO_2RR to ethanol is ascribed to the synergetic effect of the nitrogen heteroatoms and the cylindrical channel configurations. DFT calculations reveal that pyridinic N and pyrrolic N sites are required for the generation of CO* intermediates because pure carbon and graphitic N sites are highly unfavorable for generating those intermediates. The high-electron-density surface of the cylindrical surface favors the stabilization of these adsorbed CO* intermediates enabling the subsequent C-C coupling and proton–electron

transfer reactions for the ethanol formation. However, despite the high ethanol selectivity, this nitrogen-doped mesoporous carbon catalyst exhibited a low ethanol production rate. In order to increase this production rate, the same researchers [47] prepared similar N-doped mesoporous catalysts but with micropores embedded in the ordered mesoporous walls (Figure 8b). The development of medium micropores on the mesopores walls of the ordered mesoporous N-doped carbon was carried out by adding a silica precursor (tetraethylorthosilicate, TEOS) during the synthesis and its subsequent removal from the synthesized intermediate carbon-silica composite. Only narrow micropores (of about 0.52 nm) were dispersed inside the channel walls of ordered mesoporous carbons prepared without TEOS ascribed to the de-gassing during the carbonization process of carbon synthesis. However, the addition of TEOS gave medium micropores (0.84 nm) inside the channel wall of carbon derived from the silica removal. Moreover, the variation of the mass of TEOS allowed to optimize the content of the micropores in the catalyst; the surface area increases from 187 to 642 m^2 g^{-1}, and the medium micropore content from 24 to 46% by increasing the mass of TEOS from 0.27 to 1.04 g. Catalytic results have shown that a high EF (78%) for ethanol production is still maintained in micropore-embedded ordered mesoporous N-doped carbons but the presence of those medium micropores significantly enhanced the ethanol production rate; the higher the medium micropore volume is, the higher the ethanol yield is, obtaining an ethanol production rate as high as 2.3 mmol g_{cat}^{-1} h^{-1} for samples with the highest volume of medium micropores. This improved catalytic activity is mainly since medium-sized microporous structures with pyridine and pyrrolytic N sites result in fast charge transfer kinetics and high electrical conduction potentials. Therefore, the synthesis of electrocatalysts with well-engineered structures seems to be an effective strategy to act on the stabilization of key intermediates and thus to enable the C-C coupling leading to the highly desired multi-carbon products.

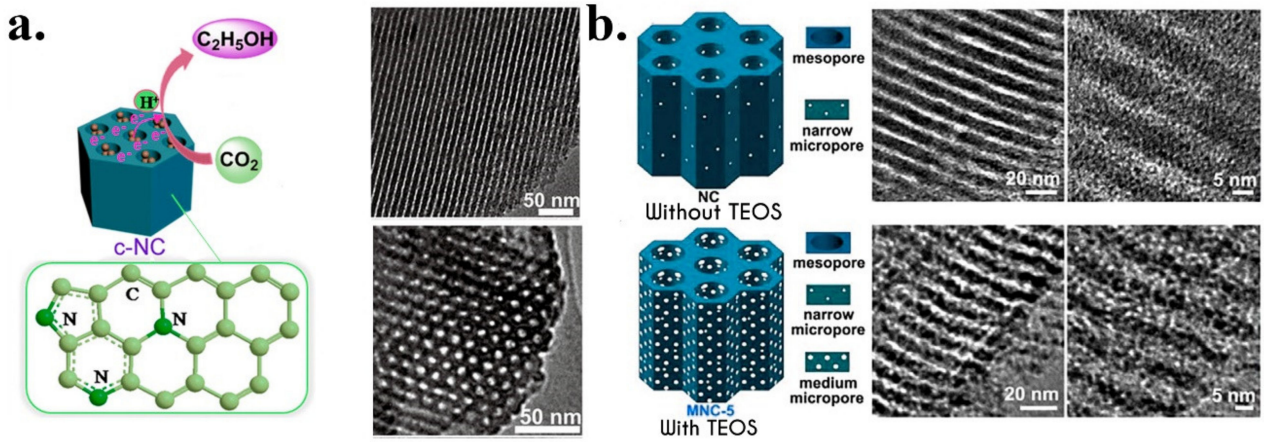

Figure 8. Pore structure illustrations and TEM images of (**a**) ordered mesoporous N-doped carbon adapted from [46] and (**b**) micropore-embedded ordered mesoporous N-doped carbons adapted from [47].

The miniaturization of carbon size is another alternative to obtain multi-carbon products by the design of the carbon architecture. Wu and co-workers [54] demonstrated that nanometer-size N-doped graphene quantum dots (NGQDs) enabled CO_2 electroreduction to multi-carbon products including ethylene, ethanol, and n-propanol with promising selectivity, high FE, high current densities, and low overpotential. The total FE of CO_2 increases by increasing the negative applied voltage reaching the maximum value of 90% at −0.75 V (vs. RHE). At low cathode potential (such as −0.26 V), C1, CO and $HCOO^-$ are the main products, however as a more negative potential is applied, C2 hydrocarbons (ethylene) and multi-carbon oxygenated (ethanol, acetate, and n-propanol) are also produced, reaching a FE of around 30% and 35%, respectively (at −0.75 V vs. RHE). The unprecedented activity and selectivity of NGQDs is explained based on the unique nanostructure in combination with most exposure of edge sites and heteroatom N doping. The crucial role of the tuning

of the dimensions and morphology of carbon nanostructure into nanometer scale was furthermore corroborated by comparing the catalytic performance of NGQDs and N-doped reduced GO (NRGO). NRGO presented a similar concentration of each N functionality than NGQDs but larger micrometer-scale lateral size and, consequently, NRGO primarily catalyzes CO_2RR to form CO without appreciable formation of multi-carbon products (<10%). This comparison clearly pointed out that the morphology determines the CO_2RR activity of carbon nanostructures towards multi-carbon products. Wu and co-workers [74] also performed DFT simulations to understand how NGQDs catalyze the CO_2RR to hydrocarbons and oxygenates. They found that N atoms in edges of NGQDs enhances their bonding with *COOH *COOH, endowing its higher performance in converting CO_2 to CO. The selective production of CH_4 over CH_3OH was explained based on the formation of the key intermediate of $*CH_2$ due to a much lower kinetic barrier for the conversion of adsorbed $*CH_2OH$ to $*CH_2$, in which further hydrogenation would produce CH_4. In the subsequent step, the effective coupling between $*CH_2$ and CO leads to various C2 products including C_2H_4 and C_2H_5OH.

2.2. Others-Doped Carbon-Based Materials

Other heteroatoms studied to enhance the catalytic activity of carbon materials in the electroreduction of CO_2, although to a lesser extent than N, are boron, phosphorus, and fluorine since, just like nitrogen, they can modify carbon electronics properties enhancing the electrochemical performance. Sreekanth and co-authors [75] probed that boron-doped graphene is a good candidate for CO_2RR to formic acid/formate. A B-doped graphene catalyst with a boron surface content (detected by XPS) of 4.1 at. % was synthesized by annealing a mixture of graphene oxide and boric acid at 900 °C under Ar Atmosphere. This catalyst is able to catalyze the CO_2RR to formate (FE of 66% at −1.4 V vs. SCE) at low overpotentials remaining stable without any degradation. DFT calculations evidence that the B-doping introduces asymmetric charge and allows a spin density distribution throughout the system. This positive spin density on the atoms of B and C suggests that both atoms are catalytically active and available for chemisorption.

Boron-doped diamond (BDD) has been widely studied for CO_2 reduction (Figure 9). Diamonds are electrical insulators, but when part of carbon atoms are substituted by boron, diamonds become conductive [76]. Consequently, BDD are presented as promising electrode materials because they combine good electrochemical properties, such as wide potential window and low overpotentials that allow the suppression of HER, with the additional advantages provided by the original diamond properties such as chemical inertness and mechanical durability [77]. Einaga and co-authors [78] have deeply studied how the BDD properties and electrocatalytic conditions affects the activity and products selectivity. The electrochemical activity and selectivity of BDD depend on the doping level, the presence of sp^2 carbon, and the electrolyte. In fact, formaldehyde, methanol, formic acid, or carbon monoxide can be produced depending on the conditions such as electrolyte and boron content (Table 4). Methanol was selectively produced with a FE of 24.3% in aqueous ammonia solution using BDD [79]. The authors pointed out the important role of ammonia and pH in the CO_2RR to methanol. In aqueous solution, CO_2 reacts with NH_3 forming bicarbonate or carbonate ions. The pH determines the species that is dominant in the solution: Dissolved CO_2 dominates at pH < 5, bicarbonates ions dominate at 7.5 < pH < 9, whereas carbonate ions are the dominant species at pH > 12. Methanol was the main products when CO_2-saturated aqueous ammonia electrolyte was used (pH of 7.7) and also when NH_4HCO_3 aqueous solution (pH 7.9) was used without CO_2 bubbling. However, methanol was not detected when pH of the NH_4HCO_3 aqueous solution was adjusted to pH < 4 or pH > 10 by the addition of HCl and NaOH, respectively. This suggests that the methanol production is attributed to the electrochemical reduction of bicarbonate ions formed by the CO_2 and ammonia reaction and not dissolved CO_2 or carbonate species. This study has a practical meaning in the electroconversion of industrially stored-CO_2 (HCO_3^-) for which amine-based solutions for CO_2 scrubbing

systems are usually used. Nevertheless, when using methanol, aqueous NaCl, or seawater as electrolyte, formaldehyde was obtained as the main product [78]. The maximum FE (77 at % −1.5 V vs. Ag/Ag^+) to formaldehyde was obtaining using methanol saturated with CO_2 as electrolyte. The formation of this product is mainly due to the presence of sp3 carbon bonds in the BDD electrode that can be beneficial for the reduction of CO_2 to formaldehyde. To confirm this point, the authors also synthesized a BDD with a large number of sp2 bonds and a very low faradic efficiency of 15 at % −1.5 V vs. Ag/Ag^+ in MeOH was obtained. Therefore, sp3 carbon bonds can be the active sites for obtaining formaldehyde. Lower FEs were obtained when using seawater (36%) and aqueous NaCl (62%) as electrolyte. The lower FE in seawater was attributed to the narrow potential window in water and the inorganic and organic impurities of seawater. Nevertheless, the formaldehyde production rate in seawater is 7.5×10^{-3} M per hour, which allows the production of formaldehyde by an entirely environmentallyfriendly process from CO_2 and seawater if, moreover, the required electrical energy is obtained from solar cells.

Table 4. Carbon and boron precursors to construction of electrocatalysts and active sites.

Sample	Main Product	DopingAtom	Carbon Precursor	Heteroatom Precursor	Doping Type	Synthesis Method	Active Site/Heteroatom Content	Ref
BG	Formate	B	graphene oxide	Boric acid	In situ	Direct solid state/thermal annealing	B y C atoms/4.1 at % (XPS)	[75]
BDD	Methanol	B	Acetone	Trimethosyborane $B(OCH_3)_3$	In situ	Plasma assisted chemical vapor deposition	Bicarbonate ions/B/C ratio 1%	[79]
BDD	Formaldehyde	B	Acetone	$B(OCH_3)$	In situ	Microwave plasma assisted chemical vapor deposition (MPVCD)	Sp3- bonded carbon/B/C atomic ratio 1.0 *w*/*w*	[78]
BDD	HCOOH	B	Acetone	Trimethosyborane $B(OCH_3)_3$	In situ	Microwave plasma assisted chemical vapor deposition (MPVCD)	n.d.	[80]
BDD	HCOOH	B	Acetone	Trimethosyborane $B(OCH_3)_3$	In situ	Microwave plasma assisted chemical vapor deposition (MPVCD)	B/C atomic ratio 1 *w*/*w*	[81]
BDD	HCOOH	B	CH_4	Trimethylboron	In situ	Microwave plasma assisted chemical vapor deposition (MPVCD)	n.d.	[82]
BDD-0.01%	HCOOH	B	CH_4	Trimethosyborane $B(OCH_3)_3$	In situ	Microwave plasma assisted chemical vapor deposition (MPVCD)	B atoms/B/C ratio 0.01%	[83]
BDD	HCOOH	B	CH_4	Trimethylboron	In situ	Microwave plasma assisted chemical vapor deposition (MPVCD)	B atoms/B/C ratio 1% and 0.1%	[84]
BDD	HCOOH	B	CH_4	Trimethosyborane $B(OCH_3)_3$	In situ	Microwave plasma assisted chemical vapor deposition (MPVCD)	B/C ratio 0.07%	[85]
FC	CO	F	BP 2000 (commercial carbon nanomaterial)	Polytetrafluoroethylene (PTFE)	In situ	Pyrolysis	C atoms close to CF_2 bonds/0.32% Atomic	[86]
F-CPC	CO	F	Resorcinol and formaldehyde (Aldol reaction)	Polytetrafluoroethylene (PTFE)	In situ	Template method (SiO_2)	Semi-ionic C-F bond/0.65% atomic	[87]
P-OLC-IP	CO	P	Onion-like carbon (nanodiamond power)	Diammonium hydrogen Phosphate $(NH_4)_2HPO_4$	Post-doping	Impregnation	P-O/2.8% atomic	[88]
P-OLC-CVD	CO	P	Onion-like carbon (nanodiamond power)	Triphenylphosphine (TPP)	Post-doping	Chemical vapor deposition CVD	P-C/3.8% atomic	[88]

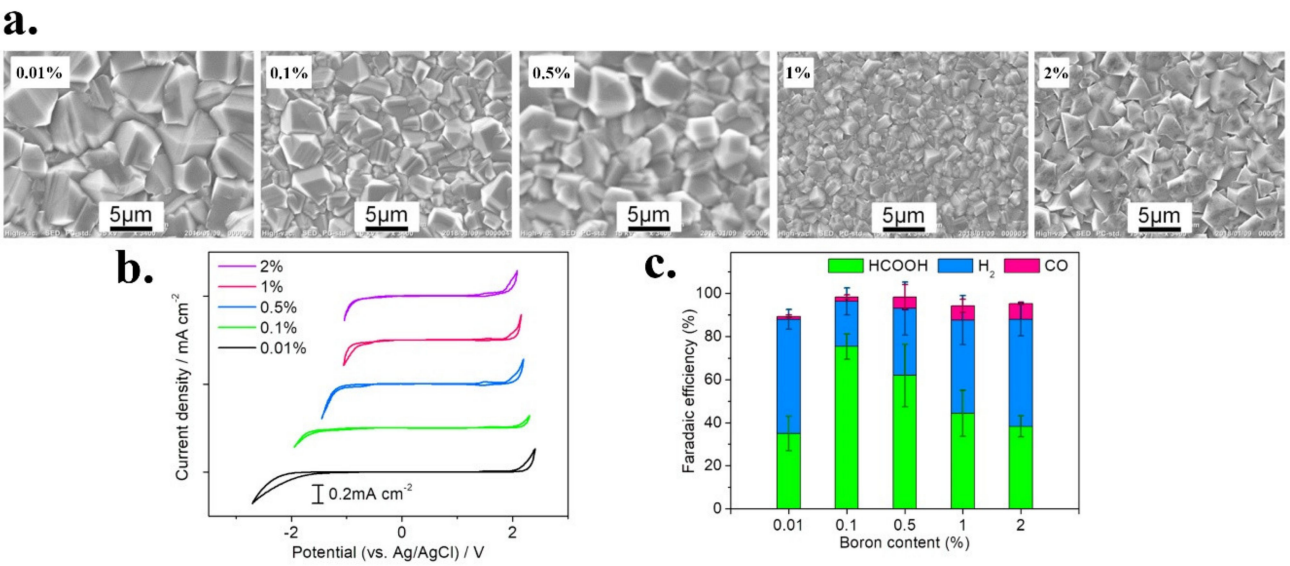

Figure 9. (**a**) SEM images of Boron-doped diamond (BDD) electrodes with different boron content. (**b**) Cyclic voltammetry (CV) curves of BDD electrodes in 0.1 M H_2SO_4 at a scan rate of 0.1 V s^{-1}, (**c**) Faradaic efficiencies to formic acid. Adapted from [83].

Therefore, the electrolyte strongly affects the selectivity and the FE in the CO_2RR using BDD. To elucidate the influence of the electrolyte, Einaga and co-authors [81,82] also studied the impact of various cations and anions on the CO_2RR to formic acid using BDD electrodes in a two-compartment H-type cell. The pH was first fixed to maximize the formic acid production before analyzing the effect of the alkali metal cations using 0.05 M RbOH as electrolyte [81]. As commented before, CO_3^{2-}, HCO_3^-, or H_2CO_3 are formed upon dissolving CO_2 and the dominant specie strongly depends on the solution pH. The pH of the CO_2-saturated RbOH electrolyte was around 7, at which a FE for the formation of formic acid of around 25% was obtained. This FE increases by the neutralization of the electrolyte solution with HCl up to the optimum pH of 6.2 at which the maximum FE was 66%. This indicates again that HCO_3^- is the key species for the formation of formic acid on the surface of the BDD electrode. Once the optimum pH was fixed, the effect of alkali metal cations (M = Li^+, Na^+, K^+, Rb^+ and Cs^+) of the electrolyte was studied [81,82]. The faradaic efficiency for producing formic acid is intimately related to the alkali metal cation size. High FE to formic acid was obtained using large cations (K^+, Rb^+, and Cs^+) whereas HER is promoted using small cations (Li^+ and Na^+) instead of CO_2RR. This is attributed to the buffer effect of hydrated alkali metal cations, which would keep the pH near the cathode suitable for CO_2RR. This buffer effect is more efficient for large cations than small cations due to the weaker interaction of large cations with water leading to the decrease of pKa for cation hydrolysis and thus, emitting oxonium ions in a more efficient way than small cations, which suppress the increase of pH and keep the CO_2 concentration high near the cathode resulting in progress of CO_2RR. The effect of the addition of anions was also studied. For that, K^+ was selected since formic acid was effectively produced and, therefore, different potassium salts were selected to study the anions effect such as KNO_3, KSO_4, KCl, KBr, and KI. Low activity for both CO_2RR and even HER was obtained when using NO_3^-, whereas formic acid is effectively produced (with a FE higher than 75%) when using SO_4^{2-}, Cl^-, Br^-, and I^- being the highest FE obtained in KCl solution (FE around 92%). The low activity of NO_3^- for CO_2RR and even HER was attributed to the electrochemical reduction of nitrate ions on the BDD electrode which reduce the electrons available for other electrochemical reactions and thus suppress the CO_2RR or

HER. Conversely, the other anions specifically adsorb on electrode and restrict the CO_2 movement to the electrode vicinity favoring the electrons transfer to CO_2.

Greater efficiency in the production of formic acid was obtained on BDD using a circulation flow cell instead a two-compartment batch cell. A maximum FE to formic acid of only 71% was obtained using alkali metal solution in a two-compartment batch cell [81]. Nevertheless, HCOOH was obtained with a high faradic efficiency of 94.7% in a two-compartment flow cell [80]. This better performance is attributed to the increase in the electrolyte flow rate that improved the CO_2 mass transport on the BDD surface. Although much more remains to be clarified about the mechanism and the effect that boron doping has on the electrochemical reduction of CO_2, the authors mention that the selectivity of the catalyst is probably due to the low binding capacity between the boron doped diamond and the intermediates.

With the aim of further clarifying the role of B-doping on BDD electrodes, Einaga and co-authors [83] also investigated the effect of the boron content in the electrocatalytic performance of the BDD electrodes. Five BDD samples (Figure 9a) were prepared with a different content of boron (B/C of 0.01%, 0.1%, 0.5%, 1%, and 2%) by microwave plasma-assisted chemical vapor deposition using $B(OCH_3)_3$ and CH_4 as boron and carbon source, respectively. The boron content alters the adsorbability of CO_2 and its intermediates and the tensile stress of the BDD electrodes and, consequently the activity and selectivity in the CO_2RR. The study of the potential window was carried out through cyclic voltammetry (VC) in 0.1 M H_2SO_4. A narrowing of the potential windows with increasing the boron content was obtained (Figure 9b). A wide potential window can be favorable for CO_2RR because HER in aqueous electrolytes can be suppressed. The performance of samples in HER was analyzed by Linear Sweep Voltammetry (LSV) after N_2 saturation. The current density increases by increasing the boron content indicating that the HER is favored according to the narrowing potential window obtained. Therefore, low boron content would be an advantage for reducing CO_2, because the increasing of the boron content favors the hydrogen production. This observation was reflected in the faradic efficiency for the formation of products (Figure 9c). Formic acid and H_2 were the main products, but as expected, the FE for the production of formic acid decreases at the expense of the increase of the H_2 production by increasing the boron content. The maximum FE for the production of formic acid is obtained (75%) with a low boron content on BDD of 0.1 %. However, at very low doping levels such as 0.01%, the electrochemical reactivity is too low and therefore the FE for formic acid and even CO was the lowest.

The CO_2 reaction mechanism on BDD was also discussed by Einaga and co-authors [83] and a possible two-step mechanism is proposed (Figure 10). The first step is the CO_2 electroreduction with an electron to the CO_2^{*-} intermediate and the second step is the formation of HCOOH or CO depending on the adsorption strength of the CO_2^{*-} intermediate. If the CO_2^{*-} intermediate can be hardly absorbed in the electrode, formic acid is produced, whereas if the intermediate CO_2^{*-} can be adsorbed, CO is obtained. According to this mechanism, the high FE to produce formic acid of BDD can be attributed to its chemical inertness and its low binding capacity with the intermediate [80]. The increase of boron content increases the adsorption of organic compounds on BDD decreasing the FE to produce formic acid but increasing the production of CO.

According to this mechanism, the product selectivity can be switched from formic acid to CO by controlling the adsorption of the CO_2^{*-} intermediate on BDD, for which the electrolyte and boron concentration of the BDD electrode are key factors [84]. The composition of the electrolyte modifies the CO_2^{*-} adsorption strength, so the product selectivity can be modified by changing the electrolyte. At this sense, the authors manage to selectively produce formic acid or CO by changing the electrolyte from KCl to $KClO_4$. In situ attenuated total reflectance-infrared (ATR-IR) measurements showed that $CO_2^{\bullet-}$ intermediates are adsorbed on BDD in $KClO_4$ therefore favoring the production of CO, whereas $CO_2^{\bullet-}$ intermediates mostly exist as free intermediates in the case of KCl promoting the formation of formic acid (Figure 11).

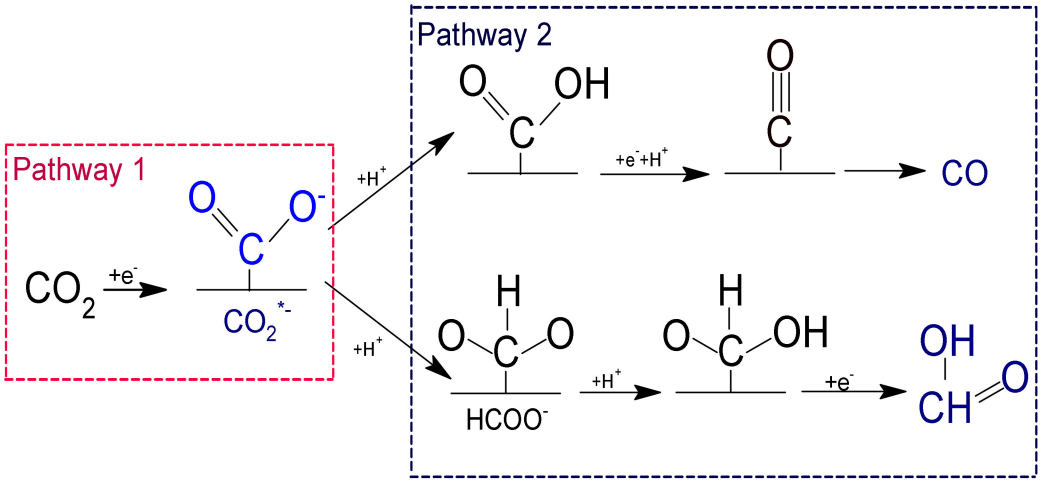

Figure 10. The CO_2 reaction mechanism on BDD.

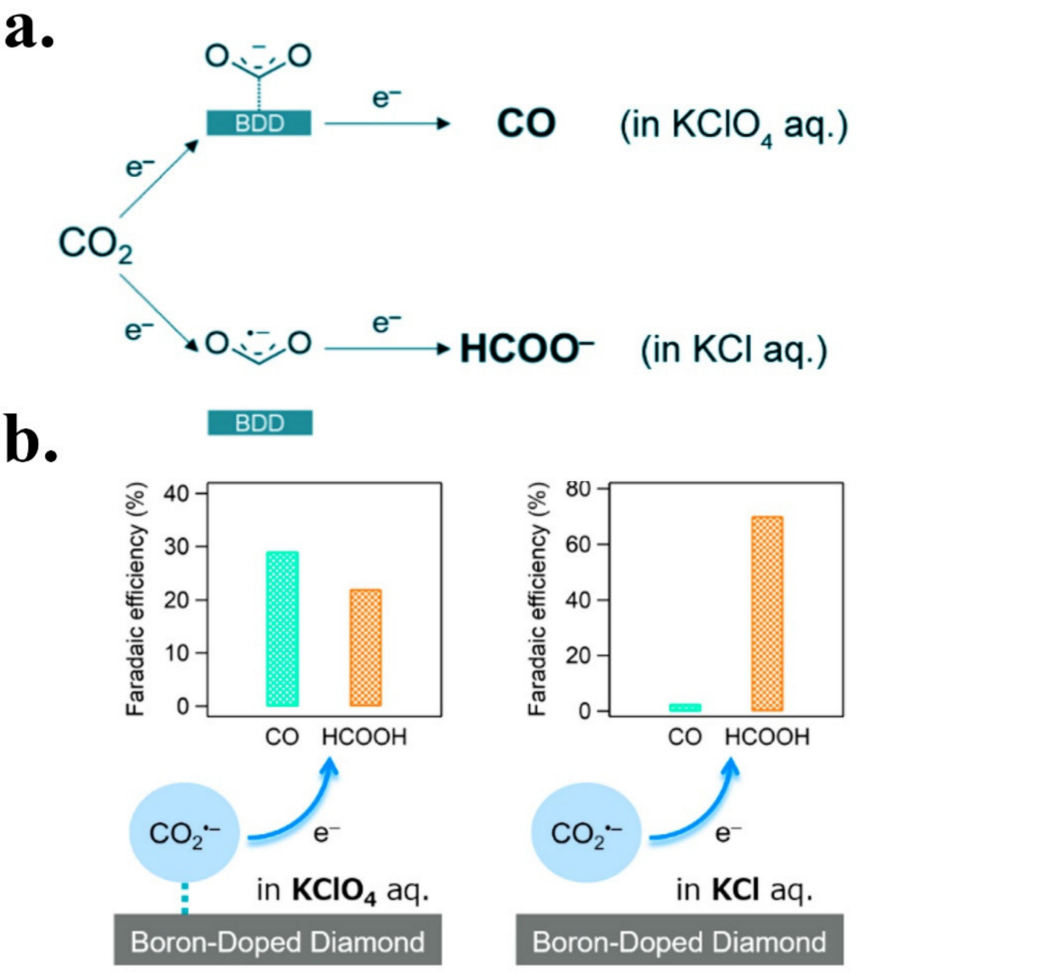

Figure 11. (**a**) Possible reaction pathway of CO_2 reduction using BDD electrodes in $KClO_4$ and KCl aqueous and (**b**) effect in the FE for acid formic and CO. Adapted from [84].

The effect of sp^2 carbon in BDD on the CO_2RR catalytic performance was also investigated by these authors [85]. They found that the content of sp^2 carbon significantly affects the CO_2RR selectivity. In absence of sp^2 carbon, formic acid is the major product (FE of 84%) and minor production of H_2 is obtained (11%) whereas when using BDD with a high amount of sp^2, H_2 is the major product (68%) with low efficiency to produce formic acid

(16%). Therefore, the increase of sp^2 content produces an increase in the production of H_2 and decreases the production of formic acid. This indicates that the CO_2RR is developed much better than HER on a sp^3 surface. Moreover, despite that FE for CO production is lower than 10% in all cases, it is observed that the presence of sp^2 favors the CO generation. According to the previously described mechanism, the authors suggest that $CO_2^{\bullet-}$ intermediates adsorb more easily on sp^2 surface decreasing the formic acid production and favoring the CO generation, although further investigation is required.

Another promising metal-free electrocatalysts for CO_2RR is C_3N doped with different heteroatoms. The possibility of using C_3N doped with heteroatoms as a metal-free electrocatalyst has recently been studied due to its mechanical, thermal, and chemical properties, which has led it to be used in different applications. Zhao and co-authors [89] carried out a theoretical study by means of density functional theory (DFT) calculations to analyze which among the B, P, Si, and S is the most promising doping heteroatom to improve the electrocatalytic properties of the C_3N carbonaceous material in the electrochemical reduction of CO_2. The analysis of the relationship between the formation energy and type of doped atom (Figure 12a) reveals that the incorporation of heteroatoms into C_3N is favorable according to the negative value of formation energy. Nevertheless, the incorporation of B and P atoms is more favorable by the substitution of N atoms of the material (B_N, P_N) rather than C atoms, whereas for heteroatoms such as Si and S, the substitution of C atoms is more favorable (Si_C, S_C). To analyze the performance of these heteroatoms doped C_3N materials for CO_2RR, it is important to analyze the free energy of formation of COOH*/HCOO*, which is the first step for CO_2RR, to determine the catalyst ability to activate the CO_2 molecule (Figure 12b). The ΔG value of HCOO* adsorption on the C–N site is 0.60, whereas B_N and Si_C-doped C_3N catalysts exhibit higher chemical activity toward HCOO* formation since $\Delta G < 0.60$ eV. The second step is the further reduction of intermediates and so, by evaluating the free energies of these further reduction, it is concluded that CO_2RR catalyzed by B_N-doped C_3N is more favorable than Si_C-doped C_3N. Moreover, considering HER (Figure 12b), the ΔG of the HER on B_N-doped C_3N (0.53 eV) is higher than that of the formation of HCOO* (0.28 eV), which is the rate-determining step of CO_2RR and consequently, HER cannot compete with CO_2RR on B_N-doped C_3N, whereas SiC-doped C_3N has high activity for HER (ΔG of -0.06 eV). All of this indicates that C_3N materials doped with boron (B_N-C_3N) can be promising metal-free catalysts for reducing CO_2 to HCOOH.

Xie and co-workers [86] used polytetrafluoroethylene (PTFE) as a fluorine doping agent to dope a commercial carbon black (BP-2000) by pyrolysis of a mixture of both carbon and fluorine sources. This procedure allowed to produce fluorine-doped carbons (CF) with abundant defects, a high surface area (1541 $m^2\ g^{-1}$), wide pore size distribution, and traces of CF2 and CF bonds. These characteristics allow to obtain a good electrochemical performance with a high FE towards CO (FE = 89.6% at 0.62 V vs. RHE) at a low overpotential (510 mV) and a low Tafel slope (81 mV dec^{-1}) indicating fast reaction kinetics for the single-electron transfer for CO_2 reduction on CF. In addition, a suppression of HER has been observed by doping the pristine carbon with fluorine atoms. DFT calculations indicate that the fluorine insertion into the graphite lattice can activate neighboring carbon atoms with highly positive charges and asymmetrical spin densities, which reduces the high energy barriers to form the COOH* intermediate compared to pristine carbon without fluorine (Pristine C) and also produce a suppression of HER leading a better performance of fluorine doped carbon for CO_2RR.

Nie and co-workers [87] also prepared fluorine-doped commercial carbon (F-PS) catalysts by pyrolyzing a mixture of commercial BP 2000 and PTFE and compared its electrocatalytic performance with structured F-doped carbon materials to analyze the effect of the carbon morphology. With this aim, they synthesized advanced fluorine-doped cage-like porous carbons (F-CPC) by a controlled polymer-derived method (Figure 13). For that, silica particles were used as template whose surface was covered with organic gel obtained by sol-gel polymerization of resorcinol and formaldehyde in presence of PTFE as

fluorine source. The corresponding carbon-base material was obtained by carbonization of the silica covered polymeric precursor at 900 °C. Finally, the silica template was removed by HF treatment (F-HCS). Part of the F-HCS sample was then activated at 1200 °C with CO_2 in order to create open pores on the carbon shell (F-CPC). In order to draw a comparison, F-doped carbon spheres (F-CS) were synthesized in a similar way, but without using the silica template precursor. Clearly, the textural properties of these samples were quite different (Figure 13b–g). F-CS and F-HCS presented a moderate surface area, 577.8 and 616.6 $m^2\ g^{-1}$, respectively, whereas higher surface area was obtained for F-CPC (1550.4 $m^2\ g^{-1}$) and F-PC (848.5 $m^2\ g^{-1}$). Thus, F-CPC presented a high surface area, a moderate volume of mesopores, and abundant micropores and a high electrical conductivity that should promote its performance for the CO_2RR. CO_2RR results shown that F-CPC present a superior electrocatalytic behavior regarding others F-doped carbon materials. F-CPC exhibits the highest FE of 88.3% for CO at −1.0 V vs. RHE with a current density of 37.5 $mA{\cdot}cm^{-2}$ whereas all other control samples show lower FE for CO and lower current density (Figure 13h,i) suggesting that the cage-like porous structure greatly promote the activity for CO_2RR. The cage-like structure effectively promoted the reactant and products diffusion kinetics during the electrochemical process due to the existence of appropriate mesopores/micropores structure. Thus, the generation of a pore-engineering structure at the carbon shell results in highly efficient catalyst for CO_2RR.

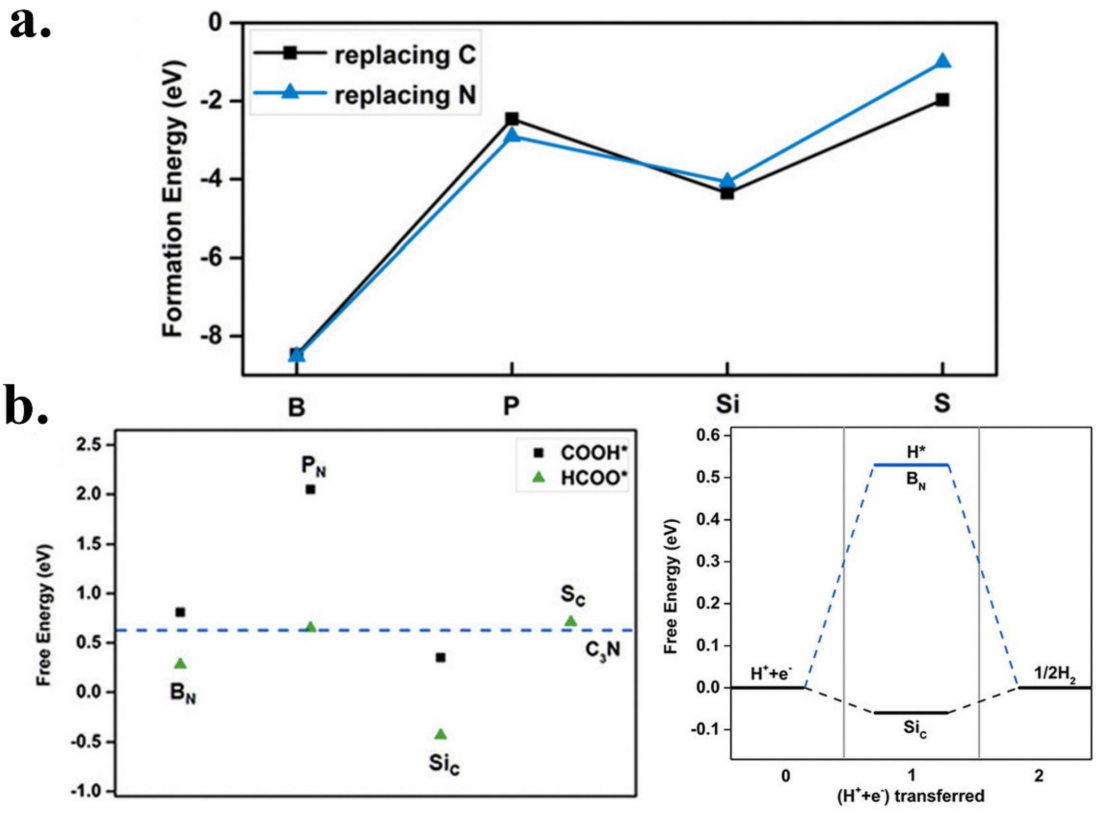

Figure 12. (**a**) Relationship between the formation energy of heteroatom-doped C_3N replacing N or C and type of doped atom, (**b**) free energies of COOH* and HCOO* adsorbed on heteroatom-doped C_3N (left) and Energy diagram of HER on B_N and Si_C-doped C_3N (right). Adapted from [89].

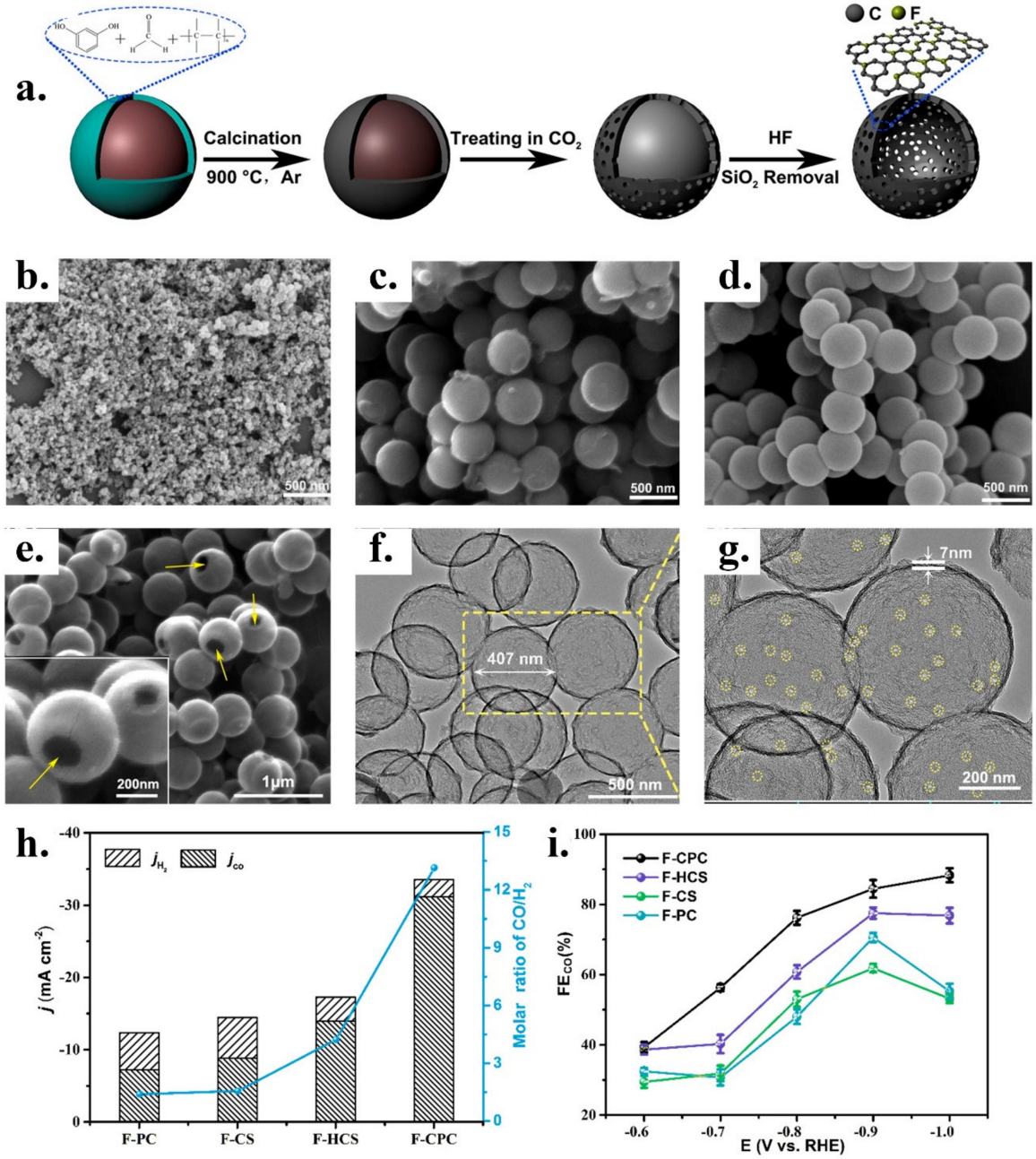

Figure 13. (**a**) Scheme of the synthesis of F-doped cage-like porous carbon (F-CPC), SEM images of F-doped (**b**) black pearls: F-PC, (**c**) carbon spheres: F-CS, (**d**) hollow carbon spheres: F-HCS and (**e**) cage-like porous carbon: F-CPC. (**f**-**g**) TEM images of F-CPC. (**h**) Geometrical current densities and the corresponding proportions of CO and H_2 at −1.0 V vs. RHE on F-doped carbon catalysts and (**i**) FE for CO production at different applied potentials. Adapted from [87].

Phosphorus and silicon have also been proposed as efficient heteroatoms to enhance the electroactivity for CO_2RR of carbon-based materials. Lui and co-workers [88] synthesized onion-like carbon (OLC), which was doped with P atoms through two post-doping processes: Impregnation (P-OLC-IP) and CVD (P-OLC-IP). The P doping method affects the configurations of phosphorus bonds. XPS, DRIFTS, and TPD shows that the P-OLC-CVD sample contains both P-C and P-O bonds in the same proportion, while the P-OLC-IP sample only contains P-O bonds. This different bond configurations influences the evaluation of the electrochemical performance in CO_2 reduction to CO. Onion-like carbon doped by CVD (P-OLC-CVD) has a better performance, registering a high FE to produce CO of 81% (at −0.9 V vs. RHE), a more positive onset potential (−0.65V vs. RHE), a

good stability of 27 h at −0.9 V, and a current density of 4.9 mA cm^{-2}. This improved catalytic performance of the P-doped carbon obtained by CVD comparted to the obtained by impregnation is explained based on the different bond configuration. The present of P-C bonds reduces the energy barrier of the rate-limiting step, that is, the proton–electron pair transfer from the catalyst surface to the CO_2 molecule to form the key intermediate COOH*. DFT calculations demonstrate that the *COOH adsorption energy is higher in P–C bonding than in P–O stabilizing the COOH* intermediate, therefore promoting the CO_2RR. Moreover, ultraviolet photoelectron spectroscopy (UPS) and partial density of state (PDOS) show that P–C bonding also improves the electron transfer capability regarding their P-O counterpart. Therefore, this work demonstrates that P-C bonding acts as active site for CO_2RR.

The feasibility of using Si atoms as doping heteroatoms of graphene to be used as metal-free electrocatalysts in CO_2RR was studied by Mao and co-workers [90] through computational methods. First, it is considered that CO_2 reduction catalytic mechanism on Si doped graphene edges originates from the coexistence of vacant and occupied sp^3 orbitals of Si atoms. Vacant sp^3 orbitals can accept electrons from the HOMO of CO_2 molecule, whereas the filled sp^3 orbitals can donate electrons to the CO_2 LUMO, which means that CO_2 can be captured and activated on Si doped graphene edges because, during this process, the energy density of C=O double bonds can be reduced, and the bond length elongated. Therefore, silicon atoms can be interesting heteroatoms to intervene in the CO_2 reduction process. When doping graphene, Si atoms are located at the edges of the material as single atoms or silicon chains in different configurations (Figure 14): Armchair silicon chain (Si chain@ACG), zigzag silicon chair (Si chain@ZZG), armchair single silicon (Si@ACG), and zigzag single silicon (Si@ZZG), each with different binding energies −1.15 eV, −1.29 eV, −0.83 eV and −0.65 eV, respectively. The computational calculations indicate that the configurations with Si single-atoms doped on the graphene edges have only one active site to bind the CO_2 molecule, obtaining C1-type products such as CH_3OH, however products such as CO and HCOOH do not have high selectivity because they have a strong interaction on active sites that makes its desorption difficult. On the other hand, Si chain doped graphene edges provide multiple active sites to interact with the CO_2 molecule, allowing the reduction of CO_2 to multi-carbon products especially C_2H_5OH.

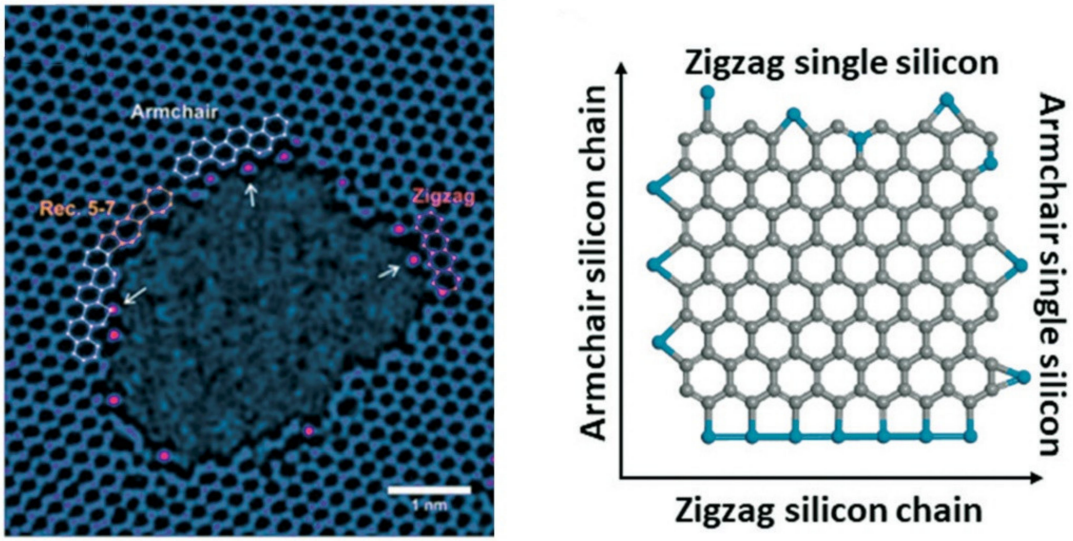

(**a**) (**b**)

Figure 14. (**a**) TEM image of a hole in graphene with single Si atoms attached to the edge (white arrows), and (**b**) different binding sites of Si at graphene edges. Adapted from [90].

However, despite good achievements have been made in CO_2RR by using heteroatoms doped carbon materials, the electrocatalytic activity and current density is still much poorer than that of metal-based catalyst and higher overpotential are required. Therefore, new strategies are still required to obtain a catalytic performance with practical meaning.

2.3. Dual-Doped Carbon-Based Materials

A recent strategy to further promote the electrocatalytic performance for CO_2RR is introducing multiple heteroatoms on the carbon network in order to obtain a synergistic effect between both heteroatoms. Wang and co-workers [91] synthesized N,S co-doped carbon nanosheets and analyzed its catalytic performance in comparison with their analog catalysts doped with a single heteroatom (S-doped and N-doped carbon). According to the XPS analysis, the co-doped catalyst has N-pyridinic species and S moieties (-C-S-C) that act as active sites and contributed to reactivity respectively, thus obtaining a superior electrochemical performance for the reduction of CO_2 to CO, whereas single doped materials (S-doped or N-doped carbon) mainly produced H_2 with a low selectivity to CO; a high FE for CO production of 85.4% (at −0.55 V vs. RHE) was obtained with N,S co-doped carbon nanosheets. This better performance is explained based on the 2D structure with abundant porosity originated by the co-doping. N precursor acts as both N source (urea) and pore-forming agent whereas the S precursor (Na_2SO_4) acts as template for forming 2D structures. This nanosheet 2D structured catalyst with abundant porosity allows a high exposure of the active sites (mainly pyridinic N) and therefore, more active sites for CO_2RR, together with better contact between the active sites and the electrolyte, which, all together, enhance the CO_2RR activity. A greatly enhanced catalytic CO_2RR activity and selectivity of N,S co-doped carbon catalyst regarding its S-free N-C counterpart was also observed by Pan and co-authors [92]. Their experimental and theoretical investigations (DFT) demonstrated that the incorporation of S into the N-doped carbon material causes more defects on the structure, providing more edge locations for N-doping and therefore facilitates the generation of high density of N-pyridinic species that serve as active sites for CO_2RR. Additionally, the introduction of S allows to reduce the free energy barriers for the formation of the intermediate COOH* on pyridinic and graphitic N, enhancing their intrinsic reactivity. The main product was CO since there is a weak adsorption of this product, which makes its desorption easy, then obtaining a faradic efficiency of 92% at −0.6 V vs. RHE with a low over-potential of 490 mV.

N and P co-doping has also been used to reorder the location and charge of neighboring carbon atoms in the material. Xie and co-workers [93] demonstrate that N and P co-doping co-activates neighbor carbon atoms facilitating the adsorption and the first transfer of electrons from CO_2 with lower energy, better key intermediates stabilization, and a rapid reaction kinetics. The carbon-based catalyst doped with N and P had a high faradic efficiency towards CO of 87% with a low overpotential of 340 mV. A synergetic effect between N and P dopants was also obtained by Chen and co-workers [94]. A high-performance N, P co-doped carbon catalyst was obtained, which shows a high FE for CO production of 92% (at −0.55 V vs. RHE). They found that the reactivity of nitrogen active centers (N-pyridinic and N-pyrrolic) is improved by the addition of P, since it reduces the formation energy barrier of the intermediate COOH* and the barrier of CO_2 activation which greatly enhance the reactivity.

Moreover, the obtaining of adjustable porous structures with high surface areas allows the easy transport of ions and provide minimal resistance. These properties together with the introduction of two different heteroatoms to material structure enables a timely improvement to develop catalysts with a good performance for CO_2 reduction. Ren and co-authors [95] developed a strategy to synthesize a porous carbon co-doped with nitrogen and boron with 3D hierarchical structure using a solution of NaCl-glucose, ammonia chlorine (NH_2Cl), and boric acid (H_3BO_3). First the solution was frozen in liquid nitrogen and then pyrolyzed in a two-stage heating process (Figure 15). This salt-sugar method provided more doping sites in the carbonaceous material. The result of using this electro-catalyst

in CO_2 reduction was obtaining a maximum faradic efficiency to CO of 83% at −0.4 V vs. RHE with a stability of 20 h. Additionally, the Tafel slope value equal to 64 mV dec^{-1} indicates the decrease of the reaction barrier for the first proton-coupled electron transfer process. The excellent performance was attributed to the synergistic effect between the N and B atom co-doping and the 3D hierarchical porous structure. The N pyridinic species is the one that shows the best capacity to facilitate the transfer of H* and the conversion of CO_2* to the intermediate COOH*. The introduction of the B atom can improve CO_2 capture and facilitate the transformation of COOH* to CO* due to its strong interaction with the O species [96]. The synergistic effect between B and N species on electrocatalytic activity was also studied by Lui and co-authors [96] with the N and B co-doping of nanodiamonds (BND). These BND allowed to obtain highly reduced products such as ethanol with a good electrochemical performance (FE = 93.2% at −1.0 V vs. RHE). These results are attributed to the important role played by N and B heteroatoms on nanodiamond-based catalysts; N-doping facilitates the transfer of H in reactions that involve hydrogenation and B-doping improves the CO_2 capture by means of union with an O atom.

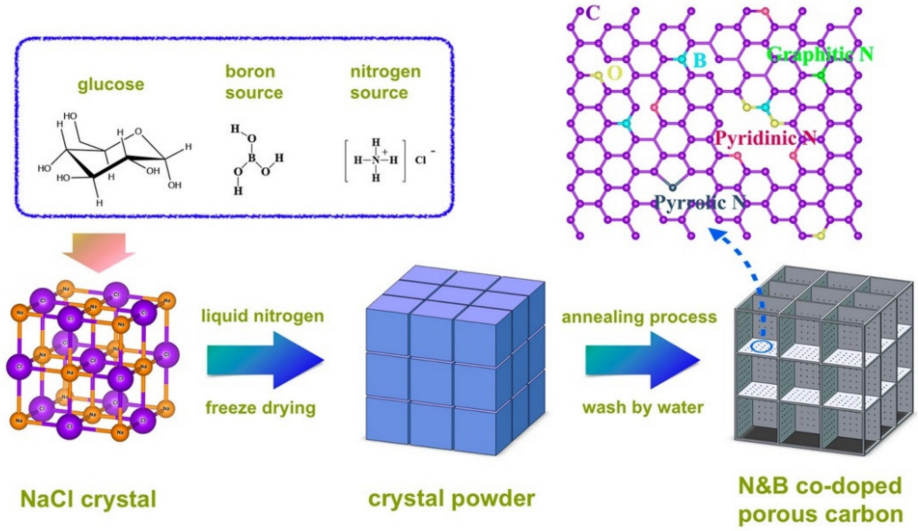

Figure 15. Schematic illustration of the synthesis of N and B co-doped porous carbon (NBPC) with a uniform 3D hierarchical structure. Adapted from [95].

In all recent co-doping processes (Table 5), it has been seen that two heteroatoms in the structure of the carbon-based material can increase faradic efficiencies, decrease overpotential, and improve catalyst stability. It is also shown how the synergistic effects of combining nitrogen with another heteroatom can facilitate the formation of the intermediate COOH* to produce CO. However, the principle of how dual doping works still remains to be clarified.

Much of the efforts for the synthesis of efficient catalysts have focused on the introduction of heteroatoms to carbon framework, N being the most widely used, however the use of heteroatoms such as B, F, and P have also had promising results that invite a deeper investigation into them, as well as the development of catalysts with two heteroatoms that demonstrated superior efficiencies in relation to the individual species (Table 6). In general, when metal-free electrocatalysts are studied, the electrochemical performance relies mainly on two factors: (I) The type of carbon material and its morphological properties such as porosity, which allows the accessibility of reagents to the active sites, and (II) the location, load, and type of heteroatoms or their functionalities in the carbon matrix. The balanced adjustment of these factors allows the improvement in the electrocatalytic activity, the catalyst selectivity, as well as its stability.

Table 5. Carbon and other precursors of heteroatoms to construction of electrocatalysts and active sites.

Sample	Main Product	Heteroatoms	Carbon Precursor	Heteroatom Precursor	Synthesis Method	Active Site	Ref
NS-CNSs	CO	N, S	Iron oleate	N (urea), S (Na_2SO_4)	Pyrolysis	N-pyridinic	[91]
NS-C	CO	N, S	Citric acid	N, S (Thiourea)	Pyrolysis	N-pyridinic	[92]
NPC	CO	N, P	Glucose anhydrous	N(urea), P(phytic acid)	Pyrolysis	P-N-C-	[93]
NPCM	CO	N, P	Aniline monomer	N (Aniline monomer), P (Phytic acid)	Pyrolysis	N-pyridinic N-Pyrrolic	[94]
NBPC	CO	N, B	Glucose	N (ammonia chloride NH_4Cl), B (boric acid H_3BO_3)	nitrogen-assisted freeze/Pyrolysis	N-pyridinic	[95]
BND	Ethanol	B, N	CH_4	B_2H_6/N_2	Chemical vapor deposition	n.d.	[96]

Table 6. Carbon-based materials metal-free doped with heteroatoms as electrocatalysts.

Electrode	Hetero-Atom	Sample	Electrolyte	Product	FE %	J [mA/cm^2]	Potential Cathode	Onset Potential/Overpotential	Stability vs. (RHE)	Tafel Slope [mV/dec]	Ref
1D/2D N-doped carbon nanorod arrays/ultrathin carbon nanosheets	N	NR/CS-900	0.5 M $KHCO_3$	CO	94.2	3.78	−0.45 V vs. RHE	−0.207 V vs. RHE/97 mV	30 h at −0.45 V	65	[31]
Metal-free N-doped graphene	N	N-graphene	0.5 M $KHCO_3$	Formate	73	7.50	−0.84 V vs. RHE	−0.3 V vs. RHE/0.78 V	12 h at −0.84 V	135	[40]
N-doped carbon nanotubes	N	PEI-NCNT	0.1 M $KHCO_3$	Formate	85	7.20	−1.85 V vs. SCE	−1.2 V vs. SCE	24 h at −1.8 V	134	[41]
N-doped carbon nanotubes	N	NCNTs	0.1 M $KHCO_3$	CO	80	~1.0	−0.78 V vs. SHE	−0.70 V vs. SHE/0.18V	10 h at −0.8 V	203	[32]
2D N-doped porous carbon nanosheets (coal tar pitch)	N	WNCNs-1000	0.1 M $KHCO_3$	CO	84	1.15	−0.6 V vs. RHE	−0.3 V vs. RHE/0.19 V	8 h at −0.6 V	132	[33]
Metal-free N functionalized graphene oxide	N	GO-VB6-4	0.1 M $KHCO_3$	Ethanol/Acetone	36.4/8.9	0.75	−0.4 V vs. RHE	n.d.	n.d.	n.d.	[48]
N-doped carbon nanotubes (NCNTs)	N	NCNTs-ACN-850	0.1 M $KHCO_3$	CO	80	~ 4.2	−1.05 V	−0.7 V/0.18 V	n.d.	160	[21]
N-doped multiwalled carbon nanotubes (MWCNTs)	N	CN/MWCNT	1 M KCl	CO	98	70	−1.46 V vs. Ag/AgCl	~−1.3 V vs. Ag/AgCl	n.d.	n.d.	[34]
NCNT	N	NCNT-3-700	0.5 M $KHCO_3$	CO	90	~5.0	−0.90 V vs. RHE	−0.40 V vs. RHE	60h at 0.90 V	~144.5	[35]
N-doped carbon	N	CNPC-1100	0.1 M $KHCO_3$	CO	92	~0.3	−0.6 V vs. RHE	−0.4 V vs. RHE	8 h at −0.6 V	~163	[36]
Carbon foam	N	CF -120	0.1 M $KHCO_3$	Syngas	~60 CO35 H_2	~10	−0.6 V vs. RHE	−0.3 V vs. RHE/0.19V	8 h at −0.6 V	103	[44]
Graphene foam	N	NG-800	0.1 M $KHCO_3$	CO	~85	~1.8	−0.58 V vs. RHE	−0.30 V vs. RHE/0.19V	5 h at −0.58 V	222	[37]
Mesoporous carbon	N	MNC-D	0.1 M $KHCO_3$	CO	92	6.8	−0.58 V vs. RHE	−0.28 V vs. RHE	16 h at −0.58 V	138	[38]
Microporous carbon	N	NPC-900	0.5 M $KHCO_3$	CO	95	2.3	−0.67 V vs. RHE	−0.27 V vs. RHE	10 h at −0.67 V	198	[27]
Hierarchically wood carbon	N	N-CWM	0.1 M $KHCO_3$	CO	78	~1.6	−0.68 V vs. RHE	−0.43 V vs. RHE	10 h at −0.68 V	144	[39]
3D integrated N-CNTs on SS	N	N-CNTs/SS	0.1 M $KHCO_3$	Syngas	~75% CO ~25 H_2	~1	−1.1 V vs. RHE	−0.2 V vs. RHE/90mV	8 h at −1.1 V	160	[45]
Plasma-treated CNTA (N-Doped Carbon Nanotube Arrays)	N	pCNTA10	0.5M $NaHCO_3$	Syngas	~75% CO ~25 H_2	n.d.	−0.82 V vs. RHE	−0.4 V vs. RHE/0.29V	10 h at −0.82 V	n.d.	[24]
N-doped carbon membrane/CNT carbon nanotubes	N	HNDCM/CNT	0.1M $KHCO_3$	HCOO	81	~11	−0.8 V vs. RHE	−0.18 V vs. RHE	36 h	138	[42]
PC61BM- N-C61	N	N-C61-800	0.5M $KHCO_3$	HCOO	91.2	11.6	−0.9 V vs. RHE	−0.42 V vs. RHE	12 h at −0.9 V vs. RHE	146	[43]
N-doped Meso-porous material	N	c-CN	0.1M $KHCO_3$	Ethanol	77	n.d.	−0.56 V vs. RHE	n.d.	6–24 h at −0.56 V vs. RHE	n.d.	[46]
N-doped Micro/Meso-porous material	N	MNCs-5	0.1M $KHCO_3$	Ethanol	78	n.d.	−0.56 V vs. RHE	−0.4 V vs. RHE	24 h at −0.56 V vs. RHE	n.d.	[47]

Table 6. *Cont.*

Electrode	Hetero-Atom	Sample	Electrolyte	Product	FE %	J [mA/cm^2]	Potential Cathode	Onset Potential/Overpotential	Stability vs. (RHE)	Tafel Slope [mV/dec]	Ref
N-doped graphene	N	NGM-1/CP	[Bmim]BF_4	CH_4	90.1	3.26	−1.4 V vs. SHE	n.d.	n.d.	n.d.	[49]
B-doped graphene	B	BG	0.1M $KHCO_3$	HCOO	66	n.d.	−1.4 V vs. SCE	−1.4 V vs. SCE	n.d.	n.d.	[75]
Diamond doped with B	B	BDD	0.1M NH_3	Methanol	24.3	n.d.	−1.3 V vs. Ag/AgCl	n.d.	n.d.	n.d.	[79]
Diamond doped with B	B	BDD	0.1M MeOH	Formaldehyde	74	n.d.	−1.7 V vs. Ag/AgCl	n.d.	n.d.	n.d.	[78]
Diamond doped with B	B	BDD	0.5M KCl	HCOOH	94.7	2	~−2.3 V vs. Ag/AgCl	n.d.	24 h	-	[80]
Diamond doped with B	B	BDD	0.075M RbOH	HCOOH	71%	2	~−2.5 V vs. Ag/AgCl	n.d.	n.d.	n.d.	[81]
Diamond doped with B	B	BDD	0.5M RbBr	HCOOH	95%	2	n.d.	n.d.	n.d.	n.d.	[82]
Diamond doped with B	B	BDD-0.01%	0.5M KCl	HCOOH	75	2	~−2.3 V vs. Ag/AgCl	n.d.	n.d.	n.d.	[83]
Diamond doped with B	B	BDD	KClO4/KCl	CO/HCOOH	36/87	n.d.	−1.8 V vs. Ag/AgCl/−2.5 V vs. Ag/AgCl	n.d.	n.d.	n.d.	[84]
Diamond doped with B	B	BDD	0.5 M KCl	HCOOH	~80%	2	−2.2 V vs. Ag/AgCl	n.d.	n.d.	n.d.	[85]
Fluorine-doped Cage-like Carbon	F	F-CPC	n.d.	CO	83.3	37.5	−1.0 V vs. RHE	n.d.	12 at −0.9 V vs. RHE	130	[87]
Fluorine-doped BD-2000	F	FC	0.1 M $NaClO_4$	CO	89.6	~0.224	−0.62 V vs. RHE	n.d.	n.d.	81	[86]
P-doped Onion-like carbon	P	P-OLC-IP	0.5 $NaHCO_3$	CO	60	0.5	−1.0 V vs. RHE	−1.0 V vs. RHE	n.d.	n.d.	[88]
P-doped Onion-like carbon	P	P-OLC-CVD	0.5 $NaHCO_3$	CO	81	4.9	−0.9 V vs. RHE	−0.65 V vs. RHE	27 h at −0.9 V	131	[88]
N, S-doped Nanosheets	N,S	NS-CNSs	0.5M KHCO3	CO	85	5.36	−0.55 V vs. RHE	–	20 h at −0.55 V	260	[91]
N, S-doped carbon/carbon paper	N,S	NS-C-900	0.1M KHCO3	CO	92	2.63	−0.6 V vs. RHE	−0.4 V vs. RHE/290 mV	21 h at −0.6 V	94	[92]
N, P-doped carbon/carbon paper	N,P	NPC	0.1M KHCO3	CO	87	0.81	−0.45 V vs. RHE	−0.25 V vs. RHE/140 mV	20 h at −0.45 V	72	[93]
N, P-doped carbon/carbon paper	N,P	NPCM	0.5 M NaHCO3	CO	92	n.d.	−0.55 V vs. RHE	−0.38V vs. RHE/270mV	24 h at −0.55 V	122	[94]
N, B-doped 3D hierarchical porous carbon/glassy carbon plate	N,B	NBPC	0.5 M KHCO3	CO	83	n.d.	−0.4 V vs. RHE	n.d.	20 h at −0.4 V	n.d.	[95]
B,N-doped nanodiamond	B,N	BND3	0.1 M NaHCO3	Ethanol	93.2	n.d.	−1.0 V vs. RHE	−0.6 V vs. RHE	3 h at −1.0 V	n.d.	[96]

3. Single-Atom Metal-Doped Carbon Catalysts

The individual metal atoms (single atoms) anchored on supports are another type of catalyst used in the electroreduction of CO_2. These catalysts are interesting because they allow heterogenization, which is the combination of the best properties of a homogeneous catalyst such as higher catalytic activity and selectivity, together with the best proprieties of a heterogeneous catalysts such as stability and easy separation [97].

When metal particles are reduced to an atomic scale, isolated atoms can be exploited to the maximum and are more catalytically active than nanoparticles, since the activity increases per metal atom. In addition, single atoms have a low coordination that can serve as catalytic active centers, and on the other hand, the homogeneity of their active sites could allow a high selectivity towards a certain product [98,99]. However, it is noted that by reducing the size of the particles to individual atoms, it also leads to a significant increase in surface free energy, causing an aggregation of these to larger particles in the synthesis process, therefore it is important to use suitable supports in which they can be distributed, anchored, and stabilized [98,100] (Figure 16).

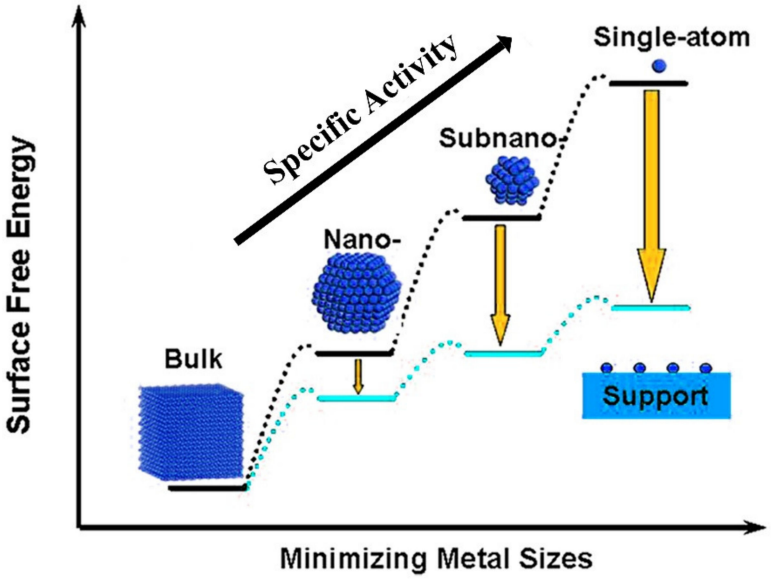

Figure 16. Scheme of metal particles reduced to an atomic scale and increase in free surface energy Adapted form [98].

3.1. Single-Atoms Supported on N-Doped Carbon-Based Materials (SMAs-N-C)

Carbon-based materials open the possibility of being used as supports due to their electrical conductivity and large specific surface areas that allow a high charge density of single atoms [97,101]. They also offer the possibility of being doped with nitrogen, allowing the metal atoms to be easily dispersed and stabilized through the strong interaction between them by means of the M-Nx bond (M = metal atoms) [102]. This makes carbon-based materials inexpensive and convenient supports for supporting isolated atoms.

3.1.1. SMAs-N-Graphene

One of the most widely used types of carbon-based materials is graphene because they have a well-defined 2D structure, they are highly conductive, and their chemical surface can be adjusted. The synthesis method to deposit single atoms on graphene consists of two main steps, *impregnation and reduction*. In the first step, the precursor for the carbon matrix can be impregnated at the same time with the nitrogen and metal precursors in solution (Co-deposition) [103] or only with the metal precursor, later the reduction process is carried out by means of a heat treatment in which active sites are formed by the bonds that form nitrogen and single atoms [104]. Graphene oxide (GO) nanosheets have been used as a precursor to the graphene matrix, mainly because it is negatively charged by the oxygenated

functional groups on its surface and edges, which allows metal cations in aqueous solutions to be adsorbed through electrostatic interactions during impregnation [105].

Several authors using this methodology managed to obtain catalysts in which monatomic metal sites predominated, homogeneously distributed with a high selectivity towards the reduction of CO_2 instead of the hydrogen production reaction and a significant improvement in the electrocatalytic performance compared to the larger particles of the same metal. For example, Jiang and co-workers [106], with single Ni atoms immobilized on graphene sheets doped with an NH_3 flux during heat treatment at 750 °C, reached a maximum faradic efficiency towards CO of ~95% under an overpotential of 620 mV and suppressed the competitive HER reaction by 10% in contrast to supported nanoparticle nickel catalysts [106]. According to the characterization by X-ray near-edge absorption structure (XANES) and X-ray absorption fine structure (EXAFS), the coordination environment of single atoms is a mixture of Ni atoms bound with nitrogen (Ni-N) and Ni atoms bound with carbon (Ni-C), however the incorporation of nitrogen mostly makes it easier to isolate the Ni atoms with the formation of the Ni-N bond. Furthermore, theoretical studies indicate that these active sites have a weak binding force with CO, which facilitates its desorption and also has a high energy barrier for hydrogen production. Zhang and co-workers [107] also used an NH_3 flux to dope the graphene matrix during heat treatment in a temperature range between 650–800 °C, however, the immobilized single atoms were Fe. Using different annealing temperatures allowed to determine the effect that temperature has on catalytic activity and the structural change of the active sites, finding that at a temperature of 800 °C a aggregation of Fe atoms to nanoparticles with diameters of 20 nm occurs and few catalytic sites are produced with an Fe-N coordination, therefore it showed a lower electrochemical performance compared to the Fe/NG-750 catalyst (annealing temperature 750 °C), with an FE towards CO over 80% at −0.60V vs. RHE. Moreover, the obtaining of CH_4 was identified with an FE less than 5% at potentials more negative than −0.30 V. By means of High-Angle Annular Dark-Field Scanning Transmission Electron Microscopy (HAADF-STEM), it was confirmed that the presence of nitrogen atoms in the sample (Fe/NG-750) allowed to immobilize the Fe atoms, achieving a predominant existence of monatomic Fe sites. Furthermore, XAFS (EXAFS) and XANES showed that electrocatalytic performance is derived mainly from the formation of coordinated Fe-N_4 sites.

Within the synthesis of SMAs-N-graphene, different ligands have also been used, whose structures with nitrogen atoms exhibit strong interactions with the graphene oxide sheets, while they can also join with the metal atoms forming the M-N bonds, achieving stabilization single atoms during heat treatment. Jiang and co-workers [101] used tris (2-benzimidazolylmethyl) amine (NTB) as ligand, together with nickel metal ions to synthesize a Ni complex (NTB) that was deposited on a GO solution. The Ni complex (NTB) was a simultaneous precursor of nitrogen and nickel atoms, then this complex adsorbed on GO is taken to a heat treatment (800 °C) in which the graphene oxide is reduced (rGO), it is doped with nitrogen and Ni metals are also deposited, forming coordinated Ni-N_4 sites (Figure 17a) that according to theoretical calculations allow to have a better selectivity towards CO since they present a high energy barrier to produce H_2. The experimental results showed a higher electrochemical performance (Fe (CO_2) = 97% at −0.8 V vs. RHE) for these catalysts, compared with catalysts without rGO as a support, demonstrating their ability to facilitate a homogeneous dispersion and stabilize the single atoms, preventing their aggregation to larger particles that can be passivated by the carbon layers. Ren and co-workers [108] immobilized cobalt phthalocyanine (CoPc) on graphene, the main reason for using CoPc was because the ease of accurately tuning its electronic structure when introducing functional ligands, in addition to having a well-defined structure and stability in CO_2 electroreduction. These characteristics allowed to investigate the behavior of electrochemical performance regarding the active site structure. A catalyst without any type of ligand (CoPc/G) exhibited a lower electrochemical performance compared to the catalyst with a nitro-type ligand (nitro-CoPc/G) that reached a faradic efficiency of 85.4% at −0.83 V vs. RHE and improving the density current by approximately 7%. The

improvement in the activity of the catalyst was attributed to the fact that the ligand (nitro) next to the catalytic center of the Co single atom raises the energy level of the orbital Co d_{z2} allowing efficient electron transfer from active sites to CO_2 and eventually decreases the Gibbs free energy of the rate-determining step, that is the formation of the intermediate CO_2^{*-}. Cheng and co-workers [109] impregnated microwave exfoliated graphene oxide (MEGO) with a nickel nitrate ethanolic solution and, once dried at 80 °C, the resulting material was processed by mixing and grinding urea as a ligand and another nitrogen precursor and subsequently heat pretreated at 800 °C under an atmosphere of NH_3. The structural characterization determined that in the wide pores greater than 50 nm, there is a higher concentration of Ni^{+2} adsorbed in the MEGO. In this case, there is a preference to form Ni nanoparticles. While Ni^{+2} encapsulated in pores of size smaller than 6 nm, it leads to the preferential formation of single atoms at the edge of the pores, because these mostly have N dopants, facilitating contact between the metal precursor and nitrogen resources such as NH_3 and urea in the heat treatment, leading then to a coordinated environment of Ni atoms with nitrogen species at the edges of the material with a high charge of single Ni atoms (6.3%) well distributed on MEGO. Due to the above characteristics, the electrochemical performance was superior with a maximum FE towards CO of 92.1% at a low over potential of 0.56V and a current density (Jco) of 26 mA cm^{-2} compared to other catalysts used such as a nickel foil (Ni^0) and nickel phthalocyanine (NiPc) with $FE_{(CO)}$ between 40–71%. On the other hand, Zhang and co-workers [110] used melanin structures to dope the graphene material, obtaining FeN_5-type sites atomically dispersed on the matrix. The synthesis process consisted of the simultaneous doping of melanin and Hemin (ferric chloride hemin) as a resource of iron (Fe^{3+}) and a pyrolysis process at 800 °C. During this process, the doped nitrogen forms an additional axial ligand coordinated with FeN_4 to form a new catalytic site of FeN_5 anchored in graphene (Figure 17b). The function of melanin not only facilitates doping with nitrogen atoms, but also allows iron atoms to be linked to a coordinated environment on graphene due to a great abundance of pyridinic and pyrrolic N species that allow the formation of the pentacoordinated iron (FeN_5) that improves the electrochemical performance for the reduction of CO_2 to CO with a faradic efficiency of 97% and a stability of 24 h at −0.46V vs,. RHE. According to the aforementioned research, a superior performance of FeN_5 sites over FeN_4 sites was found in reducing CO_2 to CO. Following the reaction mechanism shown in Figure 18 and the theoretical free energy calculations carried out by the authors [110], it can be observed that the FeN_5 site has a relatively weak binding force with the intermediate *CO (0.54 eV), which facilitates desorption of CO from the active site and therefore has a higher selectivity towards CO compared to the FeN_4 site, which has a desorption energy of 1.35 eV.

Within the synthesis methodology used by previous authors in which high pyrolysis temperatures are used, coordinated environments such as M-Nx, M-C, or M-O and defects in the matrix were obtained that can be difficult to understand, and it is difficult to attribute the true participation of each one on the catalytic activity. However, it can be assumed that the good performance achieved with these catalysts is due to the synergistic effect of the active sites and nitrogen-coordinated environments. Recently, and Li and co-workers [111] studied the role specifically played by Fe atoms with valence states of +2 and +3. For this, the authors designed two catalysts using iron-conjugated phthalocyanine molecules (FePc) on graphene (FePc-G) and then $NaBH_4$ was added to obtain the other catalyst named FePc-Gr. The FePc-Gr sample display a higher catalytic activity, obtaining a FE greater than 90% between the potentials −0.5 V and −0.6 V vs. RHE with an overpotential of 123 mV. According to the specific deconvolution of the peaks of the XPS characterization, it was found that the ratio of Fe^{2+} to Fe^{3+} (Fe^{2+}/Fe^{3+}) is greater in the FePc-Gr (0.83) catalyst compared to the FePc-G (0.36) catalyst, indicating that after treatment with $NaBH_4$ the oxidation states can change and suggests that the catalytic activity is mainly due to the obtaining of more Fe^{2+} atoms on the surface. Furthermore, the theoretical DFT calculations show that the catalytic activity of Fe^{2+} Pc can be better than Fe^{3+} Pc, however it was also found that having the two valence states together can have higher catalytic activities than

the individual states. An important point of view that is suggested is to pay more attention to the synergistic effect of each component in the catalysts of single atoms such as the effect of the valence states of the metal, the effect of the atoms that make up coordinated environments such as nitrogen, oxygen, carbon. Yang and co-authors [112] developed Ni single atoms catalysts with low-valent state Ni(I) and with a high intrinsic activity in the reduction of CO_2 to CO. The achievement of obtaining simple Ni(I) atoms was attributed to the low electronegativity of the pyridinic species N and S, and this last heteroatom was added by the authors for the dipping of graphene catalysts in addition to nitrogen. The result was a good electrochemical performance with mean overpotentials of 0.61 V, excellent stability (100 h) at high current densities such as 22 mA cm^{-2}, and high faradic efficiency of 97% for CO. Tou and co-workers [113] investigated different local coordination environments and their effects on catalytic activity by experimenting with changes in the synthesis temperature. Single Fe atoms were uniformly anchored on N-doped graphene nanosheets. They found that with increasing carbonization temperature, the pyrrolic-N species are converted to graphitic-N species and the amount of coordination between the single Fe atoms and nitrogen atoms (Fe-N) decreases, which weakened the activity and faradic efficiency in electrochemical reduction of CO_2 to CO.

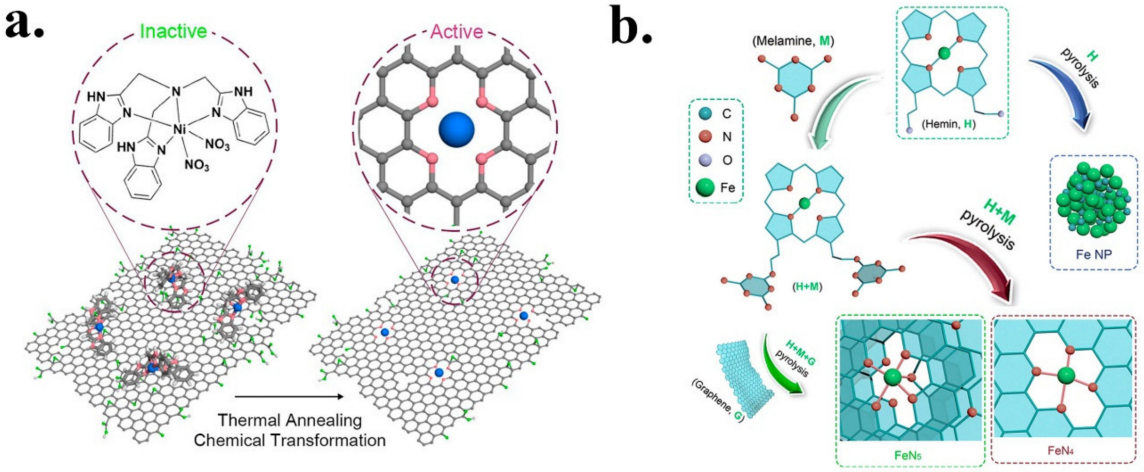

Figure 17. Synthesis methodologies for the immobilization of simple atoms using ligands. (**a**) Activation of adsorbed species on graphene oxide by thermal annealing (adapted from [101]) and (**b**) formation of the axial ligand coordinated with FeN_4 forming a new FeN_5 site (adapted from [110]).

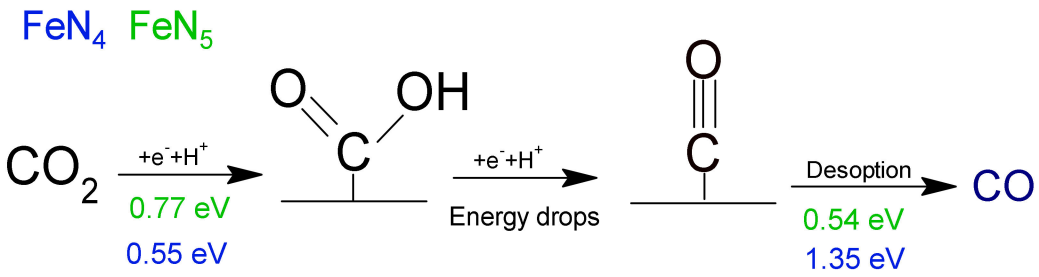

Figure 18. Reaction mechanism of the electroreduction of CO_2 to CO and binding force with intermediaries COOH*, CO* on FeN_4 and FeN_5 active sites.

In more theoretical studies developed mainly to understand the activity and selectivity of single atoms supported in graphene is the research carried out by Back and co-workers [114] that provides insights into understanding of transition metal activity (Co, Cu, Fe, Ir, Ni, Os, Pd, Pt, Rh, or Ru) as single atoms, finding that the different behaviors in these metals are due to their unique electronic structure and their electronic interaction between the d-orbital of metal atoms and the p-orbital of graphene. They also observed that

some of these materials are promising candidates for obtaining products such as CH_3OH and CH_4 using metals such as Ni, Pt, Os, Gr, and Ru, respectively. He and co-workers [115] using the computational hydrogen electrode model studied transition metals such as Ag, Cu, Pd, and Co. It is mentioned that in order for the single atoms to be well immobilized on the support, it is important to introduce defects in the material, defects that can bind strongly to the atoms and immobilize them; in this way, it is possible to avoid aggregations to large particles. Therefore, for the model, defects were introduced by removing C atoms and the vacant sites were replaced by single metal atoms. With this type of defect, it was observed that the efficiency and selectivity of the stabilized single metal atoms can be correlated according to their group number in the periodic table. They also found that at low overpotentials, products such as CH_4 can be obtained using Ag, Ni, Pd, Pt, and CH_3OH with Cu atoms.

3.1.2. SMAs-N-Other Carbon Materials

In general, the process of stabilizing single atoms in a carbon matrix consists of a process of pyrolysis of different precursors of carbon, nitrogen, and metal [116]. The ZIF zeolite imidazolate framework is an interesting precursor for the construction of carbon-based materials, because it has various nitrogen-containing ligands, has a porous structure, and has tunable metal nodes [117]. In addition, it has also been used by several authors as a matrix in the synthesis of single atoms catalysts applied to the electroreduction of CO_2 [116,118–124]. Zhao and co-workers [120] developed a synthesis strategy to obtain porous carbons doped with nitrogen, taking advantage of the fact that the Zn atoms of the ZIF-8 material evaporate in the pyrolysis process at an approximate temperature of 907 °C, leading to nitrogen rich defects and the sites left in the process can be occupied by neighboring Ni^{+2} ions. The catalysts showed abundant low coordinated sites on the surface and a strong bond with the intermediate CO_2^*, which was reflected in the electrocatalytic performance of the reduction of CO_2 to CO, with an FE equal to 71.9%, however the catalyst also exhibited an activity towards the competitive reaction HER. For their part, Zhang and co-workers [125] used layers of a two-dimensional bimetallic zeolite imidazolate framework (ZnNi-ZIF) as a precursor, which was subjected to a simple carbonization process obtaining layers of carbon doped with nitrogen and decorated with isolate Ni atoms (called SA-Ni @ NC). The advantages that the previous synthesis process brings are that the single Ni atoms can be maintained and immobilized through the Ni-N bond due to the process of etching with Zn atoms at high temperatures, which volatilizes much faster than Ni, in addition, ultra-thin 2D ZIF layers (~2.5 mm) are obtained that allow the Ni atoms to be completely exposed to the electrolyte. It is found that the Ni atoms are coordinated with three nitrogen atoms (Ni-N_3-C) and atomically dispersed on the carbon layers, and this result is complemented by the theoretical studies where it is observed that the active site Ni-N_3 presents a low barrier of 0.78 eV for the formation of the intermediate *COOH compared to Ni-N_4 sites, therefore the catalyst presented good electrocatalytic properties for the reduction of CO_2 to CO (FE = 86.2 and 10 h at −0.6 V vs. RHE). Wang et al. [126] used ZIF-8 as a precursor to obtain carbonaceous supports. Through the synthesis process, a gas diffusion strategy was used that consists of a one-step thermal activation in which the Fe sites are fixed on the nitrogen-doped nanoporous carbon. A polyhedral mesoporous matrix was obtained, and the distribution of its wide pores is mainly due to the gradual evaporation of the Zn species during the heat treatment. It was found that the coordinated sites with three nitrogen atoms of graphitic species (Fe-N_3) are the most active for the electrochemical reduction of CO_2 to CO, especially if they are located at the pore edges, allowing to reduce energy barriers for the formation of the intermediate COOH * and finally the production of CO. Therefore, excellent electrochemical performances were obtained, such as a faradic efficiency of 96% at 0.5 V vs. RHE and a current density of 6.8 mA/cm^2 at −0.6. Additionally, an exceptional stability of the catalyst was also obtained that maintained the FE and the stable current density for 48 h, so this catalyst was also used as a cathode to develop a Zn-CO_2 rechargeable battery.

ZnO@ZIF-NiZn core-shell nanorods synthesized by Hou and co-workers [127] served as a platform to obtain nitrogen-doped carbonaceous matrices with nanotube structures capable of anchoring single Ni atoms. First, the outer layer of ZnO nanorods was coated by a Ni-Zn bimetallic zeolitic imidazolate frameworks (ZIF-NiZn), which was formed from the reaction of Ni $^{2+}$, Zn^{2+} with 2-methylimidazole. Second, in a carbonization and acid treatment process, the ZnO core is removed as well as the Zn species, obtaining carbon nanotubes. The doping of single Ni atoms in the nanotubes is due to the fact that in the process the Ni^{2+} species replace the Zn^{2+} species that have been removed. Having nanotubes as a matrix facilitates mass diffusion and provides good conductivity, which was reflected in the high activity of the catalysts towards the reduction of CO_2 with an FE close to 100% in a wide potential of −0.6 V to −1.0 V vs. RHE, current density of 34.3% at −1.0 V, and stability of 20 h maintaining a percentage of 98% of its initial activity. Pan and co-workers [128] also obtained high electrochemical activity using commercial carbon nanotubes (C-CNT) in the synthesis of the catalysts. C-CNT were oxidized to obtain graphene nanoribbons attached to the outer walls of the remaining nanotubes, which had isolated Fe-N_4 active sites. In the synthesis, the use of an extra Fe precursor was not necessary, because commercial carbon nanotubes were obtained by chemical vapor deposition, so the Fe residues left by this synthesis technique were used for the formation of active sites. The hybrid material developed, facilitated mass transport, made the active sites accessible, thus achieving an $FE_{(CO)}$ of 96% and a partial current density of 22.6 mA/cm^2 at −0.76 V vs. RHE.

Through different synthesis methodologies, graphitic carbon nitride (g-N_3C_4) has been transformed as a raw material for obtaining carbonaceous matrices [129–133]. Li and co-workers [129] used topochemical transformation by carbon layer as a synthesis methodology, which allowed them to ensure the preservation in the structure of Ni-N_4 sites with a homogeneous distribution on the carbon sheets and avoided the agglomeration of Ni atoms to particles, thus allowing to obtain abundant active sites and, consequently, a maximum $FE_{(CO)}$ of 99% at −0.81 V, with a current density of 28.6 mA cm^{-2}. Zhao and co-workers [130] used a synthesis method called one-pot pyrolysis consisting of the transformation of the Ni-doped graphitic carbon nitride layered structure into carbon nanotubes in the form of bamboo with pyrolysis temperatures of 700–900 °C. The main achievement of this synthesis methodology is to generate abundant defects or trap sites in the material structure to stabilize the single atoms and have a significantly higher charge of these on carbon material (Ni atomic loading > 20.3%), which makes it suitable for practical applications. The use of these catalysts resulted in faradic efficiencies between 90.3 and 91.3% at −0.55 and 0.7 V vs. RHE, respectively. For this same line of research, the authors had already used the same synthesis methodology [131], unlike other metal such as Co, NiCo, CoFe, and NiPt were explored. The first three exhibited a good electrochemical activity from CO_2 to CO, however this was lower than the catalysts with single Ni atoms; conversely, the NiPt catalyst showed low activity for CO_2 reduction and high activity for HER. Lu and co-workers [132] synthesized N-doped ultrathin carbon nanosheets using g-C_3N_4 whose surface was coated with polydopamine (PDA), which contains nitrogen ligands for the coordination of different metal atoms within those Ni^{2+}. In this case, g-C_3N_4 was used as a template, so in the pyrolysis process, while the PDA was carbonized, the g-C_3N_4 template was decomposed and converted into a carbon skeleton doped with nitrogen. Furthermore, the Ni atoms were stabilized in a Ni-N_4 coordination environment. The main achievement of this synthesis methodology is that it allows controlling the content of Ni single atoms, obtaining an optimum metal content that is crucial for high electrochemical performances in CO_2 electrochemical reduction [132]. Ni and co-authors [133] investigated the influence of intrinsic defects in the carbon plane on catalytic activity, however intrinsic defects in the carbon plane are formed during the pyrolysis process together with other actives sites such as M-Nx and doped nitrogen species, making it a challenge to exclusively study their effect. To do this, they designed two catalysts with two different pyrolysis temperatures (800 °C and 900 °C), using carbon-rich graphitic carbon nitride (C-g-C_3N_4)

that served as template and carbon resource during the pyrolysis process. It is expected that the catalyst synthesized at the highest temperature will develop more intrinsic defects due to the release of unstable N atoms, which leads to a rearrangement of the C atoms, implying the formation of abundant intrinsic defects in the carbon plane. On the other hand, they obtained a catalyst poor in defects at the lower temperature, in addition, in both catalysts, they made sure to have the same distribution of active sites Fe-N_4. It was found that the intrinsic defects can also be active sites that together with the Fe-N_4 sites improve the electrochemical performance, therefore the catalyst rich in defects obtained a faradic efficiency towards CO of 90% at −0.75 V while the catalyst poor in defects obtained an FE 40% lower at the same potential.

On the other hand, Tou and co-workers [134] synthesized porous carbon nanosheets using $V_2O_5nH_2O$ as template. This material is a xerogel that contains stacks of sheets with parallel spaces and a weak interaction between layers that allows inserting active materials. In this case, meso-tetra(N-methyl-4-pyridyl) porphyrin ferric chloride(III) (FeTMPyP) was inserted and, subsequently, the template was removed by carbonization obtaining an ultrathin 2D carbonaceous material with Fe atoms coordinated with four nitrogen atoms that were the main active sites to reduce CO_2 to CO with an FE of 95.5% at −0.7 V. Precursors such as Hemin and polyaniline were used by Zhu and co-workers [116] to obtain carbon materials doped with nitrogen and Fe single metals. The Hemin precursor is chosen mainly because, in addition to containing the metal precursor Fe, it has carboxyl groups that are doped in the polyaniline chains through an electrostatic interaction, thus allowing a highly uniform dispersion of single atoms in the carbon structure, this is carried out by means of a heat treatment at a temperature of 700 °C. Within the chemical composition of the synthesized catalyst, it is found that during the treatment the majority of Fe^{3+} species are reduced to Fe^{2+} species, an atomic content of Fe equal to 0.86% was obtained, the single atoms are coordinated with Fe-N_4 sites, and the nitrogen species present were Pyridinic N > Pyrrolic N > Graphitic N > Oxidized N. According to theoretical studies, the graphitic N nitrogen species are the indicated species to accompany the Fe-N_4 active sites due to the fact that it presents a moderate binding force with the intermediates CHOO* and CO* in comparison with the other Pyridinic N and Pyrrolic N species. Wu and co-authors [135] also used polyaniline along with sea urchin-like FeOOH as an intermediate compound to obtain carbon nanorods with N atoms from using urea as a precursor. This carbonaceous matrix allows a high exposure of active Fe-Nx sites, for which a high FE of 95% and a low over potential of 530 mV were obtained. Using glucose and dicyadiamide as carbon and nitrogen precursors, respectively, carbonaceous matrices were obtained by He and co-workers [136], with the matrix managing to isolate single Pd atoms which, together with a coordinated environment of four nitrogen atoms, were the main active sites that allowed improving the desorption of the intermediate CO* and improving the catalytic activity without the need to use a large metal load. Glucose was also used as a carbon resource by Han and co-workers [137], who together with melanin and $Ni(NO_3)_2$ $6H_2O$ obtained carbon nanosheets with Ni-N_4 active sites. Additionally, within the synthesis process, polytetrafluoroethylene (PTFE) was used to promote the formation of single atom sites and induced the co-doping of fluorine heteronomous around the active sites that allowed to manipulate electronic structure and improve electrochemical performance. Like the previous authors, Chen and co-workers [138] also used the strategy of co-doping with Sn and N heteroatoms, and this allowed to improve the kinetic rate for the production of CO and therefore the catalytic activity. The development of double heteroatom doping catalysts to improve the stabilization of single atoms and the electrochemical performance is a promising new variant in the design of efficient electro-catalysts but that needs further study.

Recent research [139–141] highlights two important points to consider when designing single atoms catalysts, as they have been overlooked so far: (1) The first point is that in addition to taking into consideration the formation of catalytic sites, it is crucial to also study the structural geometry of the carbon matrix because it also plays a key role in the catalytic activity since the structure can influence the coordination environment of the

single atoms [118,142,143]. Hollow N-doped carbon spheres are a type of support in which individual atoms can be immobilized and their synthesis process allows good control in the design of the catalyst structure. For this, templates such as tetraethyl orthosilicate (TEOS) are used, which hydrolyze or condense leaving hollow pores [144]. Several authors [139,145–148] synthesized these materials to apply them in the CO_2 electroreduction to CO, however it was not until recently that Xiong and co-workers [139] studied the effect that different geometric structures have on carbon spheres that were used as supports for Ni-N_4 sites. The parameters studied were the shell thickness, compaction, and mesoporous size. For the synthesis of the carbon spheres, the polymerization method of a template such as TEOS and a carbon resource such as dopamine was used. Finally, they underwent pyrolysis at 800 °C. The way to fit different geometries to the matrix was by means of the dopamine variation concentration, Ni content in the dopamine solution, and the ratio of a solution containing NH_4OH, H_2O, and ethanol (Ni/HMCS-1-800, Ni/HMCS-2-800, Ni/HMCS-3-800). By means of this methodology, hollow mesoporous carbon spheres were obtained as supports, which have the main advantage of a high specific surface area and good permeability. However, within the synthesized samples, the Ni/HMCS-3-800 catalyst was optimal to obtain a good electrochemical performance ($FE_{(CO)}$ = 95% in a potential range between −0.7 to −1.1 V vs. RHE) that was related to the parameters studied in the support geometry determining two main points: (i) Having an ultra-thin carbon layer can help promote the CO_2 activation capacity of the catalyst, and allows obtaining a high content of pyridinic N species that reduce the energy barriers for CO_2 reduction by inhibiting HER and making the Ni-N_4 active sites are more exposed (Figure 19a), (ii) having mesoporous in a range of 7–10 nm was favorable to reduce the mass transfer resistance and capture the CO_2 molecules exhibiting the best catalytic ability (Figure 19b). Meanwhile, Ni and co-workers [142], in a theoretical study supported by density functional theory DFT, investigated the effect of the pore size of graphyne-based supports on the electrocatalytic activity of CO_2 using Cu single atoms. They found two important factors: (i) The pore size is directly related to the determination of the coordination number of single atoms; in other words, if the pores of the graphyne are small, they can accommodate just one Cu atom coordinated with three acetylene bonds. On the contrary, in larger pores, the Cu atoms are coordinated with two acetylene bonds. Furthermore, (ii) pore size also affects steric repulsion for reaction intermediates, therefore graphyne with large pores leads to small steric obstacles, resulting in strong binding of intermediates to active Cu sites, which in turn lowers energy barriers and lowers onset potential. In the case of small pores, the steric is stronger, leading to high overpotentials. Pan and co-workers [149] manipulated the pore edges on graphene to alter the electronic structure of the Fe-N_4 sites since they present a strong adsorption towards CO* intermediate, limiting the current density. The point of the research was to synthesize graphene with abundant holes in the basal plane using an etching with H_2O_2 in which the active sites Fe-N_4 were located mainly in the pores and their edges. For comparison purposes, a graphene was also synthesized without the generation of these holes, in which the active sites were located mainly in the bulk of graphene basal plane. Evidently in the experimental results, porous graphene obtained a superior performance with a TOF 3 times and current density 2 times larger than graphene without the development of porosity. In the calculations and theoretical studies, it was found that indeed the active Fe-N_4 sites located in the pores and edges (Fe-N_4-pore, Fe-N_4-edge) could decrease the overpotential and weaken the adsorption energy of CO, especially in the pore edges since the d-band center of Fe is reduced, increasing and decreasing the length and the Fe-C bond strength, respectively, which facilitates the desorption process. Fang and co-workers [150] developed catalysts with curved N-doped carbon nanofibers on which single Zn atoms were stabilized, from these catalysts they found that the effect of the materials curvature influences the improvement of the electrocatalytic activity from CO_2 to CO, because at an atomic level, the electron from the dx^2-y^2 orbital of the Zn atoms is released from the Zn-N bond to return to Zn atoms, which increases the electron density and accelerates the CO_2 electroreduction reaction. The current density obtained in a flow

cell was as high as 121.5 mA cm^{-2} with an FE of 94.7% at an overpotential of 330 mV and according to the DFT theoretical calculations, the active sites were Zn-N_4, which together with pyridine-N species decreased the energy barriers for the formation of *COOH. (2) The second point to consider is the economic and environmental impact on the production of single atom catalysts, therefore the use of abundant raw materials, low-cost, non-toxic, and processes that aim towards scalability and sustainability are proposed. For example, taking natural biomass as a raw material for the synthesis of carbonaceous supports is an option that can meet the sustainability objective. Wang and co-workers [140] used apples and natural egg whites as carbon and nitrogen precursors, respectively, and they also used $ZnCl_2$ as a Zn atom resource because it is relatively non-toxic. Passing through a pyrolysis process (900 °C), a catalyst with isolated Zn atoms supported on a hierarchically porous carbon matrix was obtained. The main coordination mode is the union of the Zn atoms with four nitrogen atoms Zn-N_4, the formation of the Zn-Zn bond was not observed, confirming that the zinc atoms were atomically dispersed on the support. The electrochemical performance is comparable to the catalysts with supports not derived from biomass, and the FE was 96% with an excellent stability of 20 h at −0.44 V vs. RHE. It also reports a much lower over potential equal to 50 mV. At the same time, Abbas and co-workers [141] used as a carbon and nitrogen precursor a molecule derived from biomass such as lignin and cellulose called adenine, which contains equal molar ratios of C and N. The adenine was taken together with the Ni precursor to a pyrolysis process varying the temperature among 800, 900 and 1000 °C to optimize the amount of nickel and nitrogen in the electrochemical performance. However, the sample synthesized at a temperature of 800 °C proved to be the optimal one with respect to its physicochemical and electrochemical properties, since it presented a high density of Ni-N_{4-x}-C_x type active sites located in the carbon support frameworks, which allowed obtaining a superior electrochemical performance with a high current density −300 mA/cm^2, an $FE_{(CO)}$ = 99.4% at a low over potential of 235 mV. It is considered that the previous results were obtained using a gas diffusion electrode (GDL) composed of a packed micro-porous layer of carbon (MPL) that allowed to reduce the mass transfer limitations in an electrochemical flow cell. To obtain the catalysts, Mou and co-workers [151] used a cost–effective and environmentally friendly synthesis process that consisted of immobilizing Ni single atoms on a sponge-template graphene oxide aerogel, by means of an impregnation on melamine sponge with a suspension of graphene oxide and $NiCl_2 \cdot 6H_2O$, followed by pyrolysis at 900 °C for one hour. The methodology resulted in a simple and rapid construction of catalysts with single atoms avoiding their aggregation, originating active Ni-N sites that allowed the reduction of CO_2 to CO with a faradic efficiency equal to 90.2% and an overpotential of 0.69 V vs. RHE. Ma and co-workers [152] were able to synthesize an inexpensive carbon matrix with easily available components such as melanin and citric acid, which after a pyrolysis process, obtain ultra-thin nano-sheets doped with single Ni atoms. Yang and co-workers [153] proposed a scalable strategy to obtain catalysts with single Cu atoms. The synthesis process is carried out by one-pot pyrolysis of chistosan that contains natural nitrogen, KOH that is used as activating agent to create porosity in the carbonaceous material, and Cu salt. The result was the obtaining of a carbonaceous matrix capable of immobilizing simple Cu atoms by coordinating these with four nitrogen atoms (Cu-N_4), obtaining a good electrochemical performance ($FE_{(CO)}$ = 92%, stability of 30 h at −0.7 V vs. RHE) and the design of a scalable synthesis strategy that uses nitrogen-rich biomass. Carbon black, along with urea, are also other cheap raw materials that have been used with easy and scalable synthesis process [154,155]. Yang and co-workers [155] obtained suitable matrices doped with nitrogen to anchor simple Zn atoms, and the synergistic effect between these and nitrogen atoms allows Zn-N_4 type coordination sites, in which the free energy barrier was considerably decreased for the formation of intermediate COOH*. For this reason, electrochemical performance was favorable to produce CO with faradic efficiency of 95% at −0.43 V vs. RHE and a low onset overpotential over 24 mV. On the other hand, Li and co-workers [156] also used carbon black transforming it together with $Ni(NH_3)_6I_2$ into nitrogen-doped carbon supports capable of anchoring Ni

single atoms, through impregnation and pyrolysis (900 °C) obtaining a FE(CO) = 92.3% with an overpotential equal to 0.69 V. He and co-workers [157] proposed an alternative synthesis strategy to avoid using high-temperature treatments, because this consumes a considerable amount of energy, reduces the nitrogen content of the material, and therefore causes aggregation of the simple atoms forming nanoparticles that are removed in most cases using acid treatments. This strategy consisted of chemical vapor deposition (CVD) using a low temperature of 450 °C, obtaining an open nanostructured material with a Ni metal core covered by a carbon layer doped with Ni-N sites. Electrochemical performance was remarkable with an FE of 87% and a current density of 14.8. mA cm^{-2}, results that are attributed to the characteristics provided by the nature of the catalyst, since the open nanostructure improves the mass transfer process, has isolated rich species of Ni-N that function as active centers, and the Ni metal core acts as conductor improving electron transport.

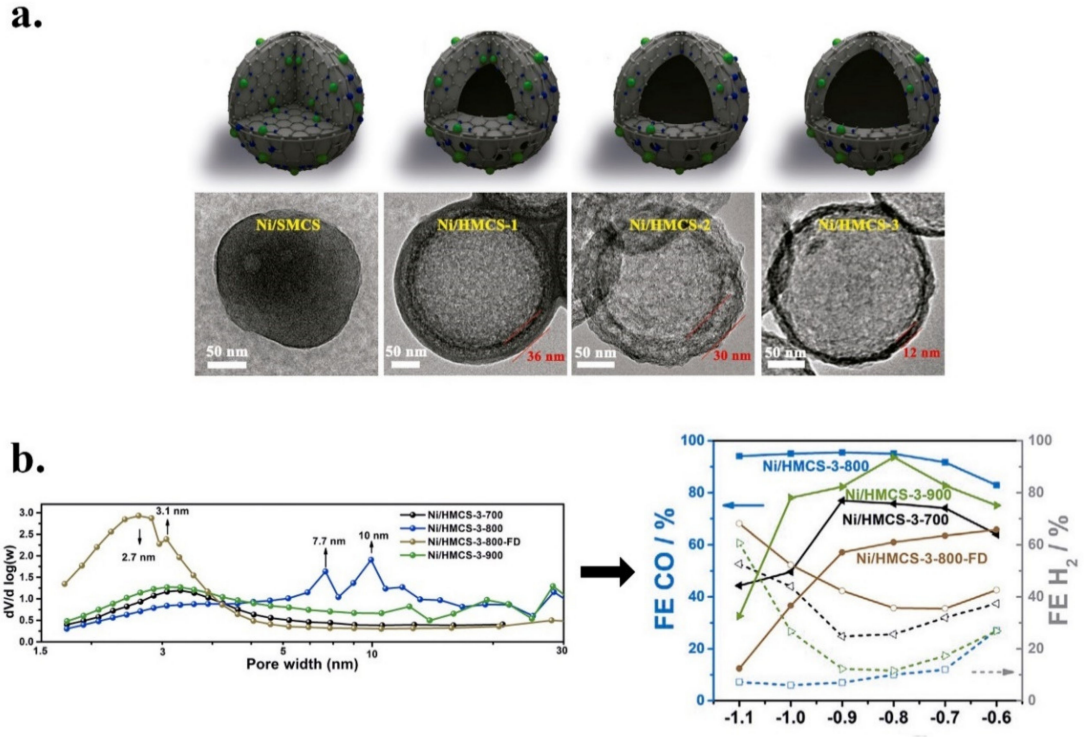

Figure 19. Relationship between geometric parameters (**a**) carbon shell (**b**) pore size on electrochemical performance. Adapted from [139].

To date, the investigations report CO as the main product of CO_2 reduction, and this is mainly due to the fact that, in single atom catalysts, the active sites formed in a coordinated environment show an ease in stabilizing the CHOO* intermediate and rapidly desorbing the CO product. Taking this advantage into account, the design of catalysts has also been considered with the aim of creating suitable active sites for both the CO reduction and the hydrogen evolution, allowing the production of syngas by manipulating the H_2/CO ratio. Song and co-workers [158] designed a catalyst with coordinated single Co atoms in the form of Co-C_2N_2 and nitrogen functionalities (N-pyridinic, N-graphitic), which form preferential actives sites for CO_2 adsorption and hydrogen evolution, respectively. To obtain these catalysts, the authors used an in-situ synthesis methodology based on the pyrolysis of ZnO@ ZIF, in which the excess Zn evaporated, preventing the aggregation of single Co atoms, and avoiding the loss of N during the process. In addition, a structure similar to that of a sponge was obtained, with a thin shell and a pore system with hierarchies, allowing a high exposure of active sites and facilitating the mass transport. In this way, the authors obtained an H_2/CO ratio of 1/2 in a potential range between −0.7 and −1.0 V. On the other hand, with the content of single atoms or the combination of these with nanoparticles of

metal, suitable active sites have also been obtained for both reactions. For example, He and co-workers [159] made two catalysts, one with single Ni atoms and the other with single Co atoms stabilized on a carbon doped with nitrogen, finding that the first catalyst had an exclusive activity towards the production of CO, while the second was selective towards hydrogen production. Considering the behavior of these catalysts separately, the authors proposed to develop a catalyst with a configuration of simple atoms using different ratios of Co/Ni atoms in order to be able to adjust the CO/H_2 ratio of the synthesis gas. In this case, they found that with an equal amount of CO and Ni, CO/H_2 ratios between 0.8 and 1.3 are obtained, which are suitable for the Fishcer–Tropsch thermochemical process. On the other hand, Zhu and co-workers [160] used single Ni atoms in the adjustment of the CO/H_2 ratio that are selective towards the reduction of CO_2 due to their active Ni-N sites and Ni nanoparticles (4.1 nm) that are selective to produce H_2. The variation of the quantity of nanoparticles with respect to the individual atoms is given by the etching treatment with HCl. A wide CO/H_2 ratio between 1:9 to 19:1 was obtained. Daiyan and co-workers [161] also adjusted the CO/H_2 ratio (1:2 to 1:1 to 3:2) by modulating active sites that consisted of nanoparticles of Co encapsulated in graphitic carbon shell on the one hand, to reduce CO_2 to CO, and on the other hand, the hydrogen evolution reaction is carried out by the remains of simple atoms of Co coordinated with four N atoms that decorate the material on the surface. Zhang and co-workers [162] synthesized a dual catalyst with single Ni atoms and single Fe atoms that were selective towards reducing CO_2 and HER, respectively. Adjusting the ratio between Ni and Fe it was possible to adjust the CO/H_2 ratio in a wide window of 0.14–10.86 to −0.86 V vs. RHE.

Although there are more studies on catalysts that have a great facility to rapidly desorb the CO product, there are single atom catalysts that have been able to have a relatively high bond energy with intermediate CO*, which stabilizes, then obtaining more reduced products. In this sense, Yang and co-workers [163] managed to obtain methanol with a $FE_{(methanol)}$ of 44% at −0.9 V vs. RHE. The methodology to obtain the catalysts consisted first of the adsorption of Cu ions in the pores of ZIF-8 obtaining nanoparticles Cu/ZIF-8, secondly, these nanoparticles were embedded in polyacrylonitrile (PAN) nanofibers, and finally they were carried out to a carbonization process in which nitrogen-doped nanofibers with a hollow interconnected structure are obtained and the coordination sites of the isolated Cu atoms with nitrogen are formed. The main characteristic of the synthesized catalysts is their flexibility and direct employability as a working electrode, so no type of binder is used that can minimize the exposure of active sites. In addition, their through-hole structure benefits the CO_2 diffusion and exposes the active sites on the surface, allowing to achieve a high current density of 93 mA cm^{-2} and a long stability of 50h at −0.9 V vs. RHE. Krapinar and co-workers [164] also used single Cu atoms that were immobilized in an amorphous carbon matrix synthesized from ZIF-8, to obtain ethanol. The optimal conditions for the electroreduction of CO_2 were a potential of −1.2 V, with a CO_2 flow of 2.5 mL min^{-1} and the use of 0.1M $CsHCO_3$ as electrolyte, resulting in a maximum $FE_{(ethanol)}$ of 43% and $FE_{(CO)}$ of 25%. Obtaining a low selectivity towards ethanol was attributed to a decrease in the local concentration of CO at electrode surface, caused by CO_2 bubbling. Therefore, to improve this situation, the authors decided to recycle the gas phase (CO), taking into account that these product serves as an intermediate to continue reducing to ethanol, thus improving $FE_{(ethanol)}$ up to 12%. Zhao and co-workers [165] detected liquid products mostly multi-carbon products such as acetic acid, ethanol, and acetone using a N-doped porous carbon synthesized from Cu-doped ZIF by a hydrothermal and carbonization processes. In general, all the products were obtained at a low overpotential, however acetone was the majority product (production rate 336.1 μg h^{-1}) with faradic efficiency of 36.7% at −0.36 V vs. RHE. In mechanistic studies, it was identified that, in all reaction steps, the free energy change was negative, which means that the reduction from CO_2 to acetone is thermodynamically favorable over the catalysts used; in addition, its high selectivity towards acetone is attributed to the fact that simple Cu atoms are

coordinated with four pyrrolic nitrogen atoms that can lower energy barriers to activate the CO_2 molecule.

Formate is another product that has recently been obtained by Shang and co-workers [166], who designed a catalyst with simple In atoms anchored on N-doped metal organic framework (MOFs). The main active sites were found to be single In atoms coordinated with four N atoms. According to the DFT theoretical studies, the formation of HCOO* was energetically more favorable than the formation of the intermediate COOH* for the obtaining CO. In addition, in the experimental results, the catalysts proved to have a high electrochemical performance with an FE (formate) of 96% at −0.65 V vs. RHE. Jiang and co-workers [167] constructed catalysts with single Sb atoms anchored in N-doped carbon nanosheets, which showed Sb-N_4 type active site that also led to a high FE of 94% at −0.8 V vs. RHE. Yang y co-workers [168] found that using single Bi atoms supported on carbon black, the reaction kinetics are accelerated and the process of reducing CO_2 to formate is facilitated. This was demonstrated through mechanistic studies, where the catalysts obtained a Tafel slope of 86 mV dec^{-1}, which means that electron transfer-proton coupling can be the rate-limiting step and shows a much lower slope than its analog catalysts formed by BiO_x cluster supported on carbon black (BiO_x/C), which obtained a Tafel slope of 118 mV dec^{-1}. The catalyst with single Bi atoms also showed superiority in the electrochemical performance with a maximum FE of 83.6% at −1.1 V vs. RHE, while the BiO_x/C catalyst obtained a maximum efficiency of 49.4% at the same potential. The selectivity of above-described catalysts towards the production of formate is mainly due to their ability to use the first pair of electrons for the reduction of CO_2 (adsorbed) towards the intermediate HCOO*, which is finally desorbed from the surface to be detected as formate.

The production of hydrocarbons such as CH_4 was also reported by Han and co-authors [169], who developed a catalyst with single Zn atoms anchored in a nitrogen-doped microporous matrix, which showed a FE of 85% and a current density of −31.8 mA cm^{-2}. The good electrochemical performance of the catalyst is attributed to its microporosity that favors the exposure of the active sites. Regarding its selectivity towards CH_4, it was found that the catalyst blocks the generation of CO because the O atoms prefer to form a chemical bond with the Zn atoms to obtain the intermediate *OCHO, instead of forming chemical bonds with the C atoms to obtain the intermediate *COOH that allows the formation of CO. Then from the intermediate *OCHO, in the following reaction steps, the O atom is rejoined with the single Zn atom and the protonation of the carbon is favored until reaching the * $OHCH_3$ intermedia; from this other H atom, it joins a C atom, thus releasing a CH_4 molecule and the * OH remains attached to the single Zn atom.

As a resume, for the development of efficient catalysts with single atoms, the following aspects stand out: (i) The coordination environment of the metallic sites in the single metals are influenced by the synthesis parameters described above, as well as the materials used as precursors of nitrogen, carbon, and the type of metal [170] (Table 7). (ii) The dominant pyridinic N species on graphene are known as efficient sites for metal coordination [106], so that single metal atoms could form mostly M-Nx bonds with these N species for their stabilization, however the influence on the electrochemical performance of the different nitrogen species in single atom catalysts still needs to be studied in greater depth. (iii) The coordination sites can be first shell, which are directly attached to the isolated atom that for N-doped materials, the first layer coordination site is nitrogen, however other atoms with a lower coordination force (second-higher Shell) but that could influence the electro-catalytic performance can be found, such as carbon and or oxygen atoms [102]; this also suggests a deeper approach. (iv) The possibility of adjusting and controlling the structures, defects, shapes, sizes, and components of carbon matrices can be explored to adjust the electronic structures of single atoms and consequently improve the electrocatalytic performance [171]. (v) Take into consideration economic and environmental aspects when selecting the precursors and the synthesis process.

Table 7. Synthesis of single atom catalysts and electrochemical performance.

Electrode	Electrolyte/Main Product	Precursor/Matrix	N Precursor	SMAs	MC [a] (wt. %)	M-N [b]	FE %	J_{CO} mA/cm^2	Potential Cathode	Onset Potential/η [mV]	Stability	Experimental	Ref
Ni-N_4-C/Glassy carbon	0.5 M $KHCO_3$/CO	g-C_3N_4/Carbon sheets	n.d.	Ni	n.d.	Ni-N_4	99.0	28.6	−0.8 V vs. RHE	n.d./~700	30 h at −0.81 V	Unvided cell/three-electrode system at an electrochemical station (CHI760E)	[129]
Ni SAs/N-C/carbon fiber paper	0.5 M $KHCO_3$/CO	ZIF-8/Porous carbon	n.d.	Ni	1.53	Ni-C/Ni-N_3	71.9	7.37 at −1.0 V	−0.9 V vs. RHE	−0.57 V vs. RHE/890	60 h at −1.0 V	Gas-tighttwo-compartment cell, Nafion 115 membrane	[120]
Ni- and N-doped reduced graphene oxide (Ni-N-rGO)/Carbon paper	0.5 M $KHCO_3$/CO	Graphene oxide (GO)-Graphene (Hummer´s method)	Tris (2benzimida-zolylmethyl) amine (NTB)	Ni	0.39	Ni-N_4/Ni-O	97.0	~25 at −0.8 V	−8 V vs. RHE	−0.60 V vs. RHE/490	n.d.	Two-compartment electrochemical cell (H-type),Nafion 117 membrane	[101]
Fe-N-doped graphene/Carbon fiber paper	0.1 M $KHCO_3$/CO	Graphene oxide (GO)-Graphene (Hummer´s method)	NH_3	Fe	0.52	Fe-N_4 (Pyridinic N)	~80.0	~1.75 at −0.6V	− 0.6 V vs. RHE	−0.30V vs. RHE/190	10 h at −0.60 V	One-compartment	[105]
Ni-NG/Glassy carbon	0.5 M $KHCO_3$ CO	Graphene oxide (GO)-Graphene	NH_3	Ni	0.44	Ni-N (Pyridinic N, Pyrrolic) Ni-C	~95.0	~11 at 0.73 V	−0.73 V vs. RHE	−0.31 V vs. RHE/~190	20 h at −0.75 V	H-Type glass cell, Nafion 117 membrane, Counter electrode of platinum foil, reference electrode SCE	[106]
Ni-NMEGO/Carbon paper	0.5 M $KHCO_3$/CO	Exfoliated graphene oxide (MEGO)	Urea/NH_3	Ni	~6.9	Ni-N edge (Pyridinic Graphitic N) Ni-C	92.1	26.8 at 0.7 V	−0.7 V vs. RHE	−0.29 V vs. RHE/180	21 h at −0.55 V	One-compartment, Counter electrode of Ir black carbon on carbon paper	[109]
A-Ni-NG/Glassy carbon	0.5 M $KHCO_3$/CO	Graphene/2D Graphene	Melamine (N)/L-Cysteine(S)	Ni	4.0	Ni(I)-N-C	97 at ~−0.7	31.5	−0.72V vs. RHE	~−0.35 V vs. RHE/n.d.	n.d.	H-type electrochemical cell, Nafion 117 membrane	[112]
A-Ni-NSG/Glassy carbon					2.5	Ni(I)-S-C	97 at ~−0.5V	36.5		~−0.18 V vs. RHE/n.d.			
NiSA-N-CNT/Carbon paper	0.5 M $KHCO_3$/CO	Dicyandiamide/ Bamboo-like CNTs (multiwalled)	Dicyandiamide	Ni	20.3	Ni-N_4	90.3–91.3	23.5 at −0.7 V	−0.55 V to −0.7 V vs. RHE	(0.275 V vs. RHE/165	n.d.	Unvided cell/three-electrode system	[130]
Co-HNC/Carbon fiber paper	0.1 M $KHCO_3$/Syngas	Zeolite imidazolate framework ZIF/3D hollow carbon structure	Zeolite imidazolate framework ZIF	Co	3.4	Co-C_2N_2	~100	n.d.	>−0.7V vs. RHE	n.d.	24 h at −0.8 V	Gas-tight full electrochemical cell (Typical threeelectrode configuration)	[158]

Table 7. *Cont.*

Electrode	Electrolyte/Main Product	Precursor/Matrix	N Precursor	SMAs	MC [a] (wt. %)	M-N [b]	FE %	J_{CO} mA/cm^2	Potential Cathode	Onset Potential/η [mV]	Stability	Experimental	Ref
ZnNx/C/Glassy carbon totating disk electrode	0.5 M $KHCO_3$/CO	Carbon black BP 2000/Micro and mesoporous carbon	Urea	Zn	0.1	Zn-N_4	95	4.8 at −0.43 V	−0.43 V vs. RHE	−0.13V vs. RHE/320	75 h at −0.43 V	Three-electrode system with a gas-tight twocompartments H-cell.	[155]
Co-N5/HNPCSs/carbon paper	0.2 M $NaHCO_3$/CO	Melamine/Hollow carbon spheres	Melamine	Co	3.5	Co-N_5	>90	~4.5 at −0.73 V	−0.57 V to −0.88 V vs. RHE	n.d.	10 h at −0.73 V	H-type cell, Nafion 117 membrane	[145]
H-M-G/Carbon paper	0.1 M $KHCO_3$/CO	Graphene	Melamine	Fe	1.4	Fe-N_5 (Pyridinic -Pyrrolic N)/Fe-N_4	97	~1.8 at −0.46 V	−0.46 V vs. RHE	−0.26 V vs. RHE/150	24 h at −0.46 V	Two-compartment electrochemical cell (H-type),Nafion 117 membrane	[110]
Ni-N/C-1/4/Carbon paper	0.5 M $KHCO_3$/CO	ZIF-8/Carbon nanotubes	ZIF-8	Ni	6.6	Ni-N	~ 80	~6.77 at −0.98 V	−0.78 V vs. RHE	n.d.	4.5 h at −0.78 V	H shaped electrochemical cellNafion 115 membrane	[146]
NiSA-NGA-900/Carbon cloth	0.5 M $KHCO_3$/CO	Melamine foam/Sponge templated graphene oxide aerogel	Melamine	Ni	~2.6	Ni-N	90.2	~8.0	−0.8 V vs. RHE	−0.4 V vs. RHE/690	6 h at −0.8 V	Gas tight H-cell, Nafion membrane N117	[151]
Ni/NC_950/Glassy carbon	0.1 M $KHCO_3$/CO	Carbon black/Micro-mesoporous carbon	$Ni(NH_3)_6I_2$	Ni	n.d.	Ni-N	90.7	~2.5	−0.8 V vs. RHE	−0.6V vs. RHE/690	10 h at −0.8 V	H-type cell, Nafion 117 membrane	[156]
Self-supported CuSAs/TCNFs	0.1 M $KHCO_3$/CH_3OH	ZIF-8/Through-hole carbon nanofibers	ZIF-8	Cu	1.3	Cu-N_4	44.0	93.0	−0.9 V vs. RHE	−0.41 V vs. RHE/n.d.	50 h at −0.9 V	Two-compartment electrochemical cell, Nafion 117	[163]
Fe-N-G-p/Carbon paper	0.1 M $KHCO_3$/CO	Graphene oxide(GO)-Graphene (Hummer´s method)	Urea	Fe	0.36	Fe^{+3}-N_4/Fe-O	94.0	4.5 at −0.58 V	−0.58 V vs. RHE	n.d./470	9 h at −0.58 V	Two-compartment electrochemical cell (H-type), Nafion 117 membrane	[149]
SA-NI@NC/Glassy carbon	0.1 M $KHCO_3$/CO	zeolite imidazolate framework ZIF/2D carbon layers	Zeolite imidazolate framework	Ni	~1.61	Ni^{+2}-N_3	86.2	n.d.	−0.6 V vs. RHE	−0.3 V vs. RHE/n.d.	1 0 h at −0.6 V	Two-compartment electrochemical cell (H-type), Nafion 115 membrane	[125]
Fe1NC/S1-1000/Carbon paper	0.5 M $KHCO_3$/CO	ZIF-8/Porous Carbon	ZIF-8	Fe	0.38	Fe-N_3 (graphitic N)	96.0	6.8 at −0.6 V	−0.5 V vs. RHE	−0.3 V vs. RHE/190	45 h at −0.45 V	Two-compartment electrochemical cell (H-type), Nafion 117 membrane,	[126]

Table 7. *Cont.*

Electrode	Electrolyte/Main Product	Precursor/Matrix	N Precursor	SMAs	MC [a] (wt. %)	M-N [b]	FE %	J_{CO} mA/cm^2	Potential Cathode	Onset Potential/η [mV]	Stability	Experimental	Ref
Fe-SA/NCS-700/Carbon paper	0.5 M $KHCO_3$/CO	Hemin/Carbon nanosheets	polyaniline	Fe	0.89	Fe-N_4 (graphitic N)	87.0	6.5 at −0.65 V	−0.47 V vs. RHE	−0.215 V vs. RHE/105	10 h at −0.47 V vs. RHE	Two-compartment electrochemical cell (H-type), Nafion 117 membrane	[116]
Ni/HMCS-3-800/Glassy carbon disk	0.5 M $KHCO_3$/CO	Dopamine/ Hollow mesoporous carbon spheres (HMCS)	n.d.	Ni	0.26	Ni-N_4-C (Pyridinic N, graphitic N)	95	10.5 at 1.1 V	−0.7 to −1.1 V vs. RHE	n.d.	10 h a −0.9 V vs. RHE	Two-compartment electrochemical cell (H-type), Nafion 117 membrane.	[139]
SA-Zn-NHPC/Carbon paper	0.5 M $KHCO_3$/CO	Apples/ Hierarchically porouscarbon	Egg whites	Zn	0.34	Zn-N_4	96	~ 5 at −0.44 V	−0.44 V vs. RHE	−0.16 V vs. RHE/50	20 h at −0.44 V vs. RHE	Two-compartment electrochemical cell (H-type), Nafion 115 membrane.	[140]
C800NiA/GDE composed of a packed carbon microporous layer (MPL).	1.0M KOH/CO	Adenine/Porous Carbon	Adenine	Ni	2.6	Ni-N_4-C	99	199 at −0.31 V	−0.31 V vs. RHE	n.d./235	6 h at 0.31 V vs. RHE	Flow cell, anion exchange membrane	[141]
CoNi-NC/Carbon paper	0.5 M $KHCO_3$/Syngas	Glucose/Carbon	Picyandiamide	Ni, Co	Ratio Co/Ni=1	Ni-N, Co-N (pyridinic N)	CO:53% CO/H_2 ratio: 0.8–1.3	51 at −0.9 V	−0.9 V vs. RHE	n.d.	7 h at 0.9 V vs. RHE	Two-compartment electrochemical cell (H-type), Nafion 117 membrane	[159]
Ni SAC/Carbon paper	0.5 M $KHCO_3$/Syngas	Dimethylglyoxime/ mesoporous carbon nanorods	dimethylglyoxime	Ni	n.d.	Ni-N	CO/H_2 ratio: 1:9 to 19:1	15 at −0.65 V	−0.65 V vs. RHE	n.d.	>8 h at 0.65 V	Two-compartment electrochemical cell (H-type), Nafion 115 membrane.	[160]
Cu SAs/NC/Carbon paper	0.1 M $KHCO_3$/CO	Chitosan/ Microporous carbon	Chitosan	Cu	0.32	Cu-N_5	92	8.9	−0.7 V vs. RHE	−0.23 V vs. RHE/n.d.	30 h at −0.7 V	Gastight two-compartment electrochemical cell, Nafion 212 membrane	[153]
NiSA/N-C/Carbon paper	0.5 M $KHCO_3$/CO	g-C_3N_4/ultrathin porous carbon nanosheets	Polydopamine (PDA)	Ni	0.86	Ni-N_4	96	26.4	−0.86 V vs. RHE	n.d./750	22 h at −0.86 V	H-type electrochemical cell, Nafion 117 membrane	[132]
SAs/NC/Carbon paper	0.5 M $KHCO_3$/Formate	ZIF-8/Porous Carbon	ZIF-8	In	1.25	In-N_4	96	8.87	−0.65 V vs. RHE	n.d.	60 h at −0.65 V	Gas-tight standard three-electrode H-type cell	[166]
DNG-SAFe/Carbon paper	0.1M $KHCO_3$/CO	C-g-C_3N_4/Graphene likeporous carbon	C-g-C_3N_4	Fe	0.74	Fe-N_4	90	33	−0.75 V vs. RHE	n.d.	17 h at −0.75 V	Gas-tight H-cell, Nafion 117 membrane	[133]

Table 7. *Cont.*

Electrode	Electrolyte/Main Product	Precursor/Matrix	N Precursor	SMAs	MC [a] (wt. %)	M-N [b]	FE %	J_{CO} mA/cm^2	Potential Cathode	Onset Potential/η [mV]	Stability	Experimental	Ref
Sb SA/NC/Glassy carbon	0.5M $KHCO_3$/Formate	Trimesic acid/ultrathin porous carbon nanosheets	Dicyandimide	Sb	2.86	Sb-N_4	94	~20	−0.8 V vs. RHE	n.d.	10 h at −0.8 V	Gas-tight H-cell,Nafion 117 membrane	[167]
Bi Sas/C/Carbon fiber paper	0.1M $KHCO_3$/Formate	Carbon black	n.d.	Bi	n.d.	n.d.	83.6	12	−1.1 V vs. RHE		10 h at −1.1 V	H-cell system, Nafion 115 membrane	[168]
Ni-NC@Ni/Carbon fiber paper	0.1M $KHCO_3$/CO	Urea/sheet-like open nanostructure	Urea	Ni	11.05	Ni-N	~87	14.8	−0.78 V vs. RHE	n.d./670	150 h at −0.78 V	Gas-tight H-cell, Nafion 117 membrane	[157]
SA-Zn/MNC/Carbon fiber cloth	0.1M $KHCO_3$/CO	Glucose/Microporous N-doped carbon	Hydroxyl ammonium chloride ($(NH_3OH)Cl$)	Zn	2.66	Zn-N_4	85	−31.8	−1.8 V vs. SCE	n.d.	35 h at −1.8 V	Two-compartment batch cell	[169]
ZnO@ZIF-NiZn50/Carbon fiber paper	0.5M $KHCO_3$/CO	ZIF-8/Carbon nanotubes	ZIF-8	Ni	0.46	Ni-N_4	98	34.3	−1.0 V vs. RHE	−0.32 V vs. RHE/n.d.	20 h at −0.8 V	H-type cell with two-compartments, anion exchange membrane (Nafion-117)	[127]
Fe-N/CNT@GNR-2/Carbon paper	0.1 M $KHCO_3$/CO	Commercial carbon nanotube/Hierarchical carbon nanotube and graphene nanoribbon networks	Urea	Fe	0.74	Fe-N_4	96	22.6	−0.76 V vs. RHE	n.d./650	5 h at −0.76 V	Two-chamber cell separated, nafion 115 membrane	[128]
Cu-SA/NPC/Carbon paper	0.1M $KHCO_3$/CH_3COCH_3	ZIF-8/Porous Carbon	ZIF-8	Cu	0.59	Fe-N_4 (Pyrrolic)	36.7	n.d.	−0.36 V vs. RHE	−0.16 V vs. RHE/250	n.d.	Airtight double-cell, Nafion 117 membrane	[152]
Fe-N-C/Glassy carbon	0.5M $KHCO_3$/CO	Polyaniline (PANI)/Carbon nanoroads	Urea	Fe	n.d.	Fe-N	95	1.9	−0.64 V vs. RHE	n.d./530	n.d.	Gas-tight classical H-cell	[135]
Ni-Sas@FNC/Carbon paper	0.5M $KHCO_3$/CO	Glucose/Carbon nanosheets	Melamine	Ni	5.92	Ni-N_4	95	25	−0.77 V vs. RHE	n.d.	10 h at −0.77 V	Two-compartment tight electrolytic-cell, Nafion 117 membrane	[137]

[a] Metal content, [b] Coordinate environment.

4. Metal Nanoparticles Supported on Carbon-Based Materials (M-NPs-C)

Supporting metal nanoparticles, metal oxides, or some sulfur metals (depending on the precursor) on carbon-based materials is another efficient way to obtain low-cost electrocatalysts, partly because metal nanoparticles can achieve good conversion efficiencies using lower metal loading and carbon materials support has reasonably priced. In addition, functionally they allow a good dispersion of the nanoparticles, they have good mechanical-electrical properties, and their structural properties are tunable, thus having better control of the active sites of the catalyst [172]. For example, Au bulk catalysts have been studied for the reduction of CO_2 to CO, which are expensive and scarce, therefore the possibility of using Au in the form of nanoparticles [173] dispersed on carbon paper allows to use a smaller amount of gold to obtain comparable faradic efficiencies with respect to a commercial Au rod. Thinking about processes with practical applications, the possibility of using cheaper and more abundant metals such as transition metals like Fe, Co, and Ni or the p-block [174–176] and type metals such as Bi, In, and Sn has also been considered. These metals are alternatives to noble metals (Au and Ag) and they have been found selective towards certain CO_2 reduction products, using them as nanoparticles dispersed on carbon-based materials.

A common material to support metal nanoparticles is commercial carbon black. Centi and co-workers [177] were among the first to demonstrate that Pt nanoparticles supported on Vulcan XC-72 improve the productivity of hydrocarbons with more than 5 carbons in a semi-half continuous cell in a gas phase electroreduction. Pérez and co-workers [178] used Vulcan XC-72R to support various non-noble metals (Cu, Co, Fe, Ni) through the impregnation methodology and, additionally, they also studied supported metal oxides, which were obtained by two reduction methodologies with borohydride and ethylene glycol. All catalysts showed an inhibition of the hydrogen evolution reaction and an improvement in the reduction of CO_2 to products such as formates or CO that could be adsorbed and transformed into even more reduced products. Sheng and co-workers [179] evaluated Pd nanoparticles (4 nm) supported on Vulcan carbon for the production of syngas with ratios between 0.5:1 and 1:1 at -0.5 at -0.6 V, with a total current density around 2.5 mA/cm^2 at -0.6 V. The selectivity of the catalyst was studied by means of two in-situ characterizations (XANES and EXAFS) and DFT theoretical calculations, finding that during the reduction of CO_2, the Pd nanoparticles are transformed into Pd hydride, a component that reduces the adsorption energy of *CO and *H products and thus allow them to be produced simultaneously with controlled selectivity. Xie and co-authors [180] supported Cu/In_2O_3 core/layer nanoparticles on carbon black also to synthesize syngas, obtaining H_2/CO ratios of 4:1 and 0.4:1 at -0.6 and -0.9 V vs. RHE, respectively, with much higher current density 12.5 mA/cm^2 at -0.9 V vs. RHE. For this case, the improvement in electrocatalytic results is related to the synergistic effect between compression stress on In_2O_3 layer and Cu doping, so that from these parameters it is also possible to tune the CO and H_2 ratios in a wide range. Silva and co-workers [181] prepared different types of these supported catalysts: The first type consisted of catalysts that supported metal particles in a range of 150–400 nm without carbon N-doping and the second type of catalysts contained Fe particles (50–100 nm) supported on the carbon matrix doped with nitrogen in the absence of Fe-N_4 residues. The firsts showed a very low their electrocatalytic performance towards CO_2 reduction whereas the later, produce CO with a FE of 66% towards CO at a low potential of -0.6 V vs. RHE, in addition to promoting the production of H_2, thus obtaining syngas ratios (CO/H_2) that can be tunable. The synthesis methodologies used by the previous authors indicate a process of two or several steps, however through the use of an anchoring agent (ligands with N,C,O,S atoms), nanoparticles immobilized on the carbonaceous support can be obtained in a direct synthesis and also allows to control the particles sized, to adjust the catalytic environment to improve CO_2 reduction and to prevent the aggregation effect of nanoparticles [182] as is the case of Kim and co-workers [183], who immobilized Ag nanoparticles on carbon black using cysteamine, tuning three different particle sizes (3, 5, and 10 nm) of which

5 nm presented the best electrochemical performance with an $FE_{(CO)}$ = 84.4% and a low overpotential over 300 mV. According to the DFT theoretical calculations, the decrease in the energy barrier can also be attributed to cysteamine since it allows modifying the spatial spin density of Ag nanoparticles, significantly reducing the overpotential. Jia and co-workers [184] supported metal nanoparticles (10 to 100 nm) on a carbon support derived from carbon black (Vulcan XC72R) doped with nitrogen, using two types of organic linkers. According to the characterizations by XDR and XPS, most of the catalysts contain more Ni particles instead of single atoms and the analysis by EXAFS confirms that Ni-Ni bonds predominate instead of Ni-N bonds. In addition, most of the Ni particles were wrapped in a carbon layer, which probably prevented the Ni nanoparticles from coming into direct contact with the aqueous electrolyte, significantly suppressing the HER obtaining a FE to H_2 of less than 10%. Within the determination of the active sites of the catalyst, they found that both nitrogen and Ni nanoparticles doping of the carbon black material play a key role in the conversion of CO_2 to CO obtaining a maximum FE of 94% at −0.7 V vs. RHE and current density of 22.7 mA/cm^2 at −1.1 V. On the contrary, individual Ni and N doping of the supports leads to low activity towards the electro-reduction of CO_2. Zhang and co-workers [185] evaluated two catalysts with Au nanoparticles supported on carbon black and graphitic carbon nitride (C_3N_4) finding that the latter catalyst achieved superior performance due to the formation of negative charges on the Au surface transferred by the support C_3N_4, allowing to stabilize the intermediate *COOH for its subsequent reduction to CO, reaching an FE of 90% with an overpotential of −340 mV vs. RHE. A similar behavior was found by the authors when supporting Ag nanoparticles on carbon black and C_3N_4. On this occasion, the interaction of the nanoparticles and C_3N_4 also led to stabilization of the intermediate and electrochemical improvement compared to catalysts based on carbon black. Zhao and co-authors [186] also used C_3N_4 as a support for Au nanoparticles, and unlike others, they incorporated carbon dots (CDots), which can accelerate the transport of electrons in the reduction and combined with the support can improve the adsorption of CO_2 and H^+. The ternary set of the Au-CDots-C_3N_4 catalyst reached an FE of ~79.8% at −0.5 V vs. RHE with an overpotential of 190 mV.

Zhang and co-workers [187] made a comparison between the commercial support Vulcan XC and graphene, doping them with nanoparticles of tin oxide obtained by hydrothermal method. An improvement in the catalytic activity was observed when using graphene as support, obtaining a faradic efficiency greater than 93% towards formate, with an improved current density of 13.1 mA/cm^2 at −1.8 V vs. SHE, while a current density of 6.2 mA/cm^2 at −1.8 V vs. SHE was obtained with the commercial support. The improvement of the catalytic activity was attributed to the strong interaction of the 2D structure of graphene with the aggregated nanoparticles, which can modify their electronic structures, influencing the adsorption and molecular reactivity of the surface. They also analyzed the dependence between the size of the tin oxide nanoparticles and the FE to formate, finding that the maximum FE is obtained when the particles have a size of 5 nm. Song and co-workers [188] also mention the strong interaction that graphene has with Cu nanoparticles due to site defects, which in this case improves selectivity towards ethanol at a low overpotential. The catalysts consisted of nitrogen-doped low-layered graphene that present a fold surface and intensive peaks called CNS carbon nanospikes. The nitrogen in the catalyst adjacent to the carbon atoms allow a polarization that can provide active sites close to Cu, allowing the intermediates to stabilize and then obtain ethanol as the majority product with an FE of 63% at −1.2 V vs. RHE, but with a relatively low current density (2 mA/cm^2 at −1.2 V vs. RHE). Recently Legrand and co-workers [189] used graphene nanoflakes (GNFs), which were synthesized by means of thermal plasma method to disperse copper nanoparticles. However, the nanoparticles were not homogeneously distributed due to the hydrophobicity of the nanostructure of the GNFs. Regarding its composition, they identified the presence of copper and sulfur, suggesting the existence of copper sulfide that improves the catalytic behavior towards formate obtaining in the best of cases a sample containing 46.4% Cu_2S with a superior electrochemical performance

(-15.9 mA/cm^2 at -0.9 V vs. RHE, FE = 40% at -0.6 V vs. RHE). Therefore, the presence of Cu_2S can improve the performance of the catalyst while decreasing the total amount of copper. Rogers and co-authors [190] synthesized a graphene nanoribbon (GNR) matrix to support Au nanoparticles from a bottom-up strategy, which allows to carry out a tuning at the molecular level introducing functional groups such as methyl carboxylate in the matrix, which leads to precise control in the catalytic environment. This is evidenced by the remarkable electrochemical performance ($FE_{(CO)} > 90\%$, onset potential at -0.37 to -0.87 V vs. RHE) and the change in the reaction mechanism when modifying the rate-determining step from CO_2 to CO.

Not long ago, nitrogen-doped graphene oxide (NGO) was also used as a support material by Yuan and co-workers [191], which in previous investigations used this material as a metal-free catalyst to reduce CO_2 to ethanol [48]. NGO was obtained using vitamin B6 (VB6) as N resource due to its low cost and as an alternative to conventional doping methods (thermal annealing of GO and chemical vapor deposition) observing that nitrogen functionalization of GO was favored by the carboxyl groups at the edges. On this occasion, they dope NGO with Cu nanoparticles in order to reduce the overpotential and improve the efficiency obtained previously. The authors determined that the catalytic ability of the catalysts is closely related to the amount of Cu in the catalyst; a maximum FE (ethanol) of 56.3% at -0.25 V vs. RHE and a low overpotential (η) of 0.140 V were obtained using a metal content of 10 wt.%. In fact, these results demonstrated the improvement of the electrocatalytic performance compared to the metal-free catalysts (FE = 36.4% at -0.4 V vs. RHE, η = 0.490 V) because the introduction of nitrogen, especially the pyridinic N species and Cu nanoparticles, provide more catalytic sites for the electro-reduction of CO_2 in addition to other characteristics, such as high conductivity and stabilization of intermediates such as CO*, then leading to the coupling of C-C bonds and blocking of reaction sites for HER (Figure 20). Ning and co-workers [192] found a similar behavior regarding the function of nitrogen species with supported nanoparticles in this case on nitrogen doped reduced graphene oxide (NrGO). They observed that the traces of N-pyridinic species in Cu_2O/NrGO allow promoting hydrogenation and the coupling of C-C bonds to later produce ethylene; the selectivity towards this product comes exclusively from the deposited Cu_2O nanoparticles, because only CO is obtained in a metal-free N-doped rGO catalyst. They also found that the rGO material can inhibit the growth of the Cu_2O nanocrystals, while the remaining nitrogen allows them to stabilize, allowing a high dispersion of these metal oxide nanoparticles on the support. With this catalyst a FE towards C_2H_4 of 19.7% at -1.4 V vs. RHE was obtained. Zeng co-workers [193] and Sun co-workers [194] also used rGO as support. In the first case, they decided to dope it with sulfur heteroatoms in addition to nitrogen heteroatoms, improving the conductivity of the material. The synthesis process consisted of a hydrothermal reaction at 180 °C for 3 h in which the support was doped using thiourea as heteroatoms precursors, at the same time nanoparticles of silver sulfide (Ag_2S) were formed; these were anchored to the support layers increasing the number of active sites for CO production. In the second case, the authors developed a hybrid electrocatalyst in which Bi and Bi_2O_3 nanoparticles were supported on the nitrogen-doped rGO, prepared by combining a heat treatment with a calcination process to partially reduce Bi_2O_3 to Bi, which generated a greater number of active sites, accelerating the intermediate reaction steps during the reduction of CO_2 to formate and thus, obtaining a good electrochemical performance with FE of 85% at -0.9 V vs. RHE and a low over potential of -0.5 V. On the other hand, Hossain and co-workers [195] also used rGO but without nitrogen doping to homogeneously support Cu nanoparticles (~10 nm), obtaining products such as CO, CH_4, and liquid products with a total FE of 76.6% at -0.4 V vs. RHE.

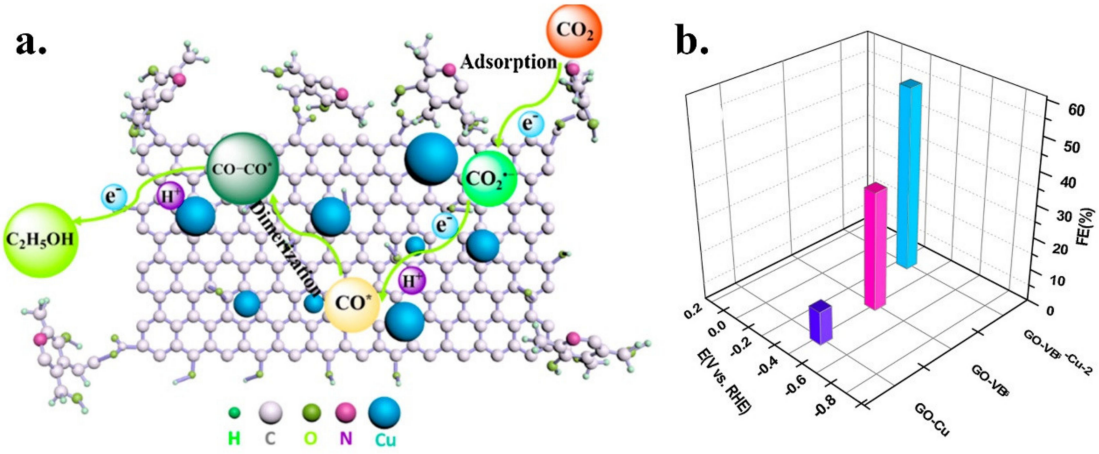

Figure 20. (**a**) CO* intermediate stabilization and dimerization process on nitrogen and copper doped graphene oxide catalysts and (**b**) comparison of electrochemical enhancement by doping GO with nitrogen and Cu simultaneously. Adapted from [191].

Supporting nanoparticles of metal alloys to date is still unknown and very rare to apply in the electrochemical reduction of CO_2. Genovese and co-workers [196] developed FeCu bimetallic catalysts supported on carbon nanotubes that were selective towards alcohols from 1 to 3 carbons. Xu and co-workers [197] recently developed a highly selective catalyst towards reducing CO_2 to CO, using bimetallic nanoparticle catalysts of Cu and Ni encapsulated in thin layers of graphene that prevent the particles aggregation and allow to obtain sizes of 12.5 nm. They mention that the metal Cu itself is one of the few that has a moderate CO_2 adsorption capacity, while Ni metal belongs to the group of cheap metals with a controllable morphology and composition. However, a high amount of the Cu component leads to a decrease in electron density in the catalyst and, consequently, a reduction of the selectivity to CO because the adsorption interaction of the intermediates is weakened (Figure 21a). Therefore, the optimal Cu to Ni ratio was found to be 0.25 (Figure 21b). The research shows a comparison with a single Ni metal catalyst that only shows selectivity towards the hydrogen evolution reaction; however, a suppression of HER and an improvement of the electrochemical performance is obtained by adding nanoparticles of Cu due to the presence of dual active sites. Wei and co-workers [198] used an alloy of In and Cu nanoparticles supported on carbon black in an in-situ synthesis controlling the molar radius In/Cu, which allowed adjusting the growth direction of the crystalline facets. They found that at an In/Cu ratio of 1.5/0.5, the In (101) facet is observed, which favors the production of HCOOH with an FE of 90% at −1.2 V vs. RHE.

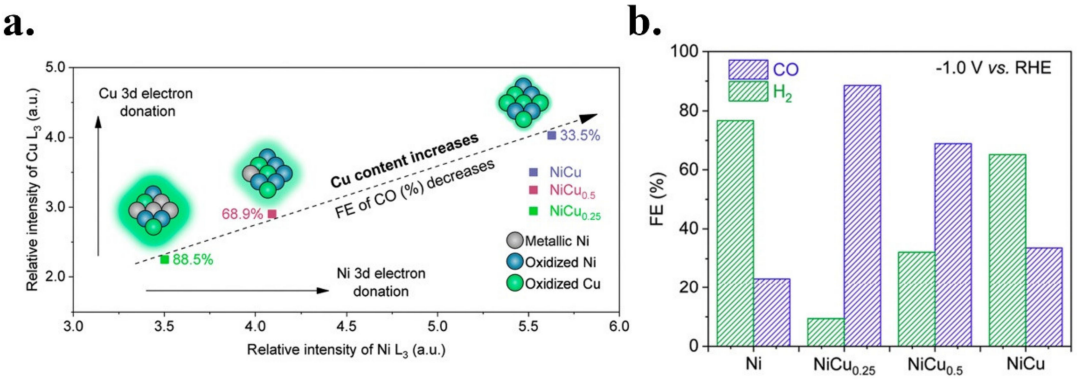

Figure 21. (**a**) Decrease in catalytic activity with increasing Cu content and (**b**) comparison of the electrochemical performance at −1.0 V vs. RHE of catalysts with different Cu to Ni ratio. Adapted from [197].

Nanotubes are another type of nanostructured carbon material that has been used previously by various authors. For example, Hossain and co-workers [199] and Zhang and co-workers [200] supported copper nanoparticles (3–60 nm) to obtain methanol and tin dioxide nanoparticles to obtain formate, respectively. To date, this material is still interesting due to its tubular structure and its resistance to acidic and basic environments [172,199]. Authors such as Zheng and co-workers [201], advocating the structural characteristics of these materials, studied the effect of confinement of Ni nanoparticles within carbon nanotubes for the production of CO. Theoretical studies carried out by the DFT reveal that the confinement effect can weaken the strong bond between the Ni nanoparticles and the intermediate CO*, thus improving the CO desorption process, which is the rate-determining step. On the other hand, Wang and co-workers [202] also obtained a good electrocatalytic performance when encapsulating Ni nanoparticles in nitrogen-doped carbon nanotubes, but in this investigation, the nanotubes were assembled on graphene to obtain a 3D hybrid material. This integration allows to reduce the irreversible aggregation problems that separate carbon materials have. This material with encapsulated Ni nanoparticles and abundant doped nitrogen atoms leads to a great improvement in the catalytic activity to produce CO (FE equal to 97.7% at −0.7 V vs. RHE). Lee and co-workers [203] studied the effect of the interfacial field in the CO_2 reduction reaction environment using Sn nanoparticles supported on entangled carbon nanotubes. Interfacial field modulation is a recent strategy that can have a significant impact on catalyst selectivity. By using carbon nanotubes, the authors increased the surface charge density of the catalyst, leading to a significant interfacial field on the Sn active sites that led to the formation of CO and not of formate, which is what was used to be seen with catalysts composed of Sn. The improvement in CO production is also related to catalyst potential of zero-charge (PZC), which is very positive due to the use of carbon nanotubes, in addition to their quality of being highly conductive.

Nanostructured materials such as carbon gels, xerogels, and aerogels, have also been used as matrices to obtain a good dispersion of the metal nanoparticles [204–206]. The method of obtaining these materials involves different stages: Gelation, curing, drying, and carbonization/activation, which influence the structural characteristics of these materials [207]. The control of the conditions in each of the processes allows adjusting the structural characteristics such as surface area, pore volume, and pore size distribution, allowing an easy design of supports for metal nanoparticles that have also been shown to be active for electrochemical CO_2 reduction [208]. Pérez-Cadenas and co-workers [209] used, for the first time, carbon xerogels doped with transition metals Ni (5.0 wt.%), Cu (7.1 wt.%) and Fe (6.5 wt.%) for the reduction of CO_2 to hydrocarbons. One of the main advantages that stand out from the catalysts obtained is that they were used directly as electrodes in a two-phase system due to their form of films (Figure 22a). Ni-doped carbon xerogels were selective towards C2 products, however Ni nanoparticles were encapsulated in the carbon structure, so a long induction period before detecting the first product was obtained with these materials in comparison with Cu or Fe-doped xerogels that had short induction periods, because the nanoparticles were located on the surface of the material. These Cu or Fe-doped xerogels were also more selective towards CH_4 and C3 products, respectively. These results showed that when using this type of catalyst, a production similar to that of traditional catalysts is obtained but using much less metal content. Later, Abdelwahab and co-workers [210] synthesized xerogels and aerogels doped with different amounts of cobalt, obtaining different products in the gas phase (C1–C4), which were quickly detected during the induction time. This behavior can be explained by the materials mesoporosity that allow easy access to the electrolyte. Additionally, a directly proportional relationship was observed between the amount of Co in the catalyst and the formation of hydrocarbons, since a greater amount of Co leads to a higher production, however it is also suggested to take into account the size of the particles and the pores texture. On the other hand, Castelo-Quibén and co-workers [211] used iron-doped catalysts composed of carbon xerogel and carbon nanofibers, obtaining hydrocarbons with 1 to 4 carbon numbers, but with greater

selectivity towards C4 type hydrocarbons. The effect of the iron nanoparticles size on the catalytic activity was also analyzed finding that a small size of particles characterized by XRD leads to high values of faradic efficiencies, for example, nanoparticles smaller than 4 nm significantly increase the formation of hydrocarbons (Figure 22b). In addition to the dependence on the size of the metal nanoparticles, the characteristics of the carbon material also play an important role. It is mentioned in previous research that when doping carbon gels with metal nanoparticles, some percentage was not accessible to the reactants [209,211]. In that sense, Castelo-Quibén and co-workers [212] synthesized Ni-based catalysts consisting of isolated mesoporous nanospheres doped with nanotubes (CNT) or nanohorns (CNH) by inverse emulsion polymerization of resorcinol and formaldehyde in presence of surfactants. The presence of mesopores allows the electrolyte to penetrate inside the carbon spheres reaching better accessibility to the active sites, while the nanostructured doping materials (CNT and CNH) reduce resistance by increasing electrical conductivity. Two types of surfactants, Span 80 and CTAB, were used in the synthesis to analyze their influence on the morphology of the material. Mesoporous nanospheres were obtained using Span 80, while when using CTBA a highly macroporous material with non-spherical morphology was obtained (Figure 22c). Ni-carbon mesoporous nanospheres were synthesized by two methodologies: (i) Doping during sol-gel synthesis or (ii) by impregnation of the prepared supports with a Ni salt solution. The catalysts doped with Ni nanoparticles by the first method do not improve the catalytic activity with respect to their supports (without doping) due to the Ni-particles embedding on the carbon matrix and thus the inaccessibility of reactants to the active sites, while the Ni-impregnated catalysts by the second method improve the activity to produce hydrocarbons, since it allowed place nickel on the surface of the nanospheres leaving the active sites exposed.

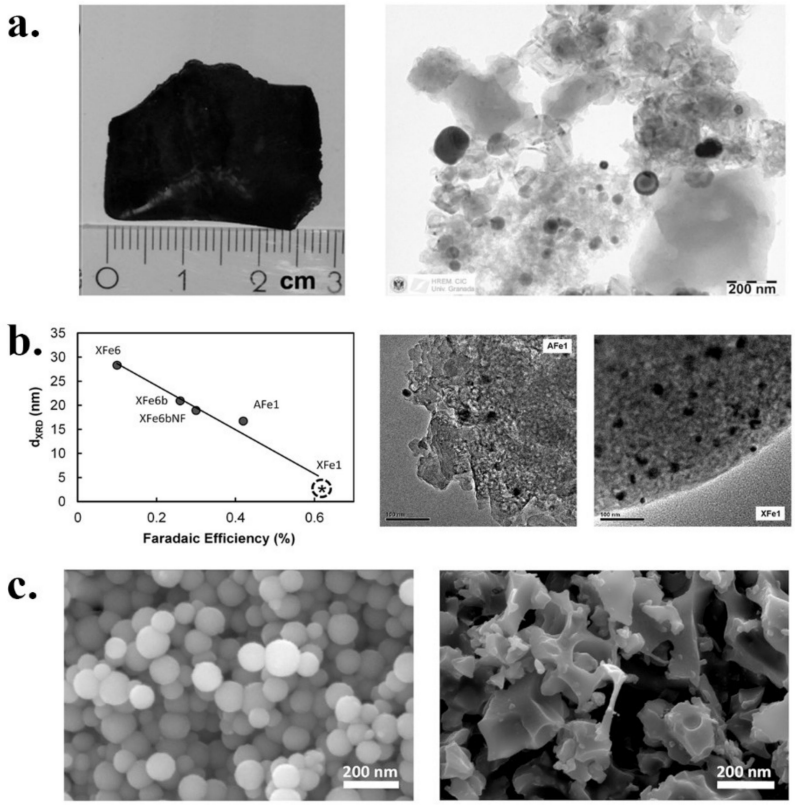

Figure 22. Carbon gels as metal nanoparticle supports in the electrochemical reduction of CO_2. (**a**) Photograph and HRTEM images of carbon xerogel supporting Ni nanoparticles, adapted from [209]. (**b**) Relationship between the size of iron particles by XDR vs. faradic efficiency (Left) and HRTEM images of Fe metal nanoparticles in carbon gels (right), adapted from [211]. (**c**) SEM images of carbon gels prepared using Span 80 and CTAB as surfactants, adapted from [213].

As a green-alternative to carbon gels, Castelo-Quibén and co-workers [212] proposed using plastic waste for the manufacture of carbon-based materials, which serve as supports to obtain low-cost electrocatalysts for the CO_2 electroreduction to hydrocarbons. The result was the obtaining of materials with overlapping carbon particles, in which hollow carbon nanofibers emerged and the Fe, Co, and Ni metal particles were located. All catalysts favor the formation of hydrocarbons from 1 to 4 carbons; for example, the copper catalyst showed a high selectivity towards C3 products, the nickel catalyst was selective towards CH_4, whereas the iron catalyst was the least selective, noting that it obtained a much larger mean metal particle size than the other two samples, so that the particle size of this metal can be related to the catalytic activity.

On the other hand, metal organic framework (MOF)-derived porous carbon materials have also been applied as supports to load metal nanoparticles. Zhang and co-workers [176] used this type of materials (ZIF-67) doped with nitrogen, which prevented the Bi nanoparticles from agglomerating and, in turn, embedded in the MOF structure, then obtaining a catalyst capable of generating formate. The supports allowed to obtain abundant active sites while Bi nanoparticles allowed to obtain a high electrocatalytic activity.

The use of metal nanoparticles dispersed on carbonaceous materials can also be part of gas diffusion electrodes (GDE), which allow the supply of CO_2 in the gaseous phase to the electrochemical cell, thus avoiding the limited solubility that CO_2 has in the electrolyte and reducing the limitations of mass transfer [214]. Specifically, the metal nanoparticles together with the carbonaceous support are part of the catalytic layer, which is deposited on a conductive material such as carbon paper, glassy carbon, carbon cloth, or metal meshes [215]. Several authors have used this strategy as an electrode in flow cells, for example Ma and co-workers [216] incorporated Ag nanoparticles in multiwall carbon nanotubes that were homogeneously distributed over the gas diffusion electrodes, obtaining a high catalytic activity towards CO (FE =< 95%, Jco = 350 mA/cm^2). Daiyan and co-workers [217] encapsulated metal nanoparticles in a graphitic carbon shell, which facilitated the adsorption of intermediaries in the reduction of CO_2 to CO. In addition, Ni nanoparticles were shielded, making the catalyst a more tolerant material to impurities such as SO_x and NO_x that CO_2 brings, as well as, tolerant to corrosive environments, so that the catalyst obtained a good 18 h stability and a current density of ~30 mA/cm^2 at 2.6 V in a gas diffusion system.

This revision (Table 8) collects different points to take into account to improve the design of catalysts that are based on the use of nanoparticles supported on carbon-based materials: (i) The catalytic activity is highly dependent on the support structural properties, as well as on the size of the nanoparticles and their dispersion; (ii) nanoparticles allows control of their surface morphology, a parameter that can be used to improve reaction kinetics and therefore electrochemical performance. (iii) Using ligands in the synthesis methodology allows to efficiently immobilize the nanoparticles, in addition to modifying their electrocatalytic and structural properties, becoming another way of adjusting the catalytic environment in order to improve the performance and tuning of the resulting reaction products; (iv) nanostructured carbon materials as supports are promising options for designing more efficient catalysts because they allow increasing the active surface area. In addition, it allows exploring different structural configurations, facilitating the design and adjustment of both the activity and selectivity of the reaction. (v) Nitrogen doping of supports has been shown to work synergistically with metal nanoparticles in the electrochemical reduction of CO_2 to stabilize reaction intermediates, in addition to improving electrical conductivity. However, future studies are needed that can clarify deeper details about the mechanism between nanoparticles and nitrogen species.

Table 8. Synthesis of metal nanoparticles supported on carbon-based materials and electrochemical performance.

Electrode	Electrolyte/Main Product	Precursor/Matrix	Nanoparticles	Metal Contents (wt. %)	FE %	J_{CO} [mA/cm^2]	Onset Potential	Stability	Experimental	Ref
Ni-NC-ATPA@C/Glassy carbon	0.5 M $KHCO_3$/CO	Carbon black Vulcan XC72R	Ni (10–100 nm)	~3.6	93.7 at −0.7 vs. RHE	22.7 at −1.1V	−0.5 V vs. RHE	54 h at −0.7 V	Gas-tight three electrode	[184]
Au-10/carbon paper	0.5 M $KHCO_3$/CO, syngas	Carbon paper TGP-H, Toray	Au (0.5–30 nm)	n.d.	78.08 at −0.59 V vs. RHE	0.8 at −0.59 V	n.d.	n.d.	Two-compartment electrochemical cell separated by a proton exchange membrane (Nafion®,117)	[173]
Fe/NC(NH_3)/Carbon cloth	0.5 M $KHCO_3$/CO, syngas	Carbon black Black Pearls	Fe	20	66 at −0.6 V vs. RHE	n.d.	n.d.	n.d.	Undivided cell, three electrodes	[181]
Nano-SnO_2/graphene/glassy carbon	0.1M $NaHCO_3$/Formate	Graphene	Sn (5 nm)	~30	93.6% at −1.8 V vs. SCE	13.1 at −1.8 V vs. SCE	−0.34 V vs. RHE.	18 h at −1.8 V	gas-tight two compartment electrochemical cell	[178]
Cu/CNS	0.1 M $KHCO_3$/Ethanol	N-doped Graphene	Cu (39.18 nm)	n.d.	63% at −1.2 V vs. RHE	2 at −1.2 V vs. RHE	−0.3 V vs. RHE.	6 h at −1.2 V	Two-compartment electrochemical cell separated by an anion exchange membrane (Selemion AMV, AGC)	[187]
Cu/GNFs/carbon cloth	0.1 M $KHCO_3$/Formate	Graphene nanoflakes	Cu	20–50	40% at −0.6 V vs. RHE	15.9 at −0.9 V vs. RHE	−0.40 V vs. RHE	n.d.	Two-compartment electrochemical cell separated by a proton exchange membrane (Nafion®)	[189]
GO-VB6-Cu-2/Carbon paper	0.1 M $KHCO_3$/Ethanol	N-doped GO	Cu (2–12 nm)	10	5.3% at −0.25 V vs. RHE	4.571 at −0.25 vs. RHE	0.140 V vs. RHE.	10 h at −0.25 V	H-type cell separated by a Nafion 117 ion exchange membrane	[191]
Cu2O/NRGO/glassy carbon	0.1 M $KHCO_3$/C_2H_4	N-doped rGO	Cu_2O (90 nm)	5.94	19.7 at −1.3 V vs. RHE	10 at −1.3 V vs. RHE	n.d.	1000 s at −1.4 V	H-type cell with two compartments separated by a proton exchange membrane (Nafion 117, Dupont).	[191]
Cu-rGO	0.1 M $NaHCO_3$/CO,CH_4, Liquid products	rGO	Cu (10 nm)	n.d.	76.6 at −0.4 V vs. RHE	n.d.	n.d.	14 h at −0.5 V	Gas-tight two-compartment electrochemical cell cationic exchange membrane (CMI-7000S)	[195]
Ag_2S/N-S-doped rGO/Glassy carbon	0.1 M $KHCO_3$/CO	N-S doped rGO	Ag_2S (50 nm)	~70	87.4 at −0.76 V vs. RHE	~70 μA cm^{-2}	−0.34 V vs. RHE	40 h at −0.76 V	Double-chamber electrochemical cell partitioned by a Nafion 117 membrane	[193]
Bi/Bi_2O_3/NrGO-700	0.5 M $KHCO_3$/Formate	N-doped rGO	Bi/Bi_2O_3 (20 nm)	17.6	85 at −0.9 V vs. RHE	18 at −0.9 V vs. RHE	−0.5 V vs. RHE	10 h at −0.9 V	H-type three electrodecell.	[194]

Table 8. *Cont.*

Electrode	Electrolyte/Main Product	Precursor/Matrix	Nanoparticles	Metal Contents (wt. %)	FE %	J_{CO} [mA/cm^2]	Onset Potential	Stability	Experimental	Ref
NiCu0.25/glassy carbon	0.1 M $KHCO_3$/CO	Graphene	Cu/Ni (12.5 nm)	ratio Cu/Ni 0.25	88.5 at −1.0 V vs. RHE	n.d.	−0.7 V vs. RHE	3000 s at −1.0 V	Three-electrode H-cell separated by a proton exchange membrane (Nafion 117)	[197]
N/NiNPs@CNT/G	0.5 M $KHCO_3$/CO	N-doped nanotube (CNT) assembled on the surface of graphene	Ni (50–75 nm)	n.d.	97.7 at −0.7 V vs. RHE	7.9 at −0.7 V	−0.3 V vs. RHE	10 h at −0.7V	Three-electrode H-type electrolytic cell with Nafion membrane	[202]
20%-Cu/CNTs/Carbon paper	0.5 M $NaHCO_3$/Methanol	Nanotubes CNTs	Cu (3–60 nm)	20%	38.4 at −1.7 V vs. SCE	17.5 at −1.5 V	−0.5 V vs. SCE	6000 s at −1.7 V	H-type cell with anode and cathode compartments separated by proton conducting Nafion 117 membrane.	[199]
SnO_2/N-MWCNTs/Glassy carbon	0.1 M $KHCO_3$/Formate	N-doped multiwalled carbon nanotubes (N-MWCNTs)	SnO_2	42.5%	46 at −0.9 V vs. Ag/AgCl	~5 at −1.3 V	n.d.	10 h at −1.3 V	Undivided three-electrode cell	[200]
Ni@NCNTs/Carbon paper	0.5 M $KHCO_3$/CO	N- doped nanotubes	Ni (50–100 nm)	26%	99.1 at −0.8 V vs. RHE	8.01 at −0.72 V	−0.3 V vs. RHE	10 h at −0.8 V	H-typethree-electrode cell, separated by a proton membrane (Nafion 117)	[201]
Bi@NPC/Glassy carbon	0.1 M $KHCO_3$/Formate	Metal organic framework (MOF)-derived porous carbon material	Bi (~20 nm)	22.6%	92 at −1.5 V SCE	14.4 at −1.5 V	−1.2 V vs. SCE	20 h at −1.5 V	Gastight electrolytic Three electrode cell	[176]
AgNP/MWCNTs/GDE	0.1 M KOH/CO	MWCNTs	Ag	n.d.	95% at −0.77 V vs. RHE	338 at −0.77 V vs. RHE	−0.1 V vs. RHE	n.d.	Electrochemicalflow reactor	[216]
Ni@NC-900/Carbon fiber paper	0.1 M $KHCO_3$/CO	Carbon shells	Ni (~0.203 nm)	~3	96% at −1 V vs. RHE	17.5 at −1 V vs. RHE	0.89 V	1 h at −0.9 V	Two compartment gas-tight H-cell (Nafion membrane)	[217]
	0.1 M $KHCO_3$/CO				85%	~30 at 2.6 V	n.d.	18 h at 2.6 V	GDE system (Sustainion X37-50 membrane)	
5nm Ag/C/Glassy carbon plate	0.5 M $KHCO_3$/CO	Carbon black	Ag (5 nm)	n.d.	84.4% at −0.75 V RHE	~4 at −0.75 V RHE	0.64 V	n.d.	Two-compartmentelectrochemical cell, Nafion 117 membrane	[183]

5. Conclusions

This review includes different types of nanostructured carbons-based materials that have been used for the development of electrocatalysts applied to the reduction of CO_2, giving evidence that these materials serve as platforms to obtain increasingly fitted catalysts for this application. Besides, the metal content ranges on a scale that goes from nanoparticles, through single atoms to the non-use of metals, which in all cases brings more advantages than the use of bulk metals, such as low cost, ease in controlling the reaction, and at the same time, factors like electrocatalytic activity, stability, and selectivity are improved.

Another point to take into account in future developments is doping with heteroatoms, since among the case studies in which they are used regardless of whether they are catalysts with nanoparticles, single atoms, or metal-free, these influenced the improvement of the efficiency of the catalyst. In the case of metal-free catalysts doped with heteroatoms, the control of these factors depends on the location, charge, and type of heteroatom used on the carbonaceous matrix, parameters that can be adjusted through different synthesis processes. For catalysts with metals on the single atom scale, the coordination environment of active sites can be adjusted by tuning the carbonaceous matrix structures leading to improved electrochemical performance. Catalysts with nanoparticles supported on nanostructured carbons can also lead to improved reaction kinetics, in addition to adjusting selectivity by manipulating the morphology of the nanoparticles and the structure of the supports. In addition to the advantage of tuning in the chemical, surface, and textural parameters offered by carbon-based catalysts, it should be noted that they have an excellent electrical conductivity that positively influences the electrochemical results, and they are very versatile in their synthesis methodologies allowing simple, economic, and environmentally conscious processes each time, aspects that must continue to be pointed out in future research for their scalability. Although nitrogen functionalities are the most studied, it is recommended to delve into other heteroatoms such as F, S, B, and P, because all of them can lead to a charge redistribution and change the characteristic electro-neutrality of carbonaceous materials. Consequently, they can modify the catalytic properties of the catalyst. Additionally, the process of functionalization of the carbonaceous matrix is advantageous when designing catalysts that contain nanoparticles or simple atoms since it helps to stabilize and avoid their agglomeration. In fact, this should be the way to modify the catalytic environment of the active sites and therefore maximize the electro-catalytic performance of the CO_2 reduction to valuable products.

Author Contributions: Conceptualization, A.F.P.-C., F.C.-M. and E.B.-G.; methodology, A.F.P.-C., F.C.-M., L.D.R.-V. and E.B.-G.; investigation L.D.R.-V. and E.B.-G.; writing—original draft preparation, L.D.R.-V.; writ-ing—review and editing, A.F.P.-C., L.D.R.-V. and E.B.-G.; supervision, A.F.P.-C. and E.B.-G.; project administration, F.C.-M. and E.B.-G.; funding acquisition, F.C.-M. and E.B.-G. All authors have read and agreed to the published version of the manuscript.

Funding: This research was funded by Spanish Ministry of Science, Innovation and Universities, grant number RTI2018-099224-B-I00; and Junta de Andalucía, grant numbers P12-RNM-2892, P18-RTJ-2974 and RNM172. L.D.R.V. was funded by MINCIENCIAS.

Data Availability Statement: Data sharing not applicable.

Acknowledgments: The authors thank the financial support of the Spanish Ministry of Science, Innovation and Universities (project RTI2018-099224-B-I00) and Junta de Andalucía (Project P12-RNM-2892, P18-RTJ-2974 and RNM172). L.D. Ramírez-Valencia is grateful to the Colombian Ministry of Sciences, Technology and Innovation (MINCIENCIAS) for supporting her PhD studies.

Conflicts of Interest: The authors declare no conflict of interest.

References

1. Kaneco, S.; Kurimoto, H.; Shimizu, Y.; Ohta, K.; Mizuno, T. Photocatalytic reduction of CO_2 using TiO_2 powders in supercritical fluid CO_2. *Energy* **1999**, *24*, 21–30. [CrossRef]
2. Mori, K.; Yamashita, H.; Anpo, M. Photocatalytic reduction of CO_2 with H_2O on various titanium oxide photocatalysts. *RSC Adv.* **2012**, *2*, 3165–3172. [CrossRef]
3. Xie, S.; Zhang, Q.; Liu, G.; Wang, Y. Photocatalytic and photoelectrocatalytic reduction of CO_2 using heterogeneous catalysts with controlled nanostructures. *Chem. Commun.* **2016**, *52*, 35–59. [CrossRef]
4. Wang, C.; Sun, Z.; Zheng, Y.; Hu, Y.H. Recent progress in visible light photocatalytic conversion of carbon dioxide. *J. Mater. Chem. A* **2019**, *7*, 865–887. [CrossRef]
5. Chueh, W.C.; Haile, S.M. Ceria as a Thermochemical Reaction Medium for Selectively Generating Syngas or Methane from H_2O and CO_2. *ChemSusChem* **2009**, *2*, 735–739. [CrossRef] [PubMed]
6. Frey, M.; Édouard, D.; Roger, A.-C. Optimization of structured cellular foam-based catalysts for low-temperature carbon dioxide methanation in a platelet milli-reactor. *C. R. Chim.* **2015**, *18*, 283–292. [CrossRef]
7. Roy, S.; Cherevotan, A.; Peter, S.C. Thermochemical CO_2 Hydrogenation to Single Carbon Products: Scientific and Technological Challenges. *ACS Energy Lett.* **2018**, *3*, 1938–1966. [CrossRef]
8. Ali, N.; Bilal, M.; Nazir, M.S.; Khan, A.; Ali, F.; Iqbal, H.M.N. Thermochemical and electrochemical aspects of carbon dioxide methanation: A sustainable approach to generate fuel via waste to energy theme. *Sci. Total Environ.* **2020**, *712*, 136482. [CrossRef]
9. Grodkowski, J.; Neta, P. Copper-Catalyzed Radiolytic Reduction of CO_2 to CO in Aqueous Solutions. *J. Phys. Chem. B* **2001**, *105*, 4967–4972. [CrossRef]
10. Ramirez-Corredores, M.M.; Gadikota, G.; Huang, E.E.; Gaffney, A.M. Radiation-Induced Chemistry of Carbon Dioxide: A Pathway to Close the Carbon Loop for a Circular Economy. *Front. Energy Res.* **2020**, *8*, 108. [CrossRef]
11. Machado, I.M.P.; Atsumi, S. Cyanobacterial biofuel production. *J. Biotechnol.* **2012**, *162*, 50–56. [CrossRef]
12. Rabinovitch-Deere, C.A.; Oliver, J.W.K.; Rodriguez, G.M.; Atsumi, S. Synthetic Biology and Metabolic Engineering Approaches To Produce Biofuels. *Chem. Rev.* **2013**, *113*, 4611–4632. [CrossRef] [PubMed]
13. Rittmann, S.; Seifert, A.; Herwig, C. Essential prerequisites for successful bioprocess development of biological CH_4 production from CO_2 and H_2. *Crit. Rev. Biotechnol.* **2015**, *35*, 141–151. [CrossRef] [PubMed]
14. Scibioh, M.A.; Viswanathan, B. Chapter 6—Biochemical Reduction of CO_2. In *Carbon Dioxide to Chemicals and Fuels*; Scibioh, M.A., Viswanathan, B., Eds.; Elsevier: Amsterdam, The Netherlands, 2018; pp. 255–306, ISBN 978-0-444-63996-7.
15. Sun, D.; Chen, Y. *Electrochemical Reduction of Carbon Dioxide Fundamentals and Technologies*; CRC Press: Boca Raton, FL, USA, 2016; ISBN 9781315099316.
16. Tuci, G.; Filippi, J.; Rossin, A.; Luconi, L.; Pham-Huu, C.; Yakhvarov, D.; Vizza, F.; Giambastiani, G. CO_2 electrochemical reduction by exohedral N-pyridine decorated metal-free carbon nanotubes. *Energies* **2020**, *13*, 2703. [CrossRef]
17. Jia, C.; Dastafkan, K.; Ren, W.; Yang, W.; Zhao, C. Carbon-based catalysts for electrochemical CO_2 reduction. *Sustain. Energy Fuels* **2019**, *3*, 2890–2906. [CrossRef]
18. Irabien, A.; Alvarez-Guerra, M.; Albo, J.; Dominguez-Ramos, A. *Electrochemical Conversion of CO_2 to Value-Added Products*; Elsevier Inc.: Amsterdam, The Netherlands, 2018; ISBN 9780128131602.
19. Mondal, B.; Song, J.; Neese, F.; Ye, S. Bio-inspired mechanistic insights into CO_2 reduction. *Curr. Opin. Chem. Biol.* **2015**, *25*, 103–109. [CrossRef] [PubMed]
20. Mikkelsen, M.; Jørgensen, M.; Krebs, F.C. The teraton challenge. A review of fixation and transformation of carbon dioxide. *Energy Environ. Sci.* **2010**, *3*, 43–81. [CrossRef]
21. Sharma, P.P.; Wu, J.; Yadav, R.M.; Liu, M.; Wright, C.J.; Tiwary, C.S.; Yakobson, B.I.; Lou, J.; Ajayan, P.M.; Zhou, X.-D. Nitrogen-Doped Carbon Nanotube Arrays for High-Efficiency Electrochemical Reduction of CO_2: On the Understanding of Defects, Defect Density, and Selectivity. *Angew. Chem.* **2015**, *127*, 13905–13909. [CrossRef]
22. Fernandes, D.M.; Peixoto, A.F.; Freire, C. Nitrogen-doped metal-free carbon catalysts for (electro)chemical CO_2 conversion and valorisation. *Dalt. Trans.* **2019**, *48*, 13508–13528. [CrossRef]
23. Navalon, S.; Dhakshinamoorthy, A.; Alvaro, M.; Garcia, H. Carbocatalysis by Graphene-Based Materials. *Chem. Rev.* **2014**, *114*, 6179–6212. [CrossRef]
24. Ji, Y.; Shi, Y.; Liu, C.; Zhang, B. Plasma-regulated N-doped carbon nanotube arrays for efficient electrosynthesis of syngas with a wide CO/H_2 ratio. *Sci. China Mater.* **2020**, *63*, 1–7. [CrossRef]
25. Hu, C.; Dai, L. Doping of Carbon Materials for Metal-Free Electrocatalysis. *Adv. Mater.* **2019**, *31*, 1804672. [CrossRef]
26. Duan, X.; Xu, J.; Wei, Z.; Ma, J.; Guo, S.; Wang, S.; Liu, H.; Dou, S. Metal-Free Carbon Materials for CO_2 Electrochemical Reduction. *Adv. Mater.* **2017**, *29*, 1701784. [CrossRef]
27. Liu, W.; Qi, J.; Bai, P.; Zhang, W.; Xu, L. Utilizing spatial confinement effect of N atoms in micropores of coal-based metal-free material for efficiently electrochemical reduction of carbon dioxide. *Appl. Catal. B Environ.* **2020**, *272*, 118974. [CrossRef]
28. Gao, K.; Wang, B.; Tao, L.; Cunning, B.V.; Zhang, Z.; Wang, S.; Ruoff, R.S.; Qu, L. Efficient Metal-Free Electrocatalysts from N-Doped Carbon Nanomaterials: Mono-Doping and Co-Doping. *Adv. Mater.* **2019**, *31*, 1–11. [CrossRef] [PubMed]
29. Liu, D.; Tao, L.; Yan, D.; Zou, Y.; Wang, S. Recent Advances on Non-precious Metal Porous Carbon-based Electrocatalysts for Oxygen Reduction Reaction. *ChemElectroChem* **2018**, *5*, 1775–1785. [CrossRef]
30. Inagaki, M.; Toyoda, M.; Soneda, Y.; Morishita, T. Nitrogen-doped carbon materials. *Carbon* **2018**, *132*, 104–140. [CrossRef]

31. Zhu, Y.; Lv, K.; Wang, X.; Yang, H.; Xiao, G.; Zhu, Y. 1D/2D nitrogen-doped carbon nanorod arrays/ultrathin carbon nanosheets: Outstanding catalysts for the highly efficient electroreduction of CO_2 to CO. *J. Mater. Chem. A* **2019**, *7*, 14895–14903. [CrossRef]
32. Wu, J.; Yadav, R.M.; Liu, M.; Sharma, P.P.; Tiwary, C.S.; Ma, L.; Zou, X.; Zhou, X.; Yakobson, B.I.; Lou, J.; et al. Achieving Highly Efficient, Selective, and Stable CO_2 Reduction on Nitrogen-Doped Carbon Nanotubes. *ACS Nano* **2015**, *9*, 5364–5371. [CrossRef] [PubMed]
33. Li, H.; Xiao, N.; Hao, M.; Song, X.; Wang, Y.; Ji, Y.; Liu, C.; Li, C.; Guo, Z.; Zhang, F.; et al. Efficient CO_2 electroreduction over pyridinic-N active sites highly exposed on wrinkled porous carbon nanosheets. *Chem. Eng. J.* **2018**, *351*, 613–621. [CrossRef]
34. Jhong, H.R.M.; Tornow, C.E.; Smid, B.; Gewirth, A.A.; Lyth, S.M.; Kenis, P.J.A. A Nitrogen-Doped Carbon Catalyst for Electrochemical CO_2 Conversion to CO with High Selectivity and Current Density. *ChemSusChem* **2017**, *10*, 1094–1099. [CrossRef]
35. Xu, J.; Kan, Y.; Huang, R.; Zhang, B.; Wang, B.; Wu, K.H.; Lin, Y.; Sun, X.; Li, Q.; Centi, G.; et al. Revealing the Origin of Activity in Nitrogen-Doped Nanocarbons towards Electrocatalytic Reduction of Carbon Dioxide. *ChemSusChem* **2016**, *9*, 1085–1089. [CrossRef] [PubMed]
36. Li, C.; Wang, Y.; Xiao, N.; Li, H.; Ji, Y.; Guo, Z.; Liu, C.; Qiu, J. Nitrogen-doped porous carbon from coal for high efficiency CO_2 electrocatalytic reduction. *Carbon* **2019**, *151*, 46–52. [CrossRef]
37. Wu, J.; Liu, M.; Sharma, P.P.; Yadav, R.M.; Ma, L.; Yang, Y.; Zou, X.; Zhou, X.D.; Vajtai, R.; Yakobson, B.I.; et al. Incorporation of Nitrogen Defects for Efficient Reduction of CO_2 via Two-Electron Pathway on Three-Dimensional Graphene Foam. *Nano Lett.* **2016**, *16*, 466–470. [CrossRef] [PubMed]
38. Kuang, M.; Guan, A.; Gu, Z.; Han, P.; Qian, L.; Zheng, G. Enhanced N-doping in mesoporous carbon for efficient electrocatalytic CO_2 conversion. *Nano Res.* **2019**, *12*, 2324–2329. [CrossRef]
39. Zhang, H.; Min, S.; Wang, F.; Zhang, Z.; Kong, C. Efficient electrocatalytic CO_2 reduction to CO with high selectivity using a N-doped carbonized wood membrane. *New J. Chem.* **2020**, *44*, 6125–6129. [CrossRef]
40. Wang, H.; Chen, Y.; Hou, X.; Ma, C.; Tan, T. Nitrogen-doped graphenes as efficient electrocatalysts for the selective reduction of carbon dioxide to formate in aqueous solution. *Green Chem.* **2016**, *18*, 3250–3256. [CrossRef]
41. Zhang, S.; Kang, P.; Ubnoske, S.; Brennaman, M.K.; Song, N.; House, R.L.; Glass, J.T.; Meyer, T.J. Polyethylenimine-enhanced electrocatalytic reduction of CO_2 to formate at nitrogen-doped carbon nanomaterials. *J. Am. Chem. Soc.* **2014**, *136*, 7845–7848. [CrossRef]
42. Wang, H.; Jia, J.; Song, P.; Wang, Q.; Li, D.; Min, S.; Qian, C.; Wang, L.; Li, Y.F.; Ma, C.; et al. Efficient Electrocatalytic Reduction of CO_2 by Nitrogen-Doped Nanoporous Carbon/Carbon Nanotube Membranes: A Step Towards the Electrochemical CO_2 Refinery. *Angew. Chem. Int. Ed.* **2017**, *56*, 7847–7852. [CrossRef]
43. Chen, Z.; Mou, K.; Yao, S.; Liu, L. Highly selective electrochemical reduction of CO_2 to formate on metal-free nitrogen-doped PC61BM. *J. Mater. Chem. A* **2018**, *6*, 11236–11243. [CrossRef]
44. Li, H.; Xiao, N.; Wang, Y.; Li, C.; Ye, X.; Guo, Z.; Pan, X.; Liu, C.; Bai, J.; Xiao, J.; et al. Nitrogen-doped tubular carbon foam electrodes for efficient electroreduction of CO_2 to syngas with potential-independent CO/H_2 ratios. *J. Mater. Chem. A* **2019**, *7*, 18852–18860. [CrossRef]
45. Liu, K.H.; Zhong, H.X.; Yang, X.Y.; Bao, D.; Meng, F.L.; Yan, J.M.; Zhang, X.B. Composition-tunable synthesis of "clean" syngas: Via a one-step synthesis of metal-free pyridinic-N-enriched self-supported CNTs: The synergy of electrocatalyst pyrolysis temperature and potential. *Green Chem.* **2017**, *19*, 4284–4288. [CrossRef]
46. Song, Y.; Chen, W.; Zhao, C.; Li, S.; Wei, W.; Sun, Y. Metal-Free Nitrogen-Doped Mesoporous Carbon for Electroreduction of CO_2 to Ethanol. *Angew. Chem. Int. Ed.* **2017**, *56*, 10840–10844. [CrossRef] [PubMed]
47. Song, Y.; Wang, S.; Chen, W.; Li, S.; Feng, G.; Wei, W.; Sun, Y. Enhanced Ethanol Production from CO_2 Electroreduction at Micropores in Nitrogen-Doped Mesoporous Carbon. *ChemSusChem* **2020**, *13*, 293–297. [CrossRef] [PubMed]
48. Yuan, J.; Zhi, W.Y.; Liu, L.; Yang, M.P.; Wang, H.; Lu, J.X. Electrochemical reduction of CO_2 at metal-free N-functionalized graphene oxide electrodes. *Electrochim. Acta* **2018**, *282*, 694–701. [CrossRef]
49. Sun, X.; Kang, X.; Zhu, Q.; Ma, J.; Yang, G.; Liu, Z.; Han, B. Very highly efficient reduction of CO_2 to CH_4 using metal-free N-doped carbon electrodes. *Chem. Sci.* **2016**, *7*, 2883–2887. [CrossRef]
50. Wei, J.; Zhou, D.; Sun, Z.; Deng, Y.; Xia, Y.; Zhao, D. A Controllable Synthesis of Rich Nitrogen-Doped Ordered Mesoporous Carbon for CO_2 Capture and Supercapacitors. *Adv. Funct. Mater.* **2013**, *23*, 2322–2328. [CrossRef]
51. Cui, X.; Pan, Z.; Zhang, L.; Peng, H.; Zheng, G. Selective Etching of Nitrogen-Doped Carbon by Steam for Enhanced Electrochemical CO_2 Reduction. *Adv. Energy Mater.* **2017**, *7*, 1701456. [CrossRef]
52. Liu, Y.; Zhao, J.; Cai, Q. Pyrrolic-nitrogen doped graphene: A metal-free electrocatalyst with high efficiency and selectivity for the reduction of carbon dioxide to formic acid: A computational study. *Phys. Chem. Chem. Phys.* **2016**, *18*, 5491–5498. [CrossRef]
53. Daiyan, R.; Saputera, W.H.; Masood, H.; Leverett, J.; Lu, X.; Amal, R. A Disquisition on the Active Sites of Heterogeneous Catalysts for Electrochemical Reduction of CO_2 to Value-Added Chemicals and Fuel. *Adv. Energy Mater.* **2020**, *10*, 1902106. [CrossRef]
54. Wu, J.; Ma, S.; Sun, J.; Gold, J.I.; Tiwary, C.; Kim, B.; Zhu, L.; Chopra, N.; Odeh, I.N.; Vajtai, R.; et al. A metal-free electrocatalyst for carbon dioxide reduction to multi-carbon hydrocarbons and oxygenates. *Nat. Commun.* **2016**, *7*, 13869. [CrossRef] [PubMed]
55. Chai, G.-L.; Guo, Z.-X. Highly effective sites and selectivity of nitrogen-doped graphene/CNT catalysts for CO_2 electrochemical reduction. *Chem. Sci.* **2016**, *7*, 1268–1275. [CrossRef] [PubMed]

56. Du, C.; Wang, X.; Chen, W.; Feng, S.; Wen, J.; Wu, Y.A. CO_2 transformation to multicarbon products by photocatalysis and electrocatalysis. *Mater. Today Adv.* **2020**, *6*, 100071. [CrossRef]
57. Mohamed, A.G.A.; Huang, Y.; Xie, J.; Borse, R.A.; Parameswaram, G.; Wang, Y. Metal-free sites with multidimensional structure modifications for selective electrochemical CO_2 reduction. *Nano Today* **2020**, *33*, 100891. [CrossRef]
58. Hernández, S.; Farkhondehfal, M.A.; Sastre, F.; Makkee, M.; Saracco, G.; Russo, N. Syngas production from electrochemical reduction of CO_2: Current status and prospective implementation. *Green Chem.* **2017**, *19*, 2326–2346. [CrossRef]
59. Hiragond, C.B.; Kim, H.; Lee, J.; Sorcar, S.; Erkey, C.; In, S. Il Electrochemical CO_2 reduction to CO catalyzed by 2D nanostructures. *Catalysts* **2020**, *10*, 98. [CrossRef]
60. Liu, S.; Yang, H.; Huang, X.; Liu, L.; Cai, W.; Gao, J.; Li, X.; Zhang, T.; Huang, Y.; Liu, B. Identifying Active Sites of Nitrogen-Doped Carbon Materials for the CO_2 Reduction Reaction. *Adv. Funct. Mater.* **2018**, *28*, 1800499. [CrossRef]
61. Siahrostami, S.; Jiang, K.; Karamad, M.; Chan, K.; Wang, H.; Nørskov, J. Theoretical Investigations into Defected Graphene for Electrochemical Reduction of CO_2. *ACS Sustain. Chem. Eng.* **2017**, *5*, 11080–11085. [CrossRef]
62. Seredych, M.; Hulicova-Jurcakova, D.; Lu, G.Q.; Bandosz, T.J. Surface functional groups of carbons and the effects of their chemical character, density and accessibility to ions on electrochemical performance. *Carbon* **2008**, *46*, 1475–1488. [CrossRef]
63. Yasuda, S.; Yu, L.; Kim, J.; Murakoshi, K. Selective nitrogen doping in graphene for oxygen reduction reactions. *Chem. Commun.* **2013**, *49*, 9627–9629. [CrossRef]
64. Jia, Y.; Zhang, L.; Du, A.; Gao, G.; Chen, J.; Yan, X.; Brown, C.L.; Yao, X. Defect Graphene as a Trifunctional Catalyst for Electrochemical Reactions. *Adv. Mater.* **2016**, *28*, 9532–9538. [CrossRef] [PubMed]
65. Daiyan, R.; Tan, X.; Chen, R.; Saputera, W.H.; Tahini, H.A.; Lovell, E.; Ng, Y.H.; Smith, S.C.; Dai, L.; Lu, X.; et al. Electroreduction of CO_2 to CO on a Mesoporous Carbon Catalyst with Progressively Removed Nitrogen Moieties. *ACS Energy Lett.* **2018**, *3*, 2292–2298. [CrossRef]
66. Hursán, D.; Samu, A.A.; Janovák, L.; Artyushkova, K.; Asset, T.; Atanassov, P.; Janáky, C. Morphological Attributes Govern Carbon Dioxide Reduction on N-Doped Carbon Electrodes. *Joule* **2019**, *3*, 1719–1733. [CrossRef]
67. Lee, J.; Kim, J.; Hyeon, T. Recent Progress in the Synthesis of Porous Carbon Materials. *Adv. Mater.* **2006**, *18*, 2073–2094. [CrossRef]
68. Lee, J.H.; Kattel, S.; Jiang, Z.; Xie, Z.; Yao, S.; Tackett, B.M.; Xu, W.; Marinkovic, N.S.; Chen, J.G. Tuning the activity and selectivity of electroreduction of CO_2 to synthesis gas using bimetallic catalysts. *Nat. Commun.* **2019**, *10*, 1–8. [CrossRef]
69. Sanz, R.; Calleja, G.; Arencibia, A.; Sanz-Pérez, E.S. Development of high efficiency adsorbents for CO_2 capture based on a double-functionalization method of grafting and impregnation. *J. Mater. Chem. A* **2013**, *1*, 1956–1962. [CrossRef]
70. Gong, K.; Du, F.; Xia, Z.; Durstock, M.; Dai, L. Nitrogen-Doped Carbon Nanotube Arrays with High Electrocatalytic Activity for Oxygen Reduction. *Science* **2009**, *323*, 760–763. [CrossRef] [PubMed]
71. Qiao, J.; Liu, Y.; Hong, F.; Zhang, J. A review of catalysts for the electroreduction of carbon dioxide to produce low-carbon fuels. *Chem. Soc. Rev.* **2014**, *43*, 631–675. [CrossRef] [PubMed]
72. Zhang, W.; Hu, Y.; Ma, L.; Zhu, G.; Wang, Y.; Xue, X.; Chen, R.; Yang, S.; Jin, Z. Progress and Perspective of Electrocatalytic CO_2 Reduction for Renewable Carbonaceous Fuels and Chemicals. *Adv. Sci.* **2018**, *5*, 1700275. [CrossRef]
73. Dutta, S.; Bhaumik, A.; Wu, K.C.W. Hierarchically porous carbon derived from polymers and biomass: Effect of interconnected pores on energy applications. *Energy Environ. Sci.* **2014**, *7*, 3574–3592. [CrossRef]
74. Zou, X.; Liu, M.; Wu, J.; Ajayan, P.M.; Li, J.; Liu, B.; Yakobson, B.I. How Nitrogen-Doped Graphene Quantum Dots Catalyze Electroreduction of CO_2 to Hydrocarbons and Oxygenates. *ACS Catal.* **2017**, *7*, 6245–6250. [CrossRef]
75. Sreekanth, N.; Nazrulla, M.A.; Vineesh, T.V.; Sailaja, K.; Phani, K.L. Metal-free boron-doped graphene for selective electroreduction of carbon dioxide to formic acid/formate. *Chem. Commun.* **2015**, *51*, 16061–16064. [CrossRef]
76. Einaga, Y. Diamond electrodes for electrochemical analysis. *J. Appl. Electrochem.* **2010**, *40*, 1807–1816. [CrossRef]
77. Ivandini, T.A.; Einaga, Y. Polycrystalline boron-doped diamond electrodes for electrocatalytic and electrosynthetic applications. *Chem. Commun.* **2017**, *53*, 1338–1347. [CrossRef]
78. Nakata, K.; Ozaki, T.; Terashima, C.; Fujishima, A.; Einaga, Y. High-yield electrochemical production of formaldehyde from CO_2 and seawater. *Angew. Chem. Int. Ed.* **2014**, *53*, 871–874. [CrossRef] [PubMed]
79. Jiwanti, P.K.; Natsui, K.; Nakata, K.; Einaga, Y. Selective production of methanol by the electrochemical reduction of CO_2 on boron-doped diamond electrodes in aqueous ammonia solution. *RSC Adv.* **2016**, *6*, 102214–102217. [CrossRef]
80. Natsui, K.; Iwakawa, H.; Ikemiya, N.; Nakata, K.; Einaga, Y. Stable and Highly Efficient Electrochemical Production of Formic Acid from Carbon Dioxide Using Diamond Electrodes. *Angew. Chem. Int. Ed.* **2018**, *57*, 2639–2643. [CrossRef]
81. Ikemiya, N.; Natsui, K.; Nakata, K.; Einaga, Y. Effect of alkali-metal cations on the electrochemical reduction of carbon dioxide to formic acid using boron-doped diamond electrodes. *RSC Adv.* **2017**, *7*, 22510–22514. [CrossRef]
82. Tomisaki, M.; Natsui, K.; Ikemiya, N.; Nakata, K.; Einaga, Y. Influence of Electrolyte on the Electrochemical Reduction of Carbon Dioxide Using Boron-Doped Diamond Electrodes. *ChemistrySelect* **2018**, *3*, 10209–10213. [CrossRef]
83. Xu, J.; Natsui, K.; Naoi, S.; Nakata, K.; Einaga, Y. Effect of doping level on the electrochemical reduction of CO_2 on boron-doped diamond electrodes. *Diam. Relat. Mater.* **2018**, *86*, 167–172. [CrossRef]
84. Tomisaki, M.; Kasahara, S.; Natsui, K.; Ikemiya, N.; Einaga, Y. Switchable Product Selectivity in the Electrochemical Reduction of Carbon Dioxide Using Boron-Doped Diamond Electrodes. *J. Am. Chem. Soc.* **2019**, *141*, 7414–7420. [CrossRef] [PubMed]
85. Xu, J.; Einaga, Y. Effect of sp2 species in a boron-doped diamond electrode on the electrochemical reduction of CO_2. *Electrochem. Commun.* **2020**, *115*, 106731. [CrossRef]

86. Xie, J.; Zhao, X.; Wu, M.; Li, Q.; Wang, Y.; Yao, J. Metal-Free Fluorine-Doped Carbon Electrocatalyst for CO_2 Reduction Outcompeting Hydrogen Evolution. *Angew. Chem. Int. Ed.* **2018**, *57*, 9640–9644. [CrossRef]
87. Ni, W.; Xue, Y.; Zang, X.; Li, C.; Wang, H.; Yang, Z.; Yan, Y.-M. Fluorine Doped Cagelike Carbon Electrocatalyst: An Insight into the Structure-Enhanced CO Selectivity for CO_2 Reduction at High Overpotential. *ACS Nano* **2020**, *14*, 2014–2023. [CrossRef] [PubMed]
88. Liu, T.; Ali, S.; Lian, Z.; Si, C.; Su, D.S.; Li, B. Phosphorus-doped onion-like carbon for CO_2 electrochemical reduction: The decisive role of the bonding configuration of phosphorus. *J. Mater. Chem. A* **2018**, *6*, 19998–20004. [CrossRef]
89. Zhao, T.; Tian, Y.; Yan, L.; Su, Z. Heteroatom-doped C_3N as a promising metal-free catalyst for a high-efficiency carbon dioxide reduction reaction. *New J. Chem.* **2020**, *44*, 11824–11828. [CrossRef]
90. Mao, X.; Kour, G.; Zhang, L.; He, T.; Wang, S.; Yan, C.; Zhu, Z.; Du, A. Silicon-doped graphene edges: An efficient metal-free catalyst for the reduction of CO_2 into methanol and ethanol. *Catal. Sci. Technol.* **2019**, *9*, 6800–6807. [CrossRef]
91. Wang, G.; Liu, M.; Jia, J.; Xu, H.; Zhao, B.; Lai, K.; Tu, C.; Wen, Z. Nitrogen and Sulfur Co-doped Carbon Nanosheets for Electrochemical Reduction of CO_2. *ChemCatChem* **2020**, *12*, 2203–2208. [CrossRef]
92. Pan, F.; Li, B.; Deng, W.; Du, Z.; Gang, Y.; Wang, G.; Li, Y. Promoting electrocatalytic CO_2 reduction on nitrogen-doped carbon with sulfur addition. *Appl. Catal. B Environ.* **2019**, *252*, 240–249. [CrossRef]
93. Xie, J.; Ghausi, M.A.; Wang, J.; Wang, X.; Wang, W.; Yang, R.; Wu, M.; Zhang, Q.; Wang, Y. Low-Energy CO_2 Reduction on a Metal-Free Carbon Material. *ChemElectroChem* **2020**, *7*, 2145–2150. [CrossRef]
94. Chen, S.; Liu, T.; Olanrele, S.O.; Lian, Z.; Si, C.; Chen, Z.; Li, B. Boosting electrocatalytic activity for CO_2 reduction on nitrogen-doped carbon catalysts by co-doping with phosphorus. *J. Energy Chem.* **2021**, *54*, 143–150. [CrossRef]
95. Jia, C.; Ren, W.; Chen, X.; Yang, W.; Zhao, C. (N, B) Dual Heteroatom-Doped Hierarchical Porous Carbon Framework for Efficient Electroreduction of Carbon Dioxide. *ACS Sustain. Chem. Eng.* **2020**, *8*, 6003–6010. [CrossRef]
96. Liu, Y.; Zhang, Y.; Cheng, K.; Quan, X.; Fan, X.; Su, Y.; Chen, S.; Zhao, H.; Zhang, Y.; Yu, H.; et al. Selective Electrochemical Reduction of Carbon Dioxide to Ethanol on a Boron- and Nitrogen-Co-doped Nanodiamond. *Angew. Chem. Int. Ed.* **2017**, *56*, 15607–15611. [CrossRef] [PubMed]
97. Zhang, H.; Liu, G.; Shi, L.; Ye, J. Single-Atom Catalysts: Emerging Multifunctional Materials in Heterogeneous Catalysis. *Adv. Energy Mater.* **2018**, *8*, 1701343. [CrossRef]
98. Yang, X.-F.; Wang, A.; Qiao, B.; Li, J.; Liu, J.; Zhang, T. Single-Atom Catalysts: A New Frontier in Heterogeneous Catalysis. *Acc. Chem. Res.* **2013**, *46*, 1740–1748. [CrossRef]
99. Li, M.; Wang, H.; Luo, W.; Sherrell, P.C.; Chen, J.; Yang, J. Heterogeneous Single-Atom Catalysts for Electrochemical CO_2 Reduction Reaction. *Adv. Mater.* **2020**, *32*, 1–24. [CrossRef]
100. Hou, C.-C.; Wang, H.-F.; Li, C.; Xu, Q. From metal–organic frameworks to single/dual-atom and cluster metal catalysts for energy applications. *Energy Environ. Sci.* **2020**, *13*, 1658–1693. [CrossRef]
101. Jeong, H.Y.; Balamurugan, M.; Choutipalli, V.S.K.; Jo, J.; Baik, H.; Subramanian, V.; Kim, M.; Sim, U.; Nam, K.T. Tris(2-benzimidazolylmethyl)amine-Directed Synthesis of Single-Atom Nickel Catalysts for Electrochemical CO Production from CO_2. *Chem. A Eur. J.* **2018**, *24*, 18444–18454. [CrossRef] [PubMed]
102. Li, X.; Rong, H.; Zhang, J.; Wang, D.; Li, Y. Modulating the local coordination environment of single-atom catalysts for enhanced catalytic performance. *Nano Res.* **2020**, *13*, 1842–1855. [CrossRef]
103. Nguyen, T.N.; Salehi, M.; Van Le, Q.; Seifitokaldani, A.; Dinh, C.T. Fundamentals of Electrochemical CO_2 Reduction on Single-Metal-Atom Catalysts. *ACS Catal.* **2020**, *10*, 10068–10095. [CrossRef]
104. Peng, Y.; Lu, B.; Chen, S. Carbon-Supported Single Atom Catalysts for Electrochemical Energy Conversion and Storage. *Adv. Mater.* **2018**, *30*, 1–25. [CrossRef] [PubMed]
105. Romanchuk, A.Y.; Slesarev, A.S.; Kalmykov, S.N.; Kosynkin, D.V.; Tour, J.M. Graphene oxide for effective radionuclide removal. *Phys. Chem. Chem. Phys.* **2013**, *15*, 2321–2327. [CrossRef]
106. Jiang, K.; Siahrostami, S.; Zheng, T.; Hu, Y.; Hwang, S.; Stavitski, E.; Peng, Y.; Dynes, J.; Gangisetty, M.; Su, D.; et al. Isolated Ni single atoms in graphene nanosheets for high-performance CO_2 reduction. *Energy Environ. Sci.* **2018**, *11*, 893–903. [CrossRef]
107. Zhang, C.; Yang, S.; Wu, J.; Liu, M.; Yazdi, S.; Ren, M.; Sha, J.; Zhong, J.; Nie, K.; Jalilov, A.S.; et al. Electrochemical CO_2 Reduction with Atomic Iron-Dispersed on Nitrogen-Doped Graphene. *Adv. Energy Mater.* **2018**, *1703487*, 1–9. [CrossRef]
108. Cheng, Y.; Zhao, S.; Li, H.; He, S.; Veder, J.P.; Johannessen, B.; Xiao, J.; Lu, S.; Pan, J.; Chisholm, M.F.; et al. Unsaturated edge-anchored Ni single atoms on porous microwave exfoliated graphene oxide for electrochemical CO_2. *Appl. Catal. B Environ.* **2019**, *243*, 294–303. [CrossRef]
109. Zhang, H.; Li, J.; Xi, S.; Du, Y.; Hai, X.; Wang, J.; Xu, H.; Wu, G.; Zhang, J.; Lu, J.; et al. A Graphene-Supported Single-Atom FeN 5 Catalytic Site for Efficient Electrochemical CO_2 Reduction. *Angew. Chem. Int. Ed.* **2019**, *58*, 14871–14876. [CrossRef]
110. Ren, X.; Liu, S.; Li, H.; Ding, J.; Liu, L.; Kuang, Z.; Li, L.; Yang, H.; Bai, F.; Huang, Y.; et al. Electron-withdrawing functional ligand promotes CO_2 reduction catalysis in single atom catalyst. *Sci. China Ser. B Chem.* **2020**, *63*, 1727–1733. [CrossRef]
111. Li, X.; Chai, G.; Xu, X.; Liu, J.; Zhong, Z.; Cao, A.; Tao, Z.; You, W.; Kang, L. Electrocatalytic reduction of CO_2 to CO over iron phthalocyanine-modified graphene nanocomposites. *Carbon* **2020**, *167*, 658–667. [CrossRef]
112. Yang, H.; Hung, S.-F.; Liu, S.; Yuan, K.; Miao, S.; Zhang, L.; Huang, X.; Wang, H.-Y.; Cai, W.; Chen, R.; et al. Atomically dispersed Ni(i) as the active site for electrochemical CO_2 reduction. *Nat. Energy* **2018**, *3*, 140–147. [CrossRef]

113. Tuo, J.; Zhu, Y.; Jiang, H.; Shen, J.; Li, C. The Effect of Coordination Environment of Atomically Dispersed Fe and N Co-doped Carbon Nanosheets on CO_2 Electroreduction. *ChemElectroChem* **2020**, *7*, 4767–4772. [CrossRef]
114. Back, S.; Lim, J.; Kim, N.Y.; Kim, Y.H.; Jung, Y. Single-atom catalysts for CO_2 electroreduction with significant activity and selectivity improvements. *Chem. Sci.* **2017**, *8*, 1090–1096. [CrossRef] [PubMed]
115. He, H.; Jagvaral, Y. Electrochemical reduction of CO_2 on graphene supported transition metals-towards single atom catalysts. *Phys. Chem. Chem. Phys.* **2017**, *19*, 11436–11446. [CrossRef] [PubMed]
116. Zhu, Y.; Li, X.; Wang, X.; Lv, K.; Xiao, G.; Feng, J.; Jiang, X.; Fang, M.; Zhu, Y. Single-Atom Iron-Nitrogen Catalytic Site with Graphitic Nitrogen for Efficient Electroreduction of CO_2. *ChemistrySelect* **2020**, *5*, 1282–1287. [CrossRef]
117. Yan, C.; Ye, Y.; Lin, L.; Wu, H.; Jiang, Q.; Wang, G.; Bao, X. Improving CO_2 electroreduction over ZIF-derived carbon doped with Fe-N sites by an additional ammonia treatment. *Catal. Today* **2019**, *330*, 252–258. [CrossRef]
118. Pan, F.; Zhang, H.; Liu, K.; Cullen, D.; More, K.; Wang, M.; Feng, Z.; Wang, G.; Wu, G.; Li, Y. Unveiling Active Sites of CO_2 Reduction on Nitrogen-Coordinated and Atomically Dispersed Iron and Cobalt Catalysts. *ACS Catal.* **2018**, *8*, 3116–3122. [CrossRef]
119. Lu, P.; Yang, Y.; Yao, J.; Wang, M.; Dipazir, S.; Yuan, M.; Zhang, J.; Wang, X.; Xie, Z.; Zhang, G. Facile synthesis of single-nickel-atomic dispersed N-doped carbon framework for efficient electrochemical CO_2 reduction. *Appl. Catal. B Environ.* **2019**, *241*, 113–119. [CrossRef]
120. Zhao, C.; Dai, X.; Yao, T.; Chen, W.; Wang, X.; Wang, J.; Yang, J.; Wei, S.; Wu, Y.; Li, Y. Ionic Exchange of Metal-Organic Frameworks to Access Single Nickel Sites for Efficient Electroreduction of CO_2. *J. Am. Chem. Soc.* **2017**, *139*, 8078–8081. [CrossRef]
121. Pan, F.; Zhang, H.; Liu, Z.; Cullen, D.; Liu, K.; More, K.; Wu, G.; Wang, G.; Li, Y. Atomic-level active sites of efficient imidazolate framework-derived nickel catalysts for CO_2 reduction. *J. Mater. Chem. A* **2019**, *7*, 26231–26237. [CrossRef]
122. Geng, Z.; Cao, Y.; Chen, W.; Kong, X.; Liu, Y.; Yao, T.; Lin, Y. Regulating the coordination environment of Co single atoms for achieving efficient electrocatalytic activity in CO_2 reduction. *Appl. Catal. B Environ.* **2019**, *240*, 234–240. [CrossRef]
123. Gu, J.; Hsu, C.S.; Bai, L.; Chen, H.M.; Hu, X. Atomically dispersed Fe3+ sites catalyze efficient CO_2 electroreduction to CO. *Science* **2019**, *364*, 1091–1094. [CrossRef]
124. Chen, X.; Ma, D.D.; Chen, B.; Zhang, K.; Zou, R.; Wu, X.T.; Zhu, Q.L. Metal–organic framework-derived mesoporous carbon nanoframes embedded with atomically dispersed Fe–N_x active sites for efficient bifunctional oxygen and carbon dioxide electroreduction. *Appl. Catal. B Environ.* **2020**, *267*, 118720. [CrossRef]
125. Zhang, C.; Fu, Z.; Zhao, Q.; Du, Z.; Zhang, R.; Li, S. Single-atom-Ni-decorated, nitrogen-doped carbon layers for efficient electrocatalytic CO_2 reduction reaction. *Electrochem. Commun.* **2020**, *116*, 106758. [CrossRef]
126. Wang, T.; Sang, X.; Zheng, W.; Yang, B.; Yao, S.; Lei, C.; Li, Z.; He, Q.; Lu, J.; Lei, L.; et al. Gas Diffusion Strategy for Inserting Atomic Iron Sites into Graphitized Carbon Supports for Unusually High-Efficient CO_2 Electroreduction and High-Performance Zn–CO_2 Batteries. *Adv. Mater.* **2020**, *32*, e2002430. [CrossRef]
127. Hou, Y.; Liang, Y.L.; Shi, P.C.; Huang, Y.B.; Cao, R. Atomically dispersed Ni species on N-doped carbon nanotubes for electroreduction of CO_2 with nearly 100% CO selectivity. *Appl. Catal. B Environ.* **2020**, *271*, 118929. [CrossRef]
128. Pan, F.; Li, B.; Sarnello, E.; Fei, Y.; Gang, Y.; Xiang, X.; Du, Z.; Zhang, P.; Wang, G.; Nguyen, H.T.; et al. Atomically Dispersed Iron-Nitrogen Sites on Hierarchically Mesoporous Carbon Nanotube and Graphene Nanoribbon Networks for CO_2 Reduction. *ACS Nano* **2020**, *14*, 5506–5516. [CrossRef]
129. Li, X.; Bi, W.; Chen, M.; Sun, Y.; Ju, H.; Yan, W.; Zhu, J.; Wu, X.; Chu, W.; Wu, C.; et al. Exclusive Ni-N_4 Sites Realize Near-Unity CO Selectivity for Electrochemical CO_2 Reduction. *J. Am. Chem. Soc.* **2017**, *139*, 14889–14892. [CrossRef]
130. Zhao, S.; Cheng, Y.; Veder, J.; Johannessen, B.; Saunders, M.; Zhang, L.; Liu, C.; Chisholm, M.F.; De Marco, R.; Liu, J.; et al. One-Pot Pyrolysis Method to Fabricate Carbon Nanotube Supported Ni Single-Atom Catalysts with Ultrahigh Loading. *ACS Appl. Energy Mater.* **2018**, *1*, 5286–5297. [CrossRef]
131. Cheng, Y.; Zhao, S.; Johannessen, B.; Veder, J.; Saunders, M.; Rowles, M.R.; Cheng, M.; Liu, C.; Chisholm, M.F.; De Marco, R.; et al. Atomically Dispersed Transition Metals on Carbon Nanotubes with Ultrahigh Loading for Selective Electrochemical Carbon Dioxide Reduction. *Adv. Mater.* **2018**, *30*, e1706287. [CrossRef]
132. Lu, Y.; Wang, H.; Yu, P.; Yuan, Y.; Shahbazian-Yassar, R.; Sheng, Y.; Wu, S.; Tu, W.; Liu, G.; Kraft, M.; et al. Isolated Ni single atoms in nitrogen doped ultrathin porous carbon templated from porous g-C_3N_4 for high-performance CO_2 reduction. *Nano Energy* **2020**, *77*, 105158. [CrossRef]
133. Ni, W.; Liu, Z.; Zhang, Y.; Ma, C.; Deng, H.; Zhang, S.; Wang, S. Electroreduction of Carbon Dioxide Driven by the Intrinsic Defects in the Carbon Plane of a Single Fe–N_4 Site. *Adv. Mater.* **2020**, *33*, e2003238. [CrossRef]
134. Tuo, J.; Zhu, Y.; Cheng, L.; Li, Y.; Yang, X.; Shen, J.; Li, C. Layered Confinement Reaction: Atomic-level Dispersed Iron–Nitrogen Co-Doped Ultrathin Carbon Nanosheets for CO_2 Electroreduction. *ChemSusChem* **2019**, *12*, 2644–2650. [CrossRef]
135. Wu, S.; Lv, X.; Ping, D.; Zhang, G.; Wang, S.; Wang, H.; Yang, X.; Guo, D.; Fang, S. Highly exposed atomic Fe–N active sites within carbon nanorods towards electrocatalytic reduction of CO_2 to CO. *Electrochim. Acta* **2020**, *340*, 135930. [CrossRef]
136. He, Q.; Lee, J.H.; Liu, D.; Liu, Y.; Lin, Z.; Xie, Z.; Hwang, S.; Kattel, S.; Song, L.; Chen, J.G. Accelerating CO_2 Electroreduction to CO Over Pd Single-Atom Catalyst. *Adv. Funct. Mater.* **2020**, *30*, 1–8. [CrossRef]
137. Han, S.G.; Ma, D.D.; Zhou, S.H.; Zhang, K.; Wei, W.B.; Du, Y.; Wu, X.T.; Xu, Q.; Zou, R.; Zhu, Q.L. Fluorine-tuned single-atom catalysts with dense surface Ni-N_4 sites on ultrathin carbon nanosheets for efficient CO_2 electroreduction. *Appl. Catal. B Environ.* **2021**, *283*, 119591. [CrossRef]

138. Chen, Y.; Ma, L.; Chen, C.; Hu, W.; Zou, L.; Zou, Z.; Yang, H. Fe and N co-doped carbon with High doping content of sulfur and nitrogen for efficient CO_2 electro-reduction. *J. CO_2 Util.* **2020**, *42*, 101316. [CrossRef]
139. Xiong, W.; Li, H.; Wang, H.; Yi, J.; You, H.; Zhang, S.; Hou, Y.; Cao, M.; Zhang, T.; Cao, R. Hollow Mesoporous Carbon Sphere Loaded Ni–N_4 Single-Atom: Support Structure Study for CO_2 Electrocatalytic Reduction Catalyst. *Small* **2020**, *16*, 2003943. [CrossRef] [PubMed]
140. Wang, N.; Liu, Z.; Ma, J.; Liu, J.; Zhou, P.; Chao, Y.; Ma, C.; Bo, X.; Liu, J.; Hei, Y.; et al. Sustainability Perspective-Oriented Synthetic Strategy for Zinc Single-Atom Catalysts Boosting Electrocatalytic Reduction of Carbon Dioxide and Oxygen. *ACS Sustain. Chem. Eng.* **2020**, *8*, 13813–13822. [CrossRef]
141. Abbas, S.A.; Song, J.T.; Tan, Y.C.; Nam, K.M.; Oh, J.; Jung, K. Synthesis of a Nickel Single-Atom Catalyst Based on $Ni-N_{4-x}C_x$ Active Sites for Highly Efficient CO_2 Reduction Utilizing a Gas Diffusion Electrode. *ACS Appl. Energy Mater.* **2020**, *3*, 8739–8745. [CrossRef]
142. Ni, Y.; Miao, L.; Wang, J.; Liu, J.; Yuan, M.; Chen, J. Pore size effect of graphyne supports on CO_2 electrocatalytic activity of Cu single atoms. *Phys. Chem. Chem. Phys.* **2020**, *22*, 1181–1186. [CrossRef]
143. Xu, H.; Cheng, D.; Cao, D.; Zeng, X.C. Publisher Correction: A universal principle for a rational design of single-atom electrocatalysts. *Nat. Catal.* **2018**, *1*, 632. [CrossRef]
144. Liu, J.; Qiao, S.Z.; Liu, H.; Chen, J.; Orpe, A.; Zhao, D.; Lu, G.Q. (Max) Extension of The Stöber Method to the Preparation of Monodisperse Resorcinol–Formaldehyde Resin Polymer and Carbon Spheres. *Angew. Chemie Int. Ed.* **2011**, *50*, 5947–5951. [CrossRef]
145. Pan, Y.; Lin, R.; Chen, Y.; Liu, S.; Zhu, W.; Cao, X.; Chen, W.; Wu, K.; Cheong, W.C.; Wang, Y.; et al. Design of Single-Atom Co-N_5 Catalytic Site: A Robust Electrocatalyst for CO_2 Reduction with Nearly 100% CO Selectivity and Remarkable Stability. *J. Am. Chem. Soc.* **2018**, *140*, 4218–4221. [CrossRef]
146. Ma, S.; Su, P.; Huang, W.; Jiang, S.P.; Bai, S.; Liu, J. Atomic Ni Species Anchored N-Doped Carbon Hollow Spheres as Nanoreactors for Efficient Electrochemical CO_2 Reduction. *ChemCatChem* **2019**, *11*, 6092–6098. [CrossRef]
147. Jeong, H.Y.; Balamurugan, M.; Choutipalli, V.S.K.; Jeong, E.S.; Subramanian, V.; Sim, U.; Nam, K.T. Achieving highly efficient CO_2 to CO electroreduction exceeding 300 mA cm-2 with single-atom nickel electrocatalysts. *J. Mater. Chem. A* **2019**, *7*, 10651–10661. [CrossRef]
148. Chen, Y.; Zou, L.; Liu, H.; Chen, C.; Wang, Q.; Gu, M.; Yang, B.; Zou, Z.; Fang, J.; Yang, H. Fe and N Co-Doped Porous Carbon Nanospheres with High Density of Active Sites for Efficient CO_2 Electroreduction. *J. Phys. Chem. C* **2019**, *123*, 16651–16659. [CrossRef]
149. Pan, F.; Li, B.; Sarnello, E.; Fei, Y.; Feng, X.; Gang, Y.; Xiang, X.; Fang, L.; Li, T.; Hu, Y.H.; et al. Pore-Edge Tailoring of Single-Atom Iron−Nitrogen Sites on Graphene for Enhanced CO_2 Reduction. *ACS Catal.* **2020**, *10*, 10803–10811. [CrossRef]
150. Fang, M.; Wang, X.; Li, X.; Zhu, Y.; Xiao, G.; Feng, J.; Jiang, X.; Lv, K.; Zhu, Y.; Lin, W.F. Curvature-induced Zn3d Electron Return on Zn−N_4 Single-atom Carbon Nanofibers for Boosting Electroreduction of CO_2. *ChemCatChem* **2020**, *13*, 603–609. [CrossRef]
151. Mou, K.; Chen, Z.; Zhang, X.; Jiao, M.; Zhang, X.; Ge, X.; Zhang, W.; Liu, L. Highly Efficient Electroreduction of CO_2 on Nickel Single-Atom Catalysts: Atom Trapping and Nitrogen Anchoring. *Small* **2019**, *15*, e1903668. [CrossRef]
152. Ma, Z.; Zhang, X.; Wu, D.; Han, X.; Zhang, L.; Wang, H.; Xu, F.; Gao, Z.; Jiang, K. Ni and nitrogen-codoped ultrathin carbon nanosheets with strong bonding sites for efficient CO_2 electrochemical reduction. *J. Colloid Interface Sci.* **2020**, *570*, 31–40. [CrossRef] [PubMed]
153. Yang, F.; Mao, X.; Ma, M.; Jiang, C.; Zhang, P.; Wang, J.; Deng, Q.; Zeng, Z.; Deng, S. Scalable strategy to fabricate single Cu atoms coordinated carbons for efficient electroreduction of CO_2 to CO. *Carbon* **2020**, *168*, 528–535. [CrossRef]
154. Takele Menisa, L.; Cheng, P.; Long, C.; Qiu, X.; Zheng, Y.; Han, J.; Zhang, Y.; Gao, Y.; Tang, Z. Insight into atomically dispersed porous M-N-C single-site catalysts for electrochemical CO_2 reduction. *Nanoscale* **2020**, *12*, 16617–16626. [CrossRef] [PubMed]
155. Yang, F.; Song, P.; Liu, X.; Mei, B.; Xing, W.; Jiang, Z.; Gu, L.; Xu, W. Highly Efficient CO_2 Electroreduction on ZnN_4-based Single-Atom Catalyst. *Angew. Chem. Int. Ed.* **2018**, *57*, 12303–12307. [CrossRef]
156. Li, F.; Hong, S.; Wu, T.S.; Li, X.; Masa, J.; Soo, Y.L.; Sun, Z. Atomically Dispersed Nickel Sites for Selective Electroreduction of CO_2. *ACS Appl. Energy Mater.* **2019**, *2*, 8836–8842. [CrossRef]
157. He, Y.; Li, Y.; Zhang, J.; Wang, S.; Huang, D.; Yang, G.; Yi, X.; Lin, H.; Han, X.; Hu, W.; et al. Low-temperature strategy toward Ni-NC@Ni core-shell nanostructure with Single-Ni sites for efficient CO_2 electroreduction. *Nano Energy* **2020**, *77*, 105010. [CrossRef]
158. Song, X.; Zhang, H.; Yang, Y.; Zhang, B.; Zuo, M.; Cao, X.; Sun, J.; Lin, C.; Li, X.; Jiang, Z. Bifunctional Nitrogen and Cobalt Codoped Hollow Carbon for Electrochemical Syngas Production. *Adv. Sci.* **2018**, *5*, 1–8. [CrossRef] [PubMed]
159. He, Q.; Liu, D.; Lee, J.H.; Liu, Y.; Xie, Z.; Hwang, S.; Kattel, S.; Song, L.; Chen, J.G. Electrochemical Conversion of CO_2 to Syngas with Controllable CO/H_2 Ratios over Co and Ni Single-Atom Catalysts. *Angew. Chem. Int. Ed.* **2020**, *59*, 3033–3037. [CrossRef]
160. Zhu, W.; Fu, J.; Liu, J.; Chen, Y.; Li, X.; Huang, K.; Cai, Y.; He, Y.; Zhou, Y.; Su, D.; et al. Tuning single atom-nanoparticle ratios of Ni-based catalysts for synthesis gas production from CO_2. *Appl. Catal. B Environ.* **2020**, *264*, 118502. [CrossRef]
161. Daiyan, R.; Chen, R.; Kumar, P.; Bedford, N.M.; Qu, J.; Cairney, J.M.; Lu, X.; Amal, R. Tunable Syngas Production through CO_2 Electroreduction on Cobalt-Carbon Composite Electrocatalyst. *ACS Appl. Mater. Interfaces* **2020**, *12*, 9307–9315. [CrossRef]
162. Zhang, M.; Hu, Z.; Gu, L.; Zhang, Q.; Zhang, L.; Song, Q.; Zhou, W.; Hu, S. Electrochemical conversion of CO_2 to syngas with a wide range of CO/H_2 ratio over Ni/Fe binary single-atom catalysts. *Nano Res.* **2020**, *13*, 3206–3211. [CrossRef]

163. Yang, H.; Wu, Y.; Li, G.; Lin, Q.; Hu, Q.; Zhang, Q.; Liu, J.; He, C. Scalable Production of Efficient Single-Atom Copper Decorated Carbon Membranes for CO_2 Electroreduction to Methanol. *J. Am. Chem. Soc.* **2019**, *141*, 12717–12723. [CrossRef]
164. Karapinar, D.; Huan, N.T.; Ranjbar Sahraie, N.; Li, J.; Wakerley, D.; Touati, N.; Zanna, S.; Taverna, D.; Galvão Tizei, L.H.; Zitolo, A.; et al. Electroreduction of CO_2 on Single-Site Copper-Nitrogen-Doped Carbon Material: Selective Formation of Ethanol and Reversible Restructuration of the Metal Sites. *Angew. Chem. Int. Ed.* **2019**, *58*, 15098–15103. [CrossRef]
165. Zhao, K.; Nie, X.; Wang, H.; Chen, S.; Quan, X.; Yu, H.; Choi, W.; Zhang, G.; Kim, B.; Chen, J.G. Selective electroreduction of CO_2 to acetone by single copper atoms anchored on N-doped porous carbon. *Nat. Commun.* **2020**, *11*, 1–10. [CrossRef]
166. Shang, H.; Wang, T.; Pei, J.; Jiang, Z.; Zhou, D.; Wang, Y.; Li, H.; Dong, J.; Zhuang, Z.; Chen, W.; et al. Design of a Single-Atom Indium$^{\delta+}$–N_4 Interface for Efficient Electroreduction of CO_2 to Formate. *Angew. Chem.* **2020**, *132*, 22651–22655. [CrossRef]
167. Jiang, Z.; Wang, T.; Pei, J.; Shang, H.; Zhou, D.; Li, H.; Dong, J.; Wang, Y.; Cao, R.; Zhuang, Z.; et al. Discovery of main group single Sb-N_4 active sites for CO_2 electroreduction to formate with high efficiency. *Energy Environ. Sci.* **2020**, *13*, 2856–2863. [CrossRef]
168. Yang, X.; Chen, Y.; Qin, L.; Wu, X.; Wu, Y.; Yan, T.; Geng, Z.; Zeng, J. Boost Selectivity of HCOO− Using Anchored Bi Single Atoms towards CO_2 Reduction. *ChemSusChem* **2020**, *13*, 6307–6311. [CrossRef]
169. Han, L.; Song, S.; Liu, M.; Yao, S.; Liang, Z.; Cheng, H.; Ren, Z.; Liu, W.; Lin, R.; Qi, G.; et al. Stable and Efficient Single-Atom Zn Catalyst for CO_2 Reduction to CH4. *J. Am. Chem. Soc.* **2020**, *142*, 12563–12567. [CrossRef]
170. Lu, X.L.; Rong, X.; Zhang, C.; Lu, T.B. Carbon-based single-atom catalysts for CO_2 electroreduction: Progress and optimization strategies. *J. Mater. Chem. A* **2020**, *8*, 10695–10708. [CrossRef]
171. Beniya, A.; Higashi, S. Towards dense single-atom catalysts for future automotive applications. *Nat. Catal.* **2019**, *2*, 590–602. [CrossRef]
172. Soloducho, J.; Cabaj, J.; Zajac, D. *Advances in Electrode Materials*; Scrivener Publishing LLC: Beverly, MA, USA, 2016; pp. 1–26. [CrossRef]
173. Nursanto, E.B.; Jeon, H.S.; Kim, C.; Jee, M.S.; Koh, J.H.; Hwang, Y.J.; Min, B.K. Gold catalyst reactivity for CO_2 electro-reduction: From nano particle to layer. *Catal. Today* **2016**, *260*, 107–111. [CrossRef]
174. Kemp, R.; Dickie, D.; Donovan, E.S.; Barry, B. Carbon dioxde transformation facilitated by earth abundant metals. U.S. Patent 10,131,996, 20 November 2018. Available online: https://patents.google.com/patent/US20170016126A1/en (accessed on 19 October 2020).
175. Yang, Z.; Oropeza, F.E.; Zhang, K.H.L. P-block metal-based (Sn, In, Bi, Pb) electrocatalysts for selective reduction of CO_2 to formate. *APL Mater.* **2020**, *8*, 60901. [CrossRef]
176. Zhang, D.; Tao, Z.; Feng, F.; He, B.; Zhou, W.; Sun, J.; Xu, J.; Wang, Q.; Zhao, L. High efficiency and selectivity from synergy: Bi nanoparticles embedded in nitrogen doped porous carbon for electrochemical reduction of CO_2 to formate. *Electrochim. Acta* **2020**, *334*. [CrossRef]
177. Centi, G.; Perathoner, S.; Winè, G.; Gangeri, M. Electrocatalytic conversion of CO_2 to long carbon-chain hydrocarbons. *Green Chem.* **2007**, *9*, 671–678. [CrossRef]
178. Pérez-Rodríguez, S.; Pastor, E.; Lázaro, M.J. Noble metal-free catalysts supported on carbon for CO_2 electrochemical reduction. *J. CO_2 Util.* **2017**, *18*, 41–52. [CrossRef]
179. Sheng, W.; Kattel, S.; Yao, S.; Yan, B.; Liang, Z.; Hawxhurst, C.J.; Wu, Q.; Chen, J.G. Electrochemical reduction of CO_2 to synthesis gas with controlled CO/H_2 ratios. *Energy Environ. Sci.* **2017**, *10*, 1180–1185. [CrossRef]
180. Xie, H.; Chen, S.; Ma, F.; Liang, J.; Miao, Z.; Wang, T.; Wang, H.L.; Huang, Y.; Li, Q. Boosting Tunable Syngas Formation via Electrochemical CO_2 Reduction on Cu/In_2O_3 Core/Shell Nanoparticles. *ACS Appl. Mater. Interfaces* **2018**, *10*, 36996–37004. [CrossRef]
181. Silva, W.O.; Silva, G.C.; Webster, R.F.; Benedetti, T.M.; Tilley, R.D.; Ticianelli, E.A. Electrochemical Reduction of CO_2 on Nitrogen-Doped Carbon Catalysts With and Without Iron. *ChemElectroChem* **2019**, *6*, 4626–4636. [CrossRef]
182. Franco, F.; Rettenmaier, C.; Jeon, H.S.; Roldan Cuenya, B. Transition metal-based catalysts for the electrochemical CO_2 reduction: From atoms and molecules to nanostructured materials. *Chem. Soc. Rev.* **2020**, *49*, 6884–6946. [CrossRef]
183. Kim, C.; Jeon, H.S.; Eom, T.; Jee, M.S.; Kim, H.; Friend, C.M.; Min, B.K.; Hwang, Y.J. Achieving Selective and Efficient Electrocatalytic Activity for CO_2 Reduction Using Immobilized Silver Nanoparticles. *J. Am. Chem. Soc.* **2015**, *137*, 13844–13850. [CrossRef]
184. Jia, M.; Choi, C.; Wu, T.S.; Ma, C.; Kang, P.; Tao, H.; Fan, Q.; Hong, S.; Liu, S.; Soo, Y.L.; et al. Carbon-supported Ni nanoparticles for efficient CO_2 electroreduction. *Chem. Sci.* **2018**, *9*, 8775–8780. [CrossRef]
185. Zhang, L.; Mao, F.; Zheng, L.R.; Wang, H.F.; Yang, X.H.; Yang, H.G. Tuning Metal Catalyst with Metal-C_3N_4 Interaction for Efficient CO_2 Electroreduction. *ACS Catal.* **2018**, *8*, 11035–11041. [CrossRef]
186. Zhao, S.; Tang, Z.; Guo, S.; Han, M.; Zhu, C.; Zhou, Y.; Bai, L.; Gao, J.; Huang, H.; Li, Y.; et al. Enhanced Activity for CO_2 Electroreduction on a Highly Active and Stable Ternary Au-CDots-C_3N_4 Electrocatalyst. *ACS Catal.* **2018**, *8*, 188–197. [CrossRef]
187. Zhang, S.; Kang, P.; Meyer, T.J. Nanostructured Tin Catalysts for Selective Electrochemical Reduction of Carbon Dioxide to Formate. *J. Am. Chem. Soc.* **2014**, *136*, 1734–1737. [CrossRef]
188. Song, Y.; Peng, R.; Hensley, D.K.; Bonnesen, P.V.; Liang, L.; Wu, Z.; Meyer, H.M.; Chi, M.; Ma, C.; Sumpter, B.G.; et al. High-Selectivity Electrochemical Conversion of CO_2 to Ethanol using a Copper Nanoparticle/N-Doped Graphene Electrode. *ChemistrySelect* **2016**, *1*, 6055–6061. [CrossRef]

189. Legrand, U.; Boudreault, R.; Meunier, J.L. Decoration of N-functionalized graphene nanoflakes with copper-based nanoparticles for high selectivity CO_2 electroreduction towards formate. *Electrochim. Acta* **2019**, *318*, 142–150. [CrossRef]
190. Rogers, C.; Perkins, W.S.; Veber, G.; Williams, T.E.; Cloke, R.R.; Fischer, F.R. Synergistic Enhancement of Electrocatalytic CO_2 Reduction with Gold Nanoparticles Embedded in Functional Graphene Nanoribbon Composite Electrodes. *J. Am. Chem. Soc.* **2017**, *139*, 4052–4061. [CrossRef] [PubMed]
191. Yuan, J.; Yang, M.P.; Zhi, W.Y.; Wang, H.; Wang, H.; Lu, J.X. Efficient electrochemical reduction of CO_2 to ethanol on Cu nanoparticles decorated on N-doped graphene oxide catalysts. *J. CO_2 Util.* **2019**, *33*, 452–460. [CrossRef]
192. Ning, H.; Mao, Q.; Wang, W.; Yang, Z.; Wang, X.; Zhao, Q.; Song, Y.; Wu, M. N-doped reduced on graphene oxide supported Cu2O nanocubes as high active catalyst for CO_2 electroreduction to C_2H_4. *J. Alloys Compd.* **2019**, *785*, 7–12. [CrossRef]
193. Zeng, L.; Shi, J.; Luo, J.; Chen, H. Silver sulfide anchored on reduced graphene oxide as a high -performance catalyst for CO_2 electroreduction. *J. Power Sources* **2018**, *398*, 83–90. [CrossRef]
194. Sun, J.; Zheng, W.; Lyu, S.; He, F.; Yang, B.; Li, Z.; Lei, L.; Hou, Y. Bi/Bi_2O_3 nanoparticles supported on N-doped reduced graphene oxide for highly efficient CO_2 electroreduction to formate. *Chin. Chem. Lett.* **2020**, *31*, 1415–1421. [CrossRef]
195. Hossain, M.N.; Wen, J.; Chen, A. Unique copper and reduced graphene oxide nanocomposite toward the efficient electrochemical reduction of carbon dioxide. *Sci. Rep.* **2017**, *7*, 3184. [CrossRef]
196. Genovese, C.; Ampelli, C.; Perathoner, S.; Centi, G. Electrocatalytic conversion of CO_2 on carbon nanotube-based electrodes for producing solar fuels. *J. Catal.* **2013**, *308*, 237–249. [CrossRef]
197. Xu, C.; Vasileff, A.; Jin, B.; Wang, D.; Xu, H.; Zheng, Y.; Qiao, S.Z. Graphene-encapsulated nickel-copper bimetallic nanoparticle catalysts for electrochemical reduction of CO_2 to CO. *Chem. Commun.* **2020**, *56*, 11275–11278. [CrossRef]
198. Wei, B.; Xiong, Y.; Zhang, Z.; Hao, J.; Li, L.; Shi, W. Efficient electrocatalytic reduction of CO^2 to HCOOH by bimetallic In-Cu nanoparticles with controlled growth facet. *Appl. Catal. B Environ.* **2021**, *283*, 119646. [CrossRef]
199. Safdar Hossain, S.; Rahman, S.U.; Ahmed, S. Electrochemical reduction of carbon dioxide over CNT-supported nanoscale copper electrocatalysts. *J. Nanomater.* **2014**, *2014*, 374318. [CrossRef]
200. Zhang, R.; Lv, W.; Li, G.; Lei, L. Electrochemical reduction of CO_2 on SnO_2/nitrogen-doped multiwalled carbon nanotubes composites in $KHCO_3$ aqueous solution. *Mater. Lett.* **2015**, *141*, 63–66. [CrossRef]
201. Zheng, W.; Guo, C.; Yang, J.; He, F.; Yang, B.; Li, Z.; Lei, L.; Xiao, J.; Wu, G.; Hou, Y. Highly active metallic nickel sites confined in N-doped carbon nanotubes toward significantly enhanced activity of CO_2 electroreduction. *Carbon* **2019**, *150*, 52–59. [CrossRef]
202. Wang, T.; Yang, J.; Chen, J.; He, Q.; Li, Z.; Lei, L.; Lu, J.; Leung, M.K.H.; Yang, B.; Hou, Y. Nitrogen-doped carbon nanotube-encapsulated nickel nanoparticles assembled on graphene for efficient CO_2 electroreduction. *Chin. Chem. Lett.* **2020**, *31*, 1438–1442. [CrossRef]
203. Lee, M.Y.; Ringe, S.; Kim, H.; Kang, S.; Kwon, Y. Electric field mediated selectivity switching of electrochemical CO_2 reduction from formate to CO on carbon supported Sn. *ACS Energy Lett.* **2020**, *5*, 2987–2994. [CrossRef]
204. Maldonado-Hódar, F.J.; Moreno-Castilla, C.; Pérez-Cadenas, A.F. Surface morphology, metal dispersion, and pore texture of transition metal-doped monolithic carbon aerogels and steam-activated derivatives. *Microporous Mesoporous Mater.* **2004**, *69*, 119–125. [CrossRef]
205. Moreno-Castilla, C.; Maldonado-Hódar, F.J.; Pérez-Cadenas, A.F. Physicochemical Surface Properties of Fe, Co, Ni, and Cu-Doped Monolithic Organic Aerogels. *Langmuir* **2003**, *19*, 5650–5655. [CrossRef]
206. Maldonado-Hódar, F.J.; Moreno-Castilla, C.; Rivera-Utrilla, J.; Hanzawa, Y.; Yamada, Y. Catalytic Graphitization of Carbon Aerogels by Transition Metals. *Langmuir* **2000**, *16*, 4367–4373. [CrossRef]
207. Gallegos-Suárez, E.; Pérez-Cadenas, A.F.; Maldonado-Hódar, F.J.; Carrasco-Marín, F. On the micro- and mesoporosity of carbon aerogels and xerogels. The role of the drying conditions during the synthesis processes. *Chem. Eng. J.* **2012**, *181–182*, 851–855. [CrossRef]
208. Pérez-Cadenas, A.F.; Moreno-Castilla, C.; Carrasco-Marin, F.; Maldonado-Hódar, F.; Morales-Torres, S.; Kapteijn, F. Dodep Carbon Material for the Electrocatalytic Conversion of CO_2 into Hydrocarbons, Uses pf the Material and Conversion Method Using Said. Material. Patent No. WO2013004882, 10 January 2013.
209. Pérez-Cadenas, A.F.; Ros, C.H.; Morales-Torres, S.; Pérez-Cadenas, M.; Kooyman, P.J.; Moreno-Castilla, C.; Kapteijn, F. Metal-doped carbon xerogels for the electro-catalytic conversion of CO_2 to hydrocarbons. *Carbon* **2013**, *56*, 324–331. [CrossRef]
210. Abdelwahab, A.; Castelo-Quibén, J.; Pérez-Cadenas, M.; Elmouwahidi, A.; Maldonado-Hódar, F.J.; Carrasco-Marín, F.; Pérez-Cadenas, A.F. Cobalt-doped carbon gels as electro-catalysts for the reduction of CO_2 to hydrocarbons. *Catalysts* **2017**, *7*, 25. [CrossRef]
211. Castelo-Quibén, J.; Abdelwahab, A.; Pérez-Cadenas, M.; Morales-Torres, S.; Maldonado-Hódar, F.J.; Carrasco-Marín, F.; Pérez-Cadenas, A.F. Carbon-iron electro-catalysts for CO_2 reduction. The role of the iron particle size. *J. CO_2 Util.* **2018**, *24*, 240–249. [CrossRef]
212. Castelo-Quibén, J.; Elmouwahidi, A.; Maldonado-Hódar, F.J.; Carrasco-Marín, F.; Pérez-Cadenas, A.F. Metal-carbon-CNF composites obtained by catalytic pyrolysis of urban plastic residues as electro-catalysts for the reduction of CO_2. *Catalysts* **2018**, *8*, 198. [CrossRef]
213. Castelo-Quibén, J.; Bailón-García, E.; Pérez-Fernández, F.J.; Carrasco-Marín, F.; Pérez-Cadenas, A.F. Mesoporous carbon nanospheres with improved conductivity for electro-catalytic reduction of O_2 and CO_2. *Carbon* **2019**, *155*, 88–99. [CrossRef]

214. Ripatti, D.S.; Veltman, T.R.; Kanan, M.W. Carbon Monoxide Gas Diffusion Electrolysis that Produces Concentrated C2 Products with High Single-Pass Conversion. *Joule* **2019**, *3*, 240–256. [CrossRef]
215. Messias, S.; da Ponte, M.; Reis-Machado, S.A. Carbon Materials as Cathode Constituents for Electrochemical CO_2 Reduction—A Review. *J. Carbon Res.* **2019**, *5*, 83. [CrossRef]
216. Ma, S.; Luo, R.; Gold, J.I.; Yu, A.Z.; Kim, B.; Kenis, P.J.A. Carbon nanotube containing Ag catalyst layers for efficient and selective reduction of carbon dioxide. *J. Mater. Chem. A* **2016**, *4*, 8573–8578. [CrossRef]
217. Daiyan, R.; Lu, X.; Tan, X.; Zhu, X.; Chen, R.; Smith, S.C.; Amal, R. Antipoisoning nickel-carbon electrocatalyst for practical electrochemical CO_2 reduction to CO. *ACS Appl. Energy Mater.* **2019**, *2*, 8002–8009. [CrossRef]